

**Characterization of High Entropy Alloys for Magnetocaloric
Applications**

Submitted in partial fulfillment of the requirements for
the degree of
Doctor of Philosophy
in
Materials Science and Engineering

Alice E. Perrin

B.S., Physics, The College of William and Mary
M.S., Materials Science and Engineering, Carnegie Mellon University

Carnegie Mellon University
Pittsburgh, PA

December 2019

Contents

Contents	ii
Abstract	vi
Acknowledgments	viii
List of Figures	x
List of Tables	xv
1 Introduction	1
1.1 Structures of Metals	3
1.1.1 Crystal Structures	3
1.1.2 Phases and Phase Diagrams	4
1.1.3 Electronic Configurations of Transition Metals	8
1.2 Soft Magnetic Materials	9
1.2.1 Ferromagnetism	9
1.2.2 Exchange Interactions	13
1.3 Magnetic Refrigeration	16
1.3.1 The Magnetocaloric Effect	16
1.3.2 Applications of Magnetocaloric Cooling	24
1.3.3 Current Magnetocaloric Materials of Interest	30

1.4	High Entropy Alloys	33
1.4.1	Structure and Physics	33
1.4.2	Previous Study and Applications	36
1.5	Hypothesis	37
2	Experimental Techniques and Sample Preparation	40
2.1	Sample Production	40
2.1.1	Arc Melting and Melt Spinning	40
2.1.2	Thin Film Sputtering	41
2.1.3	Compositional Analysis	43
2.2	Structural Characterization	43
2.2.1	X-Ray Diffraction	43
2.2.2	Scanning Electron Microscopy and Electron Dispersive Spectroscopy .	46
2.2.3	Differential Scanning Calorimetry	47
2.3	Magnetic Characterization	47
2.3.1	Vibrating Sample Magnetometry	47
2.3.2	Mössbauer Spectroscopy	50
2.3.3	Magneto-Optical Kerr Effect	53
2.4	Applied Pressure Experiments	54
2.4.1	High Pressure XRD	54
2.4.2	High Pressure Magnetometry	55
3	Developing Magnetocaloric HEAs in the FeCoNiCuX System	57
3.1	Basis of Alloy Development and Curie Temperature Engineering	57
3.2	Structural Characterization	61
3.3	Magnetic Characterization	63
3.4	Summary	65

4	Analysis of Compositional Variation In FeCoNiCuMn System	67
4.1	Pseudo-Binary Compositional Variations in System	67
4.2	Magnetic Analysis through Mössbauer Spectroscopy	72
4.2.1	Qualitative Observation of Exchange Interactions	72
4.2.2	Quantitative Analysis of Hyperfine Field Distributions	73
4.3	Summary	79
5	The Effects of Pressure on the FeCoNiCuMn System	80
5.1	High Pressure X-Ray Diffraction	80
5.2	High Pressure Magnetization Measurements	83
5.3	Analysis of Pressure Effects on D-Orbital Spatial Extent	86
5.4	Summary	91
6	Analysis of Low Temperature Magnetic Transition in FeCoNiCuMn System	94
6.1	Magnetic Domain Formation	95
6.2	Antiferromagnetic Exchange	97
6.3	Summary	99
7	Conclusions and Future Work	100
	Bibliography	104
	Appendix A Sample Synthesis	118
A.1	ICP-AES Data	118
A.2	Thin Film Development	119
A.2.1	Compositional Analysis	119
A.2.2	Crystallographic Characterization	121
A.2.3	Magnetic Characterization	122
A.2.4	Conclusion	123

<i>CONTENTS</i>	v
Appendix B Relevant Phase Diagrams	126
Appendix C Mossbauer Raw Data	130
C.1 Raw Data Files	130

Abstract

Magnetocaloric refrigeration offers more energy efficiency than conventional gas compression refrigeration by up to 20%, and has the additional advantage of being environmentally friendly as it does not require the use of ozone depleting gases. The primary challenge in developing magnetocaloric refrigerators for commercial use is in developing suitable materials with large room temperature magnetocaloric effects. Critical rare earths metals (REs) and compounds have been studied because of their large magnetocaloric response and working temperatures close to room temperature. However, the scarcity, high price and corrosion of REs limit their commercial use, leading to the investigation of more sustainable transition metal-based alloys. I explore the possibility of developing high performance high entropy alloys for magnetocaloric applications, and my approach to this problem follows on the materials paradigm: 1) synthesis, 2) structure, 3) properties, and 4) performance. Synthesis requires determining the best conditions for producing the alloys in the proper form, and this is important both for the initial production of my bulk alloys through rapid solidification. The structure of high entropy alloys is necessarily a random distribution of atoms, and an investigation of the homogeneity of this condition through electron dispersive spectroscopy is vital for determining the stability of the alloy. I investigate the magnetic and thermal properties of these alloys both to assess their fitness for specific magnetocaloric applications, and also to better understand the relationship between their structure and properties. Mössbauer spectroscopy experiments for magnetic data was performed in collaboration with Monica Sorescu at Duquesne University. I extend this exploration through high pressure

and low temperature studies to to develop a fundamental understanding of the magnetic interactions in these alloys, including a novel approach to visualizing exchange using the Bethe-Slater curve that explore the importance of considerations of the d-orbital extent on changes in exchange. High pressure magnetic measurements were performed in collaboration with Scott McCall at Lawrence Livermore National Lab. I began this study with a focus on performance in commercial refrigeration applications, but the complex magnetic and structural attributes of these materials require rigorous study for a better understanding of magnetic high entropy alloys, and this work contributes to this relatively unexplored but growing field.

Acknowledgments

This work was funded under the National Science Foundation (NSF) Grant DMR-1709247. I acknowledge use of the Materials Characterization Facility at Carnegie Mellon University supported by grant MCF-677785, as well as use of the Data Storage Systems Center at CMU.

Academically, I have a lot of people to acknowledge for helping me throughout the last four years. My utmost gratitude to my advisors, Mike McHenry and David Laughlin. You've been patient when I needed it, but never stopped pushing scientific vigor and curiosity. You've given me so much exposure to interesting science, experimental techniques, and career and collaboration opportunities. I'm so thankful for everything I've learned from you both, and I couldn't have imagined a better graduate school experience. Thank you as well to my committee members: Dr. Monica Sorescu, Prof. Bryan Webler, and Prof. Vincent Sokalski. Your input throughout the course of my project has significantly shaped the trajectory of this work, and you've challenged me to develop a deeper understanding of my project.

Thank you to Dr. Betsy Clark, Tom Nuefer, Bill Pingatore, and Dr. Adam Wise for teaching me almost everything I know about materials characterization. A huge thank you to all of my group mates who helped me in and out of the lab: Dr. Natan Aronhime, Mari-Therese Burton, Sam Greene, Yuval Krimer, Dr. Satoru Simizu, Dr. Mst Nazumunnahar, Vishal Ravi, Bing Zhou, Tong Mo, Caroline Gorham, Yang Liu, and Vara Bollapragada. Special thanks as well to the collaborators who have helped us do so much that isn't possible in my own lab, and given me plenty of academic and career advice along with it: Dr. Mike

McElfresh, Dr. Scott McCall, Dr. Paul Ohodnicki, Dr. Monica Sorescu, Dr. Alex Leary, Vladimir Keylin, Dr. Huseyin Ucar, and Dr. Matt Lucas. My gratitude as well to a few of the CMU MSE staff who have handled so much of the organizational work that has made focusing on research easier during my time here: Marygrace Antkowski, Kelly Rockenstein, Suzy Smith, Dave Crockett, Neetha Khan, and Jeanna Pekarcik.

I'm an incredibly lucky person to have so many wonderful, supportive friends from all stages of my life: Sarah Iler, Courtney Tamaro, AK Ghimire, Amy Ryan, Anneliese Schmidt, Ali McDonnell, Phoebe Yeoh, Yuanzhi Ma, Xiaomin Tang, Dr. Rafael Giaomin, Dr. Ajay Pisat, Priya Anand, Dr. Derek Lau, Anna Weiss, Kuai-Kuai Jin, Dr. Brandon Amos, Tim Mueller-Sim, Natalie Hartog, the entire Murphy family, Terri Steffan, Jess Canose, Lindsey Laverty, and Cole MacDonald. A few people in particular have given me near constant encouragement and guidance from the beginning: Corinn Durham, Mallory Tucker, Sarah Murphy, Caroline Hamby, Megan Gulliford, and Heather Hoskins. My family, particularly my parents, James and Sophie, my brother Fain and niece Sophie, and extended family, have been a constant source of support throughout the years. This would also be incomplete if I didn't thank a few special animals, too: Fran, who got me through my overview, and all my fosters who gave me the best stress relief possible this year. This thesis is dedicated to my best friends, and two of my greatest loves: my sister, Josie, and my dog, Toby.

List of Figures

1.1	(a) A rendering of a body-centered cubic (BCC) crystal structure. (b) A rendering of a face-centered cubic (FCC) crystal structure.	4
1.2	Left: Gibbs energy of different phases in a hypothetical system at pressure P. Bold portions of lines indicate that it is the energetically favorable phase. Right: Pressure vs Temperature phase diagram for hypothetical phase; orange dotted line corresponds to pressure P of Gibbs energy plot.	5
1.3	Top: Gibbs energy of different phases in a hypothetical binary composition system at temperature T. Dotted lines indicate lowest energy for two phases, a and b. Bottom: Composition vs temperature phase diagram showing two phase region; orange dotted line corresponds to temperature T of Gibbs energy plot.	6
1.4	Left: Gibbs free energy vs. order parameter of a first order transition. Right: Gibbs free energy vs. order parameter of a higher order transition.	8
1.5	The five types of d-orbital shapes. The direction of the lobes will depend on the crystal structure and electronic environment of the atoms.	9
1.6	Orientation of magnetic moments: (A) paramagnetic, (B) ferromagnetic, and (C) antiferromagnetic.	11
1.7	Magnetization vs. temperature behavior for higher order vs. first order magneto-structural phase transitions.	12

1.8	The Slater-Pauling curve, showing the relationship between number of electrons and magnetization. Reprinted with permission from J.C. Slater, Physical Review 49, pg. 931, 1936. Copyright 2019 by the American Physical Society. [1]	13
1.9	A B-H loop for a ferromagnetic material. [2]	14
1.10	The Bethe-Slater curve, demonstrating the relationship between atomic spacing normalized by d-orbital extent and exchange energy.	17
1.11	The magnetocaloric effect in a full refrigeration cycle, compared with a conventional vapor refrigeration cycle.	18
1.12	Isothermal magnetization versus field measurements spanning the working temperature range (230K to 370K in this plot) of a magnetocaloric material, which can be used to calculate the total change in magnetic entropy.	20
1.13	Calculated change in magnetic entropy vs. temperature from the measured isotherms, which is equal to the change in thermal entropy.	20
1.14	Various methods of calculating refrigeration capacity for a given ΔS curve. [3]	22
1.15	Different thermodynamic cycles possible for magnetocaloric refrigeration systems. [4]	25
1.16	A Halbach cylinder with labelled design parameters.	27
1.17	Self pumping magnetic cooling system [5]	29
1.18	2012 compilation of classes of MCE materials considering T_c and ΔT achieved for each. [6]	32
1.19	Rendering of a 5-component high entropy alloy. [7]	35
2.1	Diagram of the arc melting chamber. Alloys are heated and mixed with the plasma arc several times to ensure homogeneity. Adapted from [8]	41
2.2	Diagram of the melt spinning process. Alloys are rapidly quenched in the ejection stage. [9]	42
2.3	Diagram of the experimental setup of x-ray diffraction, demonstrating the frame of reference for the angle of diffraction. [10].	45
2.4	Arrott Noakes plot for an $Fe_{75}Pt_{25}$ alloy with T_c between 403K and 413K. [11]	49

2.5	A magnetization versus temperature curve with the derivative curve, dM/dT overlaid to show the calculated inflection point. The slope at the inflection point is extended down until it intersects with the x axis in order to calculate T_c	50
2.6	Experimental setup of Mössbauer spectroscopy measurements. If the emitter and absorber nuclei are identical, the transmission spectrum will be a simple peak, as it appears above. [12]	51
2.7	Electronic energy levels experiencing Zeeman splitting due to magnetic dipoles (right). [13]	53
2.8	Example Mössbauer spectra for gamma rays after passing through $Fe_{80}B_{20}$. All six peaks due to Zeeman splitting are clearly defined. [14]	54
2.9	Diamond anvil cell designed to apply uniform pressure to samples	55
2.10	Beamline setup in which white radiation passes through the pressure cell into a solid state detector.	55
2.11	Mcell 10 pressure cell, which houses the sample in the TPFPE plug and is mounted in a SQUID system. [15]	56
3.1	X-ray diffraction scans for each five-component HEA. FCC peaks are labelled at the top in black, and some extraneous BCC peaks labelled in red can be seen in the red spectrum of $FeCoNiCuAg$	62
3.2	EDS composition maps of (a) $FeCoNiCuMn$, (b) $FeCoNiCuAg$, (c) $FeCoNiCuPt$, and (d) $FeCoNiCuMo$. Clustering is evident in (b) and (d).	63
3.3	Magnetization versus temperature for (a) $FeCoNiCuMn$, (b) $FeCoNiCuAg$, (c) $FeCoNiCuPt$, and (d) $FeCoNiCuMo$. Dotted red lines indicate the inflection point slope used to calculate T_c . Green arrows indicate cooling curve and red arrows indicate heating curves.	64
4.1	T_c values for alloys in the $FeCoNiCuMn$ pseudo-binary systems, plotted with respect to their atomic Mn content. The two most promising alloys are circled in red. . .	69

4.2	RC values for alloys in the FeCoNiCuMn psuedo-binary systems, plotted with respect to their atomic Mn content. The two most promising alloys are circled in red.	70
4.3	Top: Mössbauer spectra for two HEA alloys. Bottom: Corresponding HFDs, with discrete peaks and shoulders denoted with red arrows.	74
4.4	T_c of pseudo-binary alloys plotted against average hyperfine field, demonstrating that the relationship is composition-independent for small variational changes. . .	75
5.1	Diffraction peaks for FeCoNiCuMn with applied pressure. Shoulders present on all patterns (including atmospheric pressure) are due to copper clustering.	81
5.2	Plot of magnetization vs. temperature at several applied pressures. Each measurement follows the pattern: (1)ZFC to 5K, (2) 20Oe field heating to 350K, (3) 20Oe field cooling back to 5K.	84
5.3	The relationship between applied pressure and measured T_c values, which is fairly linear.	85
5.4	(a) Bethe Slater Curve, showing the empirical relationship between J_{ex} and D/d_{d3} . (b) T_c of the disordered FCC Fe-Ni phase. [16]	86
5.5	(a) P vs a (lattice spacing) for FeCoNuCuMn derived from high pressure XRD data. From this data I calculated the change in atomic spacing, $D = \frac{a}{\sqrt{2}}$. . .	88
5.6	(a) d orbital diameter versus applied pressure for the FeCoNiCu ₁₉ Mn ₂₁ alloy. (b) $\frac{D}{d}$ ratio with applied pressure, which increases despite both D and d decreasing with pressure.	92
5.7	Magnitude of first term and second term from parentheses in equation 5.9. . .	93
6.1	Magnetization heating curves at different applied fields, taken after zero field cooling. 95	
6.2	Magnetization vs. temperature measurements (with ZFC) demonstrating that the low temperature transition is not changed with small compositional variation. . .	96

6.3	Magnetization vs. temperature measurements for alloys with greater compositional variation showing the emergence of a low temperature dip in the magnetization.	98
A.1	X-ray diffraction of a 20nm thin film sputtered from an equiatomic FeCoNiCuMn target.	122
A.2	X-ray diffraction of a 100nm thin film sputtered from an equiatomic FeCoNiCuMn target.	123
A.3	Magnetization vs. temperature of the sputtered thin films, normalized for shape comparison.	124
A.4	Magnetization vs. field for sputtered thin films, demonstrating the in plane coercivity to be larger than out of plane for both thicknesses of film.	125
B.1	Phase diagram for Cu-Mo binary system showing immiscibility up through liquid phases. [17]	127
B.2	Phase diagram for Cu-Mn binary system [18]	127
B.3	Phase diagram for Co-Mn binary system [18]	128
B.4	Phase diagram for Ni-Mn binary system [19]	128
B.5	Phase diagram for Fe-Mn binary system [20]	129

List of Tables

3.1	T_c of several 5+ component HEAs.	58
3.2	T_c , M_s , RC, and assessment of homogeneity for HEAs.	65
4.1	Top:Configurational entropy calculated for equiatomic alloys with different number of components. Right columns show the difference between the calculation and a binary alloys (S_{2-equi}), and the % S increases. Bottom: Configurational entropy calculated for small psuedo-binary departures from equiatomic in 5-component alloys. Right columns show the net difference from equiatomic, and the % S decreases.	68
4.2	Summary of properties of several promising magnetocaloric materials; my current alloys of focus are listed first.	71
4.3	Mössbauer spectroscopy data for FeCoNiCuMn pseudo-binaries.	73
4.4	Contributions to average hyperfine field from each element.	78
5.1	Bulk modulus of FeCoNiCuMn compared with elemental components, and other common alloys.	82
A.1	Atomic percentages of each atom present in bulk FeCoNiCuMn for each psuedo-binary departure from equiatomic.	119
A.2	Atomic percentages of each species present in sputtered thin films (measured using XPS analysis) compared with experimental bulk composition.	119
A.3	Coercivity and saturation fields for thin films and bulk samples of FeCoNiCuMn.	124

Chapter 1

Introduction

High entropy alloys (HEAs) are multicomponent systems in which configurational entropy is larger than the fusion entropy of most common metals. In many HEAs, BCC or FCC phases are entropically stabilized, avoiding intermetallic formation to enhance solid solution strengthening. Recently, HEAs are studied for magnetocaloric effect (MCE) applications. This thesis presents magnetic investigations of HEAs aimed at optimizing MCE near room temperature and describing the discrete exchange interactions in the system which act to distribute contributions to the magnetic entropy.

This introductory chapter discusses relevant background to make the goals of this project more clear, starting with an overview of atomic structure, phases, and electronic structure; the physics of soft magnetic materials and magnetocaloric refrigeration by the magnetocaloric effect; and high entropy alloys and previous study of both high entropy and magnetocaloric materials. This information provides the necessary background information to understand the underlying logic of my thesis hypotheses. My thesis hypotheses are that a magnetic high entropy alloy can be developed which will have advantageous magnetocaloric properties, and these properties, which include a broader magnetic entropy curve, will be caused by the distribution of exchange caused by the mixing of several magnetic atoms in a single phase. This distribution of exchange is caused by the sum of several discrete exchange

interactions which suggest localized electronic behavior in these alloys.

Chapter 2 will discuss the experimental methods required for sample synthesis and preparation, magnetic characterization to assess the samples' fitness in magnetocaloric refrigerators, structural characterization to assess the stability of the high entropy alloys' single phase, and high pressure experiments to further probe the distribution of exchange interactions.

Chapter 3 will give an overview of the range of high entropy alloys I developed at the outset of this project, four of which I chose to characterize further and compare against one another. From this study, FeCoNiCuMn was chosen as the most promising HEA for magnetocaloric applications.

Chapter 4 will discuss Mössbauer spectroscopy performed on these alloys and the calculations resulting from these measurements which allowed us to quantify the individual contributions to T_c of the alloys in the FeCoNiCuMn HEA system.

Chapter 5 discusses several applied pressure experiments and calculations I have performed on the FeCoNiCuMn HEA system to further probe the exchange interactions in the system. I combine experimental work with observations on the nature of the Bethe-Slater curve to calculate the change in the expectation value of the d-orbital radius in these alloys.

Chapter 6 focuses on the low temperature behavior observed in zero field cooling measurements on the FeCoNiCuMn HEA system and the possible explanations for this behavior.

Chapter 7 summarizes the overarching conclusions I can draw from the last four years of research on this project, and describes future work which will be done on this project to bolster the conclusions of chapters 4 through 6.

1.1 Structures of Metals

1.1.1 Crystal Structures

Pure metals are almost always crystalline in structure, meaning that their atoms align in a regular lattice formation periodically in 3D. There are 14 unique regular lattices, known as Bravais lattices, but the majority of metals fall into cubic lattice structures [21]. All alloys characterized in this thesis fall into two lattice types: body centered cubic (BCC), in which atoms sit on the corners of a cubic cell in addition to an atom sitting in the center of the cube (Fig. 1.1a); and face centered cubic (FCC), in which atoms sit on the corner of a cubic cell, and also on each face of the cube (Fig. 1.1b). Face centered cubic structures are close packed, which means that the atoms are arranged in such a way to minimize the amount of unused space between atoms. The configuration of atoms in a given metal will depend on what is most energetically favorable for that element or alloy, and this will rely on a multitude of factors including magnetic behavior and electron density. An element or alloy can change crystal structure at specific temperatures if these factors change with temperature—for example, magnetic transitions often occur with structural transitions. In crystalline structures, directions within the material can be significant. X-ray diffraction (sec 2.2.1) can be used to calculate the type and spacing of the lattice through diffracted peaks that are indicative of the different planes of atoms in a sample. The close packing of FCC prohibits more diffraction peaks than BCC due to the additional atoms on the faces, so the first plane that can diffract x-rays in an FCC lattice is the (111) plane, which extends across the body diagonal of the crystal. The different planes and directions in the crystal can also be significant in magnetic materials to determine the direction of magnetization, but this is not significant in my magnetic alloys.

There are also metallic alloys which can be amorphous, meaning that there is no regular crystal structure, and the structure is a jumble of atoms resembling a liquid [16]. This requires a specific alloying procedure (usually rapid solidification from the liquid phase) and

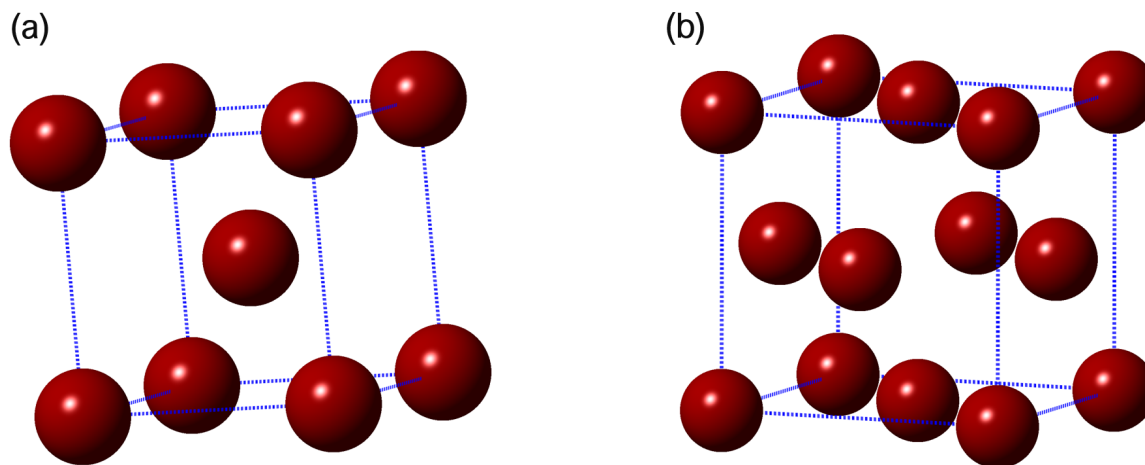


Figure 1.1: (a) A rendering of a body-centered cubic (BCC) crystal structure. (b) A rendering of a face-centered cubic (FCC) crystal structure.

typically requires an additional element present which prevents the formation of a crystal structure, such as much larger atoms whose size prohibit a lattice from forming without excessive strain. Certain forms of materials, such as a metal sputtered into a thin film, are more likely to be amorphous [22]. Because of their electronic structure, metal atoms are energetically likely to crystallize, so amorphous phases of metals are always considered “metastable”.

1.1.2 Phases and Phase Diagrams

A material at any given temperature and pressure is defined in part by the phase it’s in, which refers to the crystallographic structure as well as the magnetic, electric, or elastic properties of the material. The structure and properties will all have a critical temperature at which they arise or disappear depending on the which of the different potential phases of a system have the lowest Gibbs free energy (Fig. 1.2)

Phases of a material can be considered stable, metastable, or unstable depending on the Gibbs free energy of the phase, and whether they formed in a slow equilibrium environment, or from a rapid non-equilibrium process. As mentioned in section 1.1.1, amorphous metallic

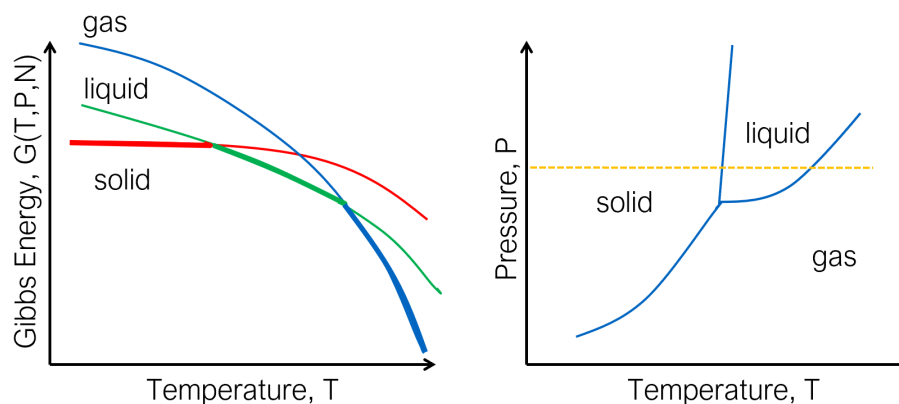


Figure 1.2: Left: Gibbs energy of different phases in a hypothetical system at pressure P . Bold portions of lines indicate that it is the energetically favorable phase. Right: Pressure vs Temperature phase diagram for hypothetical phase; orange dotted line corresponds to pressure P of Gibbs energy plot.

phases are often formed in a rapid solidification process, which allows the formation of a phase that is likely not the stable equilibrium phase of the metallic alloys in question. However, because the alloys are being rapidly cooled from a liquid, a metastable amorphous phase can form because the liquid phase (with necessarily amorphous structure) was stable at the high temperature. A metastable phase can be relatively stable (meaning the phase will remain for a long period of time, i.e. hundreds of years) depending on the elements present and how they interact, as well as how the material is used (if a metastable phase is heated repeatedly, for example, it likely will not remain in that phase as heat allows equilibrium phases to begin to form).

To determine which equilibrium phases will form, we can consult phase diagrams for a given alloy. Phase diagrams are a useful resource for determining which phases should form in an alloy at a certain temperature, pressure, and composition. Composition-varied phase diagrams will show us whether specific mixtures of alloys will remain single phase or decompose, which results in the formation of two phases of an alloy with different compositions. Decomposition occurs at the point when atoms are no longer soluble in another atomic environment, and this insolubility will increase with decreasing temperature, forming

a miscibility gap which appears as a parabola on phase diagrams in which two phases are always present (Fig. 1.3). Certain ratios of atomic species will also result in specific phase formation, which can lead to intermetallic alloy formation in complex systems. Intermetallics are the phases which disrupt a desired single phase formation, and typically have a specific stoichiometric atomic structure which is energetically favorable [23], and intermetallic formation can be desirable or undesirable depending on the type of alloy being developed. This leads to another distinction: phases can be disordered or ordered. In an ordered phase, atoms will occupy a specific site on a lattice. For example, in ordered NiAl, the Al atoms sit on the corners of the cube and the Ni atom sits in the body centered atom (Fig. 1.1a). However, high entropy alloys experience a disordered phase, in which the atoms in the alloy could occupy any site in the lattice.

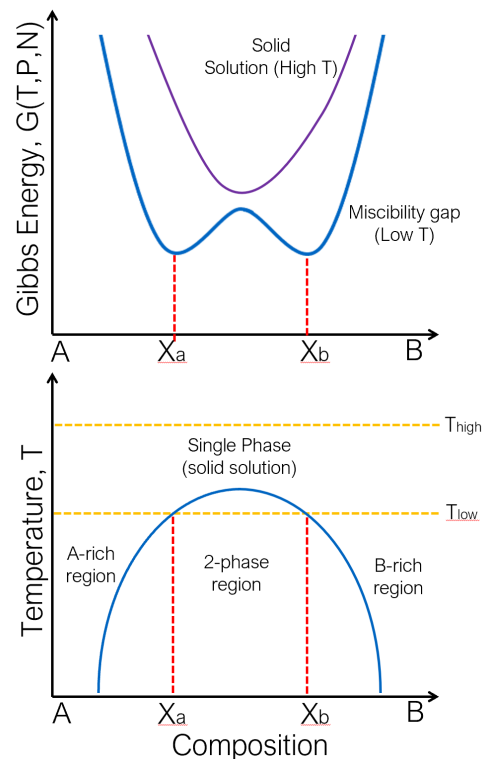


Figure 1.3: Top: Gibbs energy of different phases in a hypothetical binary composition system at temperature T . Dotted lines indicate lowest energy for two phases, a and b. Bottom: Composition vs temperature phase diagram showing two phase region; orange dotted line corresponds to temperature T of Gibbs energy plot.

Phases are also defined by the type of transitions that occur as they arise or disappear. Phase transformations are defined as being first order if they arise from a disruptive change in the material, such as a crystal structure change, and there are often discontinuities in other properties of the material during these phase (such as heat capacity). Higher order phase transitions do not cause a discontinuity in other properties, and these transitions will correspond to an order parameter which decreases continuously from 0 Kelvin to the transition temperature. The order parameter is a measure of the ordering of the new symmetry which arises in a phase transition and the exact order parameter is dependent on the type of transition. The order parameter of a magnetic transition is defined as the magnetization normalized by the saturation magnetization at 0K, which is the maximum possible magnetization of the material in that phase. Magnetic transitions can be first order if they are accompanied by a structural transition, but a magnetic transition on its own is a higher order transition. Fig. 1.7 shows an example of the magnetization versus temperature curves for each type. The type of phase can be understood quantitatively by the Landau theory of phase transitions. Landau expands the Gibbs free energy, $G(T)$, as a power series with an order parameter, m :

$$G(T) = G_o(T) + \alpha(T - T_c)m^2 + \frac{1}{2}\beta m^4 + \frac{1}{3}\gamma m^6 \quad (1.1)$$

For higher order transitions, the first three terms of this equation dominate, and α and β are both positive. Higher order transitions begin at $m=0$ at $T=T_c$ and m increases continuously as T is decreased. A plot of the Gibbs free energy, $G(m)$ would have a single minimum at $m=0$ above T_c , and would form two minima at non-zero, symmetric values of m as T decreases below T_c (Fig. 1.4b). Because first order transitions experience hysteresis due to the destructive phase transformation, the Landau expansion includes the γ term to fully capture the behavior. α and γ will be positive, while β will be negative. For first order transitions, there will be three minima in the Gibbs energy at the transition temperature;

one at $m=0$, and two at non-zero, symmetric values, pointing to the co-existence of two phases during the transition (Fig. 1.4a).

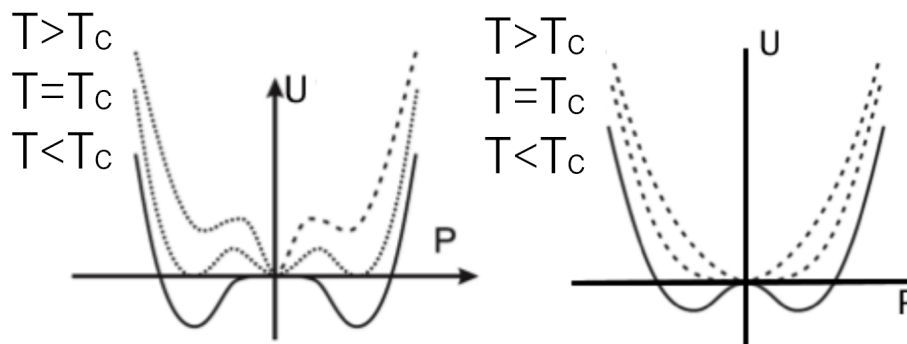


Figure 1.4: Left: Gibbs free energy vs. order parameter of a first order transition. Right: Gibbs free energy vs. order parameter of a higher order transition.

1.1.3 Electronic Configurations of Transition Metals

Transition metals contain several shells of electrons; the first few electron shells ($1s^2$, $2p^6$, $2s^2$) are filled, and depending on the row in the period table, there can be several more filled shells, followed by a partially filled d electron band. In transition metals these unfilled electrons are generally non-localized, which means in transition metals, the d electrons form an electron cloud around the atoms which behaves as an electron band. Unpaired d electrons contribute spin to the system which act as magnetic dipoles in the system. This will be discussed further in section 1.2. Most transition metals are paramagnetic at room temperature, so these spins are randomly oriented, but in elements such as iron, the unpaired electrons are oriented ferromagnetically at room temperature.

The shape of the d-orbitals will depend on the most energetically favorable configuration of electrons. There are five possible shapes (Fig. 1.5), all of which are energetically equal for a single atom. The shape of d-orbitals in the solid state depends on the electronic environment surrounding the atom, as well as the crystal structure of the material. The expectation value

of the d-orbital radii will become important as I begin exploring the magnetic behavior of alloys under pressure, as the d-orbital extent will change with pressure along with atomic spacing.

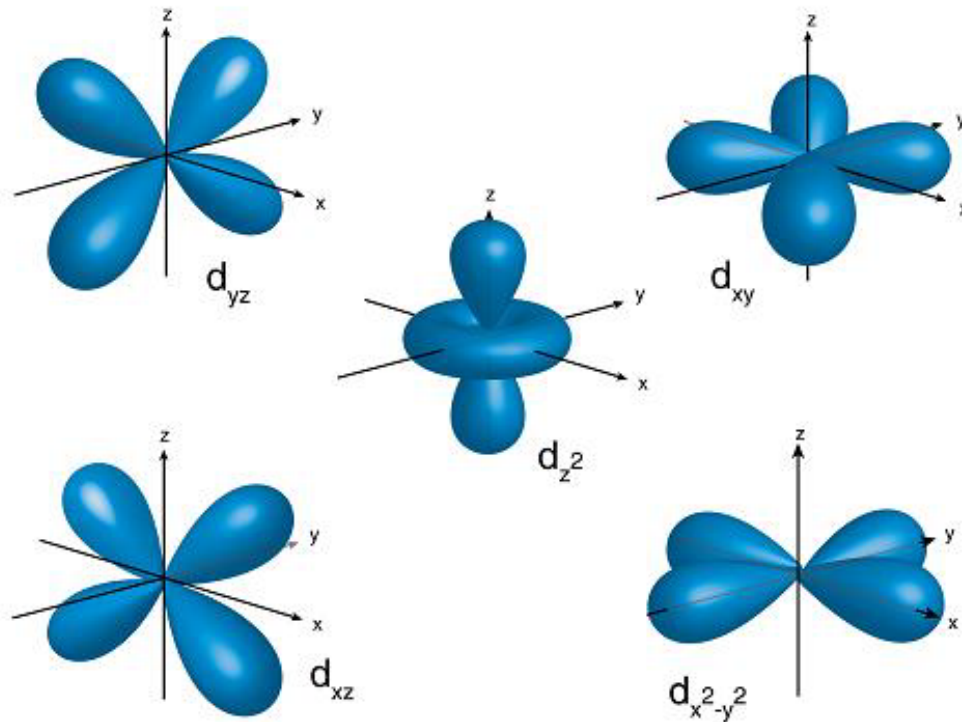


Figure 1.5: The five types of d-orbital shapes. The direction of the lobes will depend on the crystal structure and electronic environment of the atoms.

1.2 Soft Magnetic Materials

1.2.1 Ferromagnetism

Magnetism is a phenomenon in which an atoms electrons orient such that the atom will experience a torque causing it to align with a magnetic field. Typically, electrons will pair up in opposite orientations due to the Pauli exclusion principle, and unpaired electrons will orient in random directions such that there is no alignment. However, in specific atoms (Fe, Ni, Co, and Gd at room temperature), these unpaired electrons will orient in the same

direction to create a net spin on the atom. Because transition metals form a shared electron cloud in solids, this net spin is not necessarily an integer. This spin is also known as a magnetic dipole, also known as a magnetic moment.

There are several types of magnetic response to a magnetic field; paramagnetism, ferromagnetism, antiferromagnetism, and diamagnetism are the most common and the most relevant to this work. Diamagnetic materials are oriented anti-parallel to magnetic fields, and thus experience a small moment alignment against the direction of a field. Paramagnetic materials have magnetic dipoles which are oriented in random directions (Fig. 1.6a), and the sum of these moments is zero. Under the application of a magnetic field, these moments will align along the field direction, but when the field is removed they revert back to disordered orientations. Paramagnetism is typically the disordered phase above the critical temperature at which ordered magnetic phases spontaneously arise. Ferromagnetism is a state in which a material's magnetic dipoles are aligned along, or precessing about, one axis (Fig. 1.6b). The exact degree of directional alignment is temperature dependent, and can be described by an order parameter, $\frac{M}{M_s}$ where M is the magnetization at temperature T , and M_s is the saturation magnetization, which is M at temperature $T=0\text{K}$. This order parameter goes to 1 at $T=0\text{K}$, and 0 at $T=T_c$ (the Curie temperature, the critical point at which the net moment is 0). Antiferromagnetism is a state in which the magnetic dipoles are aligned in opposing directions (Fig. 1.6c), so the net magnetic moment is 0, typically arising when moments are too close for ferromagnetism to be energetically favorable. The critical temperature of an antiferromagnetic material is known as the Néel temperature (T_n). The moments in an antiferromagnetic phase behave similarly to those in a ferromagnetic phase in that their orientation with respect to the axis of alignment is dependent on the temperature, but it is defined by two order parameters which correspond to the spins which are pointed "up", and the spins which are pointed "down", essentially forming magnetic sublattices. Each order parameter is still defined as 1 at $T=0\text{K}$ and 0 at $T=T_n$; the only difference is that the sum of the moments remains 0 regardless of the order parameters.

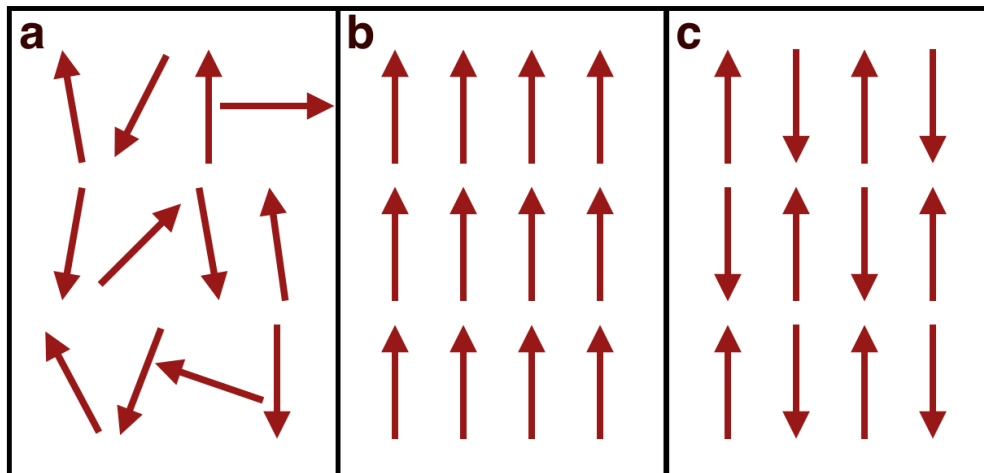


Figure 1.6: Orientation of magnetic moments: (A) paramagnetic, (B) ferromagnetic, and (C) antiferromagnetic.

The critical temperatures are where a phase transition between magnetic phases takes place, and is considered a non-disruptive, higher-order transition due to the fact that it is a continuous transition. However, there are some magnetic transitions that occur discontinuously due to a structural phase transition at the same temperature, known as a first order magneto-structural phase transition (FOMP). This leads to a discontinuous change in the magnetization at the transition temperature. The normalized magnetization, which is the magnetization divided by the saturation magnetization at 0K, is the “order parameter” for a magnetic phase, indicating how well-aligned the magnetic moments are. Fig. 1.7 shows how this order parameter changes for a higher order transition (left) versus a first order transition (right).

The saturation magnetization correlates to the number of electrons in an atom, and it is the largest magnetization possible for a material given a sufficiently large field applied at 0K (where all moments should be completely parallel). The Slater-Pauling curve (Fig. 1.8) is an empirical curve showing the maximum magnetization achievable for a given number of electrons (on average). It is important to note that the magnetization of each magnetic element is not proportional to T_c ; iron (Fe) has a larger magnetization but lower T_c than cobalt

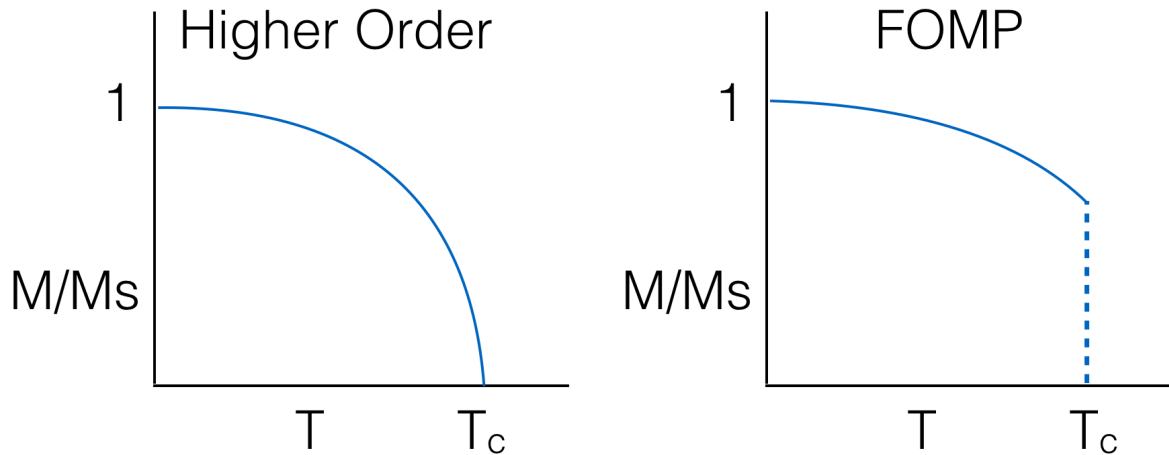


Figure 1.7: Magnetization vs. temperature behavior for higher order vs. first order magneto-structural phase transitions.

(Co). However, most additions which lower T_c will cause a lower M_s . The ferromagnetic elements iron, cobalt, and nickel lie on the curve, while binary alloy systems containing at least one of each have a branch lying on the curve, and a branch that extends underneath it. This demonstrates that the Fe-Co binary represents the maximum magnetization per atom achievable in an alloy system as any other additions lower the average moment. The binary alloys with branches extending underneath the curve have electronic interactions which lower the magnetization due to d-orbital filling, and some may also have lower magnetization due to the presence of antiferromagnetic exchange, such as in the Co-Mn binary alloy.

Beyond the type of transition, ferromagnetic materials can be categorized by their magnetic hardness. Hardness is a measure of the strength of the magnetic field which is required to reverse the magnetization direction of the material. When a ferromagnetic material is exposed to an external magnetic field, the material will require a specific field to reach saturation (Fig. 1.9), at which point the magnetization of the material will no longer increase. [2] When this field is removed, however, the magnetization of the material may not return to 0. Magnetic hardness affect the remnant magnetization, which is the magnetization of the material at zero field after being saturated in field. The strength of the field being applied in the opposite direction needed to return the magnetization back

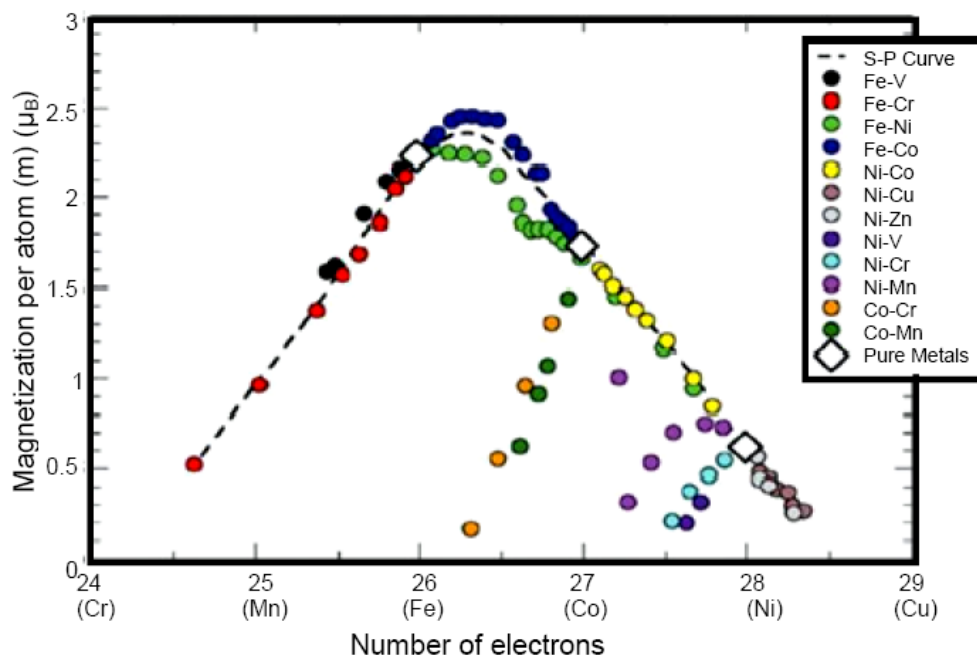


Figure 1.8: The Slater-Pauling curve, showing the relationship between number of electrons and magnetization. Reprinted with permission from J.C. Slater, *Physical Review* 49, pg. 931, 1936. Copyright 2019 by the American Physical Society. [1]

to 0 is known as the coercivity, and the larger the coercivity, the more magnetically “hard” a material is. Larger coercivity materials are useful for applications requiring a magnetic material to hold information, such as magnetic media, whereas small coercivity materials are useful for applications in which the magnetization will be reversed rapidly with small loss of energy, such as in transformer cores.

1.2.2 Exchange Interactions

The solution of Schrödinger’s equation for multi-electron systems, as first addressed for molecular orbitals, starts with a many electron wavefunction:

$$\Psi = \Psi_{\alpha,\alpha}(1)\Psi_{\alpha,\beta}(2)\cdots\Psi_{z,\alpha}(N-1)\Psi_{z,\beta}(N) \quad (1.2)$$

where $\Psi_{\alpha,\alpha}(1)$ is the wavefunction of electron 1 occupying molecular orbital 1 with spin

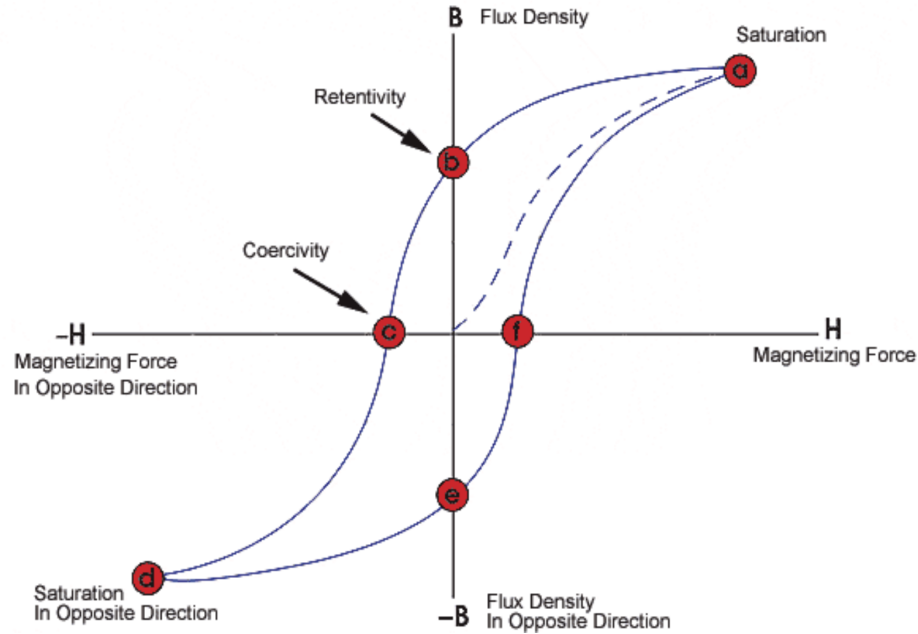


Figure 1.9: A B-H loop for a ferromagnetic material. [2]

α , electron 2's wavefunction 2 occupying molecular orbital 1 with spin β , ... However, this many electron wavefunction lacks antisymmetry required by the exclusion principle and is replaced by a Slater determinantal wavefunction [24] :

$$\Psi = \sqrt{1/N!} \det |\Psi_{\alpha,\alpha}(1)\Psi_{\alpha,\beta}(2) \cdots \Psi_{z,\alpha}(N-1)\Psi_{z,\beta}(N)| \quad (1.3)$$

which satisfy the Hartree Fock equations [24] for the ground state:

$$f_1 \Psi_{\alpha,\sigma}(1) = \varepsilon \Psi_{\alpha,\sigma}(1) = [h_1 + \sum_j \{2J_1(1) - K_1(1)\}] \Psi_{\alpha,\sigma}(1) \quad (1.4)$$

with σ either the α or β spin and the term in square brackets is the Fock operator, f_1 . h_1 is the atomic Hamiltonian and $J_1(1)$ is the electron-electron Coulomb operator for the j th electron. For many electron systems, interchange of the electrons is accounted for in the electron-electron exchange operator for the j th electron:

$$K_j(1)\Psi_\alpha(1) = \left\{ \int \Psi_j^*(2)\Psi_\alpha(2)\left(\frac{1}{r_{12}}\right)d\tau_2 \right\} \Psi_j(1) \quad (1.5)$$

In the context of mean field theory [25], Heisenberg exchange interactions [26] are linearly related to T_c . While the Hartree-Fock equations are on firm theoretical footing, the solution of Schrodinger's equation with Slater determinantal wavefunctions become computationally intractable with increasing number of electrons. Hartree-Fock theory has been supplanted by considerations of a self-consistent field approximation [27] and the construction of an exchange correlation potential in local spin density functional theory (DFT) [28, 29]. There are now many DFT calculations of exchange interactions in transition metal alloys [30].

Calculation of exchange interactions in the solid state are treated most correctly in solutions to relativistic Dirac equations [31]. Exchange integrals in the context of the Heitler-London theory [32] of the chemical bond were used to construct the Bethe-Slater curve [33–35], predicting the dependence of J_{ex} on D/d , where D is the transition metal interatomic spacing and d is the spatial extent of magnetic d-orbitals (Fig. 1.10). In practice, exchange is more often discussed semi-empirically using Bethe-Slater curve predictions of 3d transition metal magnetic states. Since the Bethe-Slater curve is rooted in atomic bonding theory it may also be of future interest to view it in the context of recent universal binding energy ideas [36]. The magnetic energy term between magnetic dipoles is known as exchange energy, and each pair of neighboring atoms have an exchange interaction. The magnetic energy term is defined by the Heisenburg Hamiltonian:

$$\mathcal{H} = - \sum_{i,j} J \langle \vec{S}_i \cdot \vec{S}_j \rangle \quad (1.6)$$

where J is the exchange constant, and \vec{S}_i is the spin angular momentum of a given atom in the system. Exact calculation of the exchange energies of ferromagnets from this equation yields values much lower than the experimentally calculated values, and thus supplemental models have been employed to better explain ferromagnetism [37]. In general, the exchange

energy for ferromagnetic metals can be estimated from their T_c values with the equation:

$$T_c \approx \frac{2\langle J \rangle}{3k_b} \quad (1.7)$$

The Bethe-Slater curve allows us to visualize the relative exchange strength of each atomic moment [33,34]. This curve has broadly been used to explain differences in exchange interactions with changes in atomic spacing, particularly when antiferromagnetic exchange becomes ferromagnetic at larger distances in compounds containing Mn, for example. [38–40] This curve could be used to predict the effect of applied pressure (which decreases the atomic spacing) on the strength of individual exchange interactions. It can also be used to predict the strength of alloys which are next to each other on the curve. However, it's important to remember that the curve is not an accurate prediction tool for non-adjacent exchange interactions, so its utility as a predictor of magnetic behavior in more complex alloys is limited, and I go into a more deep exploration of this in chapter 5.

1.3 Magnetic Refrigeration

1.3.1 The Magnetocaloric Effect

The magnetocaloric effect is the change in temperature experienced by all ferromagnetic materials upon the application or removal of a magnetic field in an adiabatic environment. This occurs because the magnetic entropy $\Delta S_{magnetic}$ of the system decreases upon application of a magnetic field; in an adiabatic reaction, the total entropy change must remain zero, and thus the thermal entropy $\Delta S_{thermal}$ of the system increases, causing an increase in the temperature of the system:

$$\Delta S(T)_{\Delta H} = \left(\Delta S_{magnetic}(T)_{H_f} - \Delta S_{thermal}(T)_{H_i} \right)_T \geq 0 \quad (1.8)$$

The opposite occurs when the field is removed, and the decrease in temperature upon

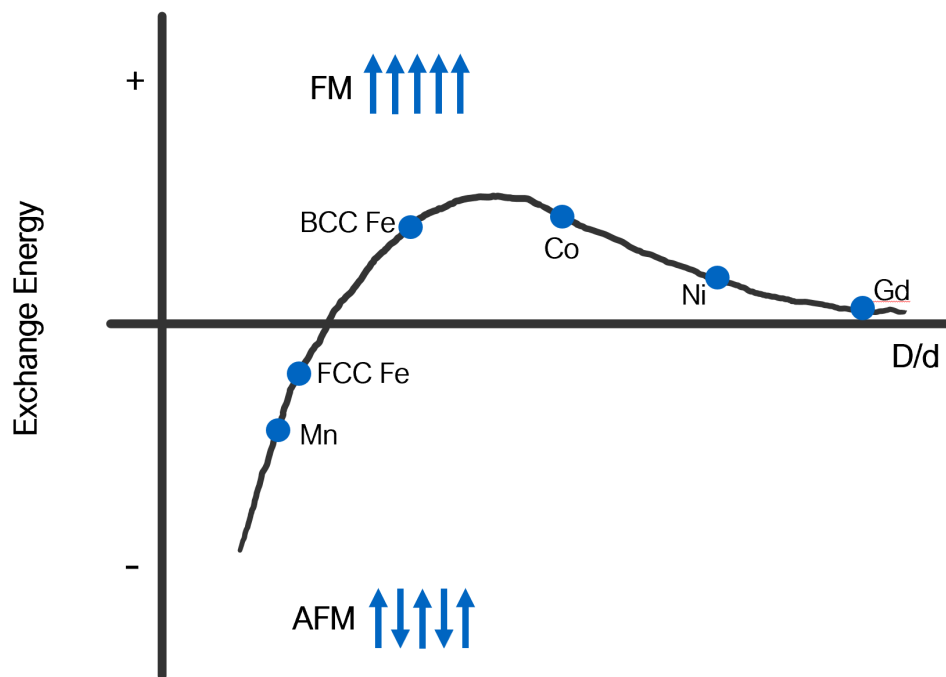


Figure 1.10: The Bethe-Slater curve, demonstrating the relationship between atomic spacing normalized by d-orbital extent and exchange energy.

removal is the most important step in the magnetocaloric cycle for magnetic refrigeration. This cooling and heating cycle is analogous to the conventional vapor refrigeration cycle, which relies on the drop in temperature a vapor experiences as it is decompressed (Fig. 1.11). In both cases, a heat exchanger will remove heat from the system after the first adiabatic cycle and will be cooled during the second.

As a sample will equilibrate with the surrounding system given time, it is difficult to measure the thermal entropy change of a material directly. However, we can calculate the magnetic entropy change with an equation derived from the magnetic Gibbs free energy:

$$G = U - TS + PV - HM \quad (1.9)$$

where the magnetic energy term is HM , the magnetic field multiplied by the magnetization. The differential Gibbs free energy can then be written in two ways, depending on which value

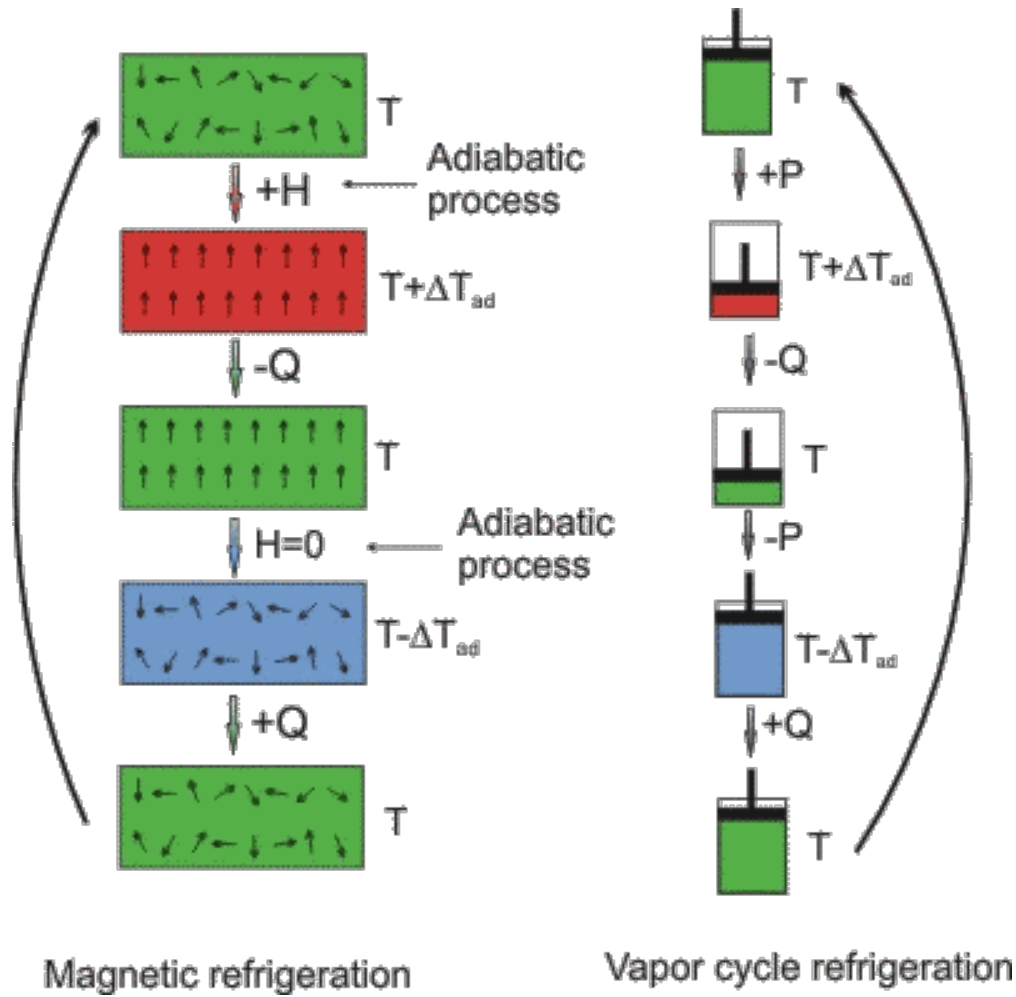


Figure 1.11: The magnetocaloric effect in a full refrigeration cycle, compared with a conventional vapor refrigeration cycle.

in the magnetic energy is considered to be the independent variable. For this calculation, the advantageous differential is:

$$dG = VdP - SdT - MdH \quad (1.10)$$

From this form of the differential Gibbs energy, we can obtain the Maxwell relation:

$$\left(\frac{\partial S_M(T, H)}{\partial H} \right)_T = \left(\frac{\partial M(T, H)}{\partial T} \right)_H \quad (1.11)$$

which can then be rearranged to express the change in magnetic entropy:

$$\Delta S_M(T)_H = \int_0^{H_{max}} \left(\frac{\partial M}{\partial T} \right)_H dH \quad (1.12)$$

To calculate ΔS_M in equation 1.12, the standard method is to measure isothermal magnetization versus field data for a material over a range of temperatures in regular intervals (typically 5K-10K) spanning from above T_c to below it (Fig. 1.12). $\frac{dM}{dT}$ is the difference in M between two temperatures, and ΔS_M is this difference integrated through the entire applied field; the corresponding value of T for this data point is the average of the two temperatures (Fig. 1.13). ΔS_M is negative, but plots often show the absolute value of S to reflect the thermal entropy change. The area under the positive curve is equal to the cooling capacity of the system. The ΔS curve is most useful when we are able to determine the full width at half maximum (FWHM) values, so a larger range of isotherms is preferable for these measurements [41]. The broadness of the ΔS curve will depend on the type of magnetic transition being assessed, as it is essentially the slope of the magnetization versus temperature curve. First order magneto-structural transitions will exhibit large magnetocaloric responses over a small temperature range, whereas higher order transitions tend to have small responses with a broader FWHM, so for materials with a higher order transition in particular, it may require a span of hundreds of Kelvin to encapsulate the entire magnetocaloric effect in the ΔS curve.

Because of the vast differences between the shape and size of ΔS curves, magnetocaloric materials are commonly compared using a figure of merit known as the refrigeration capacity (RC) which takes into account both the temperature range at FWHM and the magnitude of the entropy change for a given material at a given field (as ΔS and RC will scale with applied field [42]). The refrigeration capacity can be measured many ways, which are visualized in Fig. 1.14. The most commonly reported RC value is defined as the peak entropy ΔS_{max} multiplied by the temperature span at the FWHM of the entropy curve:

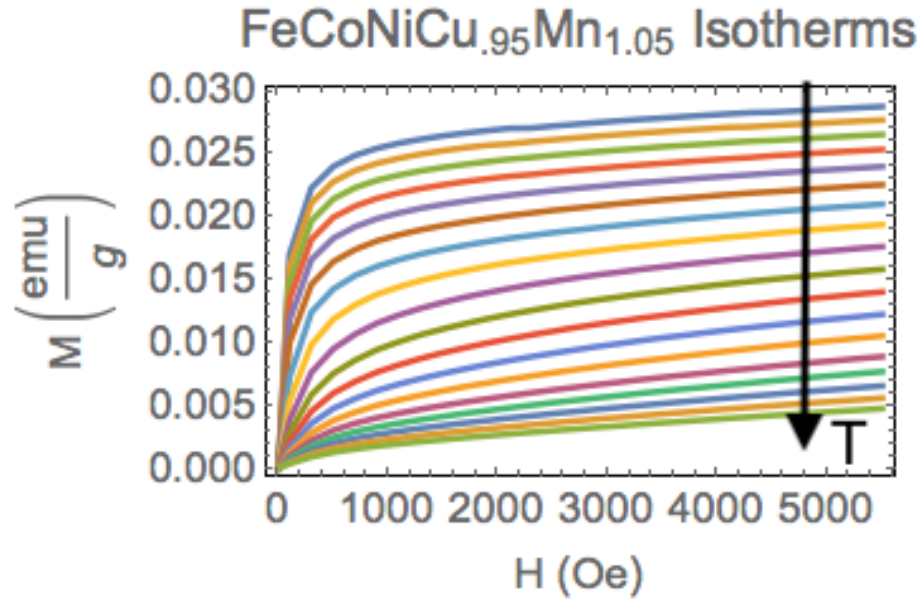


Figure 1.12: Isothermal magnetization versus field measurements spanning the working temperature range (230K to 370K in this plot) of a magnetocaloric material, which can be used to calculate the total change in magnetic entropy.

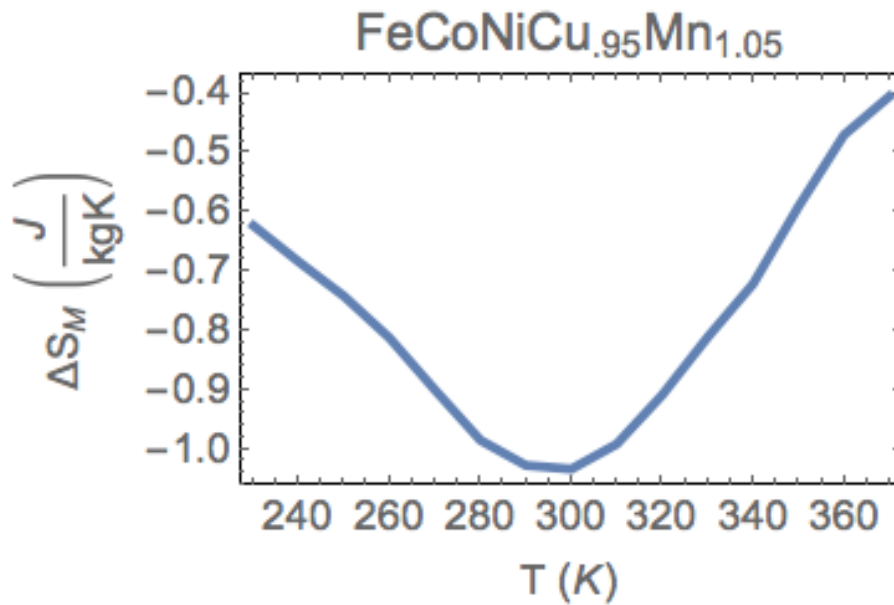


Figure 1.13: Calculated change in magnetic entropy vs. temperature from the measured isotherms, which is equal to the change in thermal entropy.

$$RC_{FWHM} = |\Delta S_{peak} \Delta T_{FWHM}| \quad (1.13)$$

This definition allows for easy calculation of RC as it does not require integration over the ΔS curve or require individual curve fitting, but it overestimates the total capacity for cooling for a given material. A more accurate value of RC is obtained by integrating under (or over, if the absolute value of ΔS_M is not taken) the ΔS curve over the range of temperatures at FWHM (RC_{Area} in Fig. 1.14). This calculation accounts for the shape of the curve, and assumes that a magnetocaloric material will only be efficient enough for commercial use within this maximum entropy change range. The third method of calculation (RC_{WP}) was first proposed by Wood and Potter in 1985, and it is the area of the largest rectangle possible to draw under the ΔS curve. Practically, this results in a rectangle multiplying the cycle's ΔS at the coldest working temperature by the entire temperature span, which results in an underestimate of RC. This is less straightforward to calculate, but it means that asymmetry of the curve is penalized [43] Each method has advantages and disadvantages, but for ease of calculation and to maximize reported figures of merit, the standard parameter for comparison is RC_{FWHM} .

There are a few considerations to make when comparing magnetocaloric materials using their reported RC values. RC values will scale linearly with applied field, so values reported for $H_{max}=1.5T$ can be multiplied by 3.33 to get an estimate of the RC at 5T. However, both the FWHM temperature range and T_{peak} will shift to higher temperatures as field is increased, so materials with T_{peak} reported at room temperature for a specific applied field will experience a ΔS peak at a higher temperature for a larger field [42]. Additionally, paying attention to the FWHM range is important. A material with an extremely large ΔS and small FWHM, or small ΔS but large FWHM, will exhibit a large RC value that does not reflect its utility in magnetocaloric applications, in which a working temperature range of 30-50K is desirable.

The other figure of merit necessary when characterizing a magnetocaloric material is the adiabatic temperature change over one cooling cycle (demagnetization) at ΔS . This is possible to measure directly, but it can also be calculated from the existing magnetization

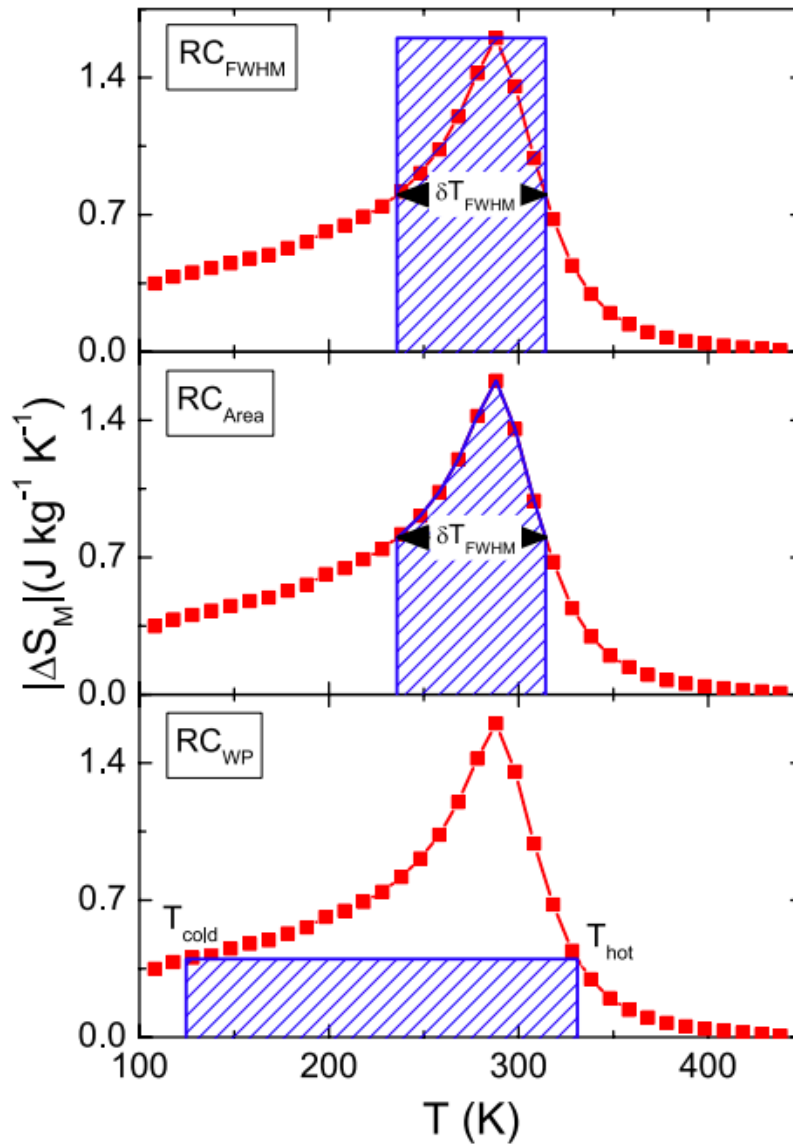


Figure 1.14: Various methods of calculating refrigeration capacity for a given ΔS curve. [3]

data if the material's heat capacity is known. The expression can be derived from the second differential form of the Gibbs free energy, in which the magnetic differential term is now HdM :

$$dG = VdP - SdT + HdM \quad (1.14)$$

from which we can obtain the Maxwell relation:

$$-\left(\frac{\partial H}{\partial T}\right)_M = \left(\frac{\partial S}{\partial M}\right)_T \quad (1.15)$$

This can be inverted, and the term on the right can be broken into multiplied partial derivatives:

$$\left(\frac{\partial T}{\partial H}\right)_M = -\left(\frac{\partial M}{\partial S}\right)_T = \left(\frac{\partial M}{\partial T}\right)\left(\frac{\partial T}{\partial S}\right) \quad (1.16)$$

From the definition of heat capacity, we can make the substitution:

$$\left(\frac{\partial T}{\partial S}\right) = \frac{T}{C_p} \quad (1.17)$$

to obtain a similar form to equation 1.12:

$$\Delta T_{ad}(T, H_{max}) = \int_{H_{max}}^0 \frac{T}{C_p(T, H)} \left(\frac{\partial M}{\partial T}\right) dH \quad (1.18)$$

where ΔT_{ad} is the temperature change over a single adiabatic demagnetization cycle starting at a given value of T. H_{max} is the applied field that is removed, and C_p is the heat capacity of the material at the beginning temperature T. This equation can be simplified by dropping the field dependence of the heat capacity, which has been shown to not be significantly altered by magnetic fields [44]. In doing this, the term $\frac{T}{C_p(T)}$ is constant and can be pulled out of the integral. The remaining integral is then equivalent to equation 1.12, so the integral can be replaced by the ΔS value at the desired temperature. With this simplification, the temperature change over one cycle at the peak entropy change can be written as:

$$\Delta T_{ad} = -\left(\frac{T}{C_p}\right) |\Delta S_{max}| \quad (1.19)$$

This value gives us an upper limit on the temperature change possible to achieve in one magnetocaloric cycle, which also gives us a rough idea of how many cycles it would

take to reach the desired temperature. Because this is more directly related to their use in magnetic refrigeration applications, it is also an important figure of merit when considering the viability of a magnetocaloric material for commercial use. A value of ΔT_{ad} between 5K-10K would be considered commercially viable.

1.3.2 Applications of Magnetocaloric Cooling

The magnetocaloric effect has been used for cooling to very low temperatures since 1933, when Giauque et al. developed the first magnetocaloric system to obtain temperatures below 1 Kelvin. [45]. This system required that their material first be cooled to temperatures of a few Kelvin with liquid helium because the magnetocaloric effect was only large in that temperature range. In general, the magnetocaloric effect is largest just below the Curie temperature (T_c) of a material [46]. Thus, a material with a room temperature T_c (300K) would be ideal for commercial refrigeration applications. Commercialized magnetocaloric refrigeration is of interest because it offers more energy efficiency than conventional gas compression refrigeration by up to 20%, and has the additional advantage of being environmentally friendly as it does not require the use of ozone depleting gases. [47, 48] The majority of MCE research focuses on developing materials with T_c around room temperature because of the difficulty of lowering T_c without suppressing M_s to a prohibitively low value. The specific materials that have been studied for these applications are discussed in more detail in section 1.3.3. However, the magnetocaloric material is only one component of a magnetic refrigerator, and there are several design considerations that must be made in order to maximize efficiency [4].

One factor is the thermodynamic cycle of heating and cooling used in the system. There are four primary types of cycle: Carnot, Ericsson, Brayton, and Active Magnetic Regenerator (AMR). The Carnot cycle (Fig. 1.15a), which is the most efficient, is the process depicted in Fig. 1.11 and is comprised of two adiabatic processes (in which the total entropy change is 0) and two isothermal processes (in which the material exchanges heat with a hot or cold

temperature sink). The Ericsson cycle (Fig. 1.15b), which is comprised of two isothermal processes and two isofield processes (where the field is held constant as the temperature changes), relies on a regenerator to transfer heat between parts of the cycle, alternating between absorbing and releasing heat when needed. The Brayton cycle (Fig. 1.15c) is made up of two isofield processes and two adiabatic processes, and does not necessarily require a regenerator during cooling. The AMR cycle is similar to the Ericsson cycle, but it uses the magnetocaloric material as both a refrigerant and a regenerator, and it is almost as efficient as the Carnot cycle for room temperature magnetic refrigeration. For this reason, most MCE refrigerator designs rely on the Carnot or AMR cycles. [4]

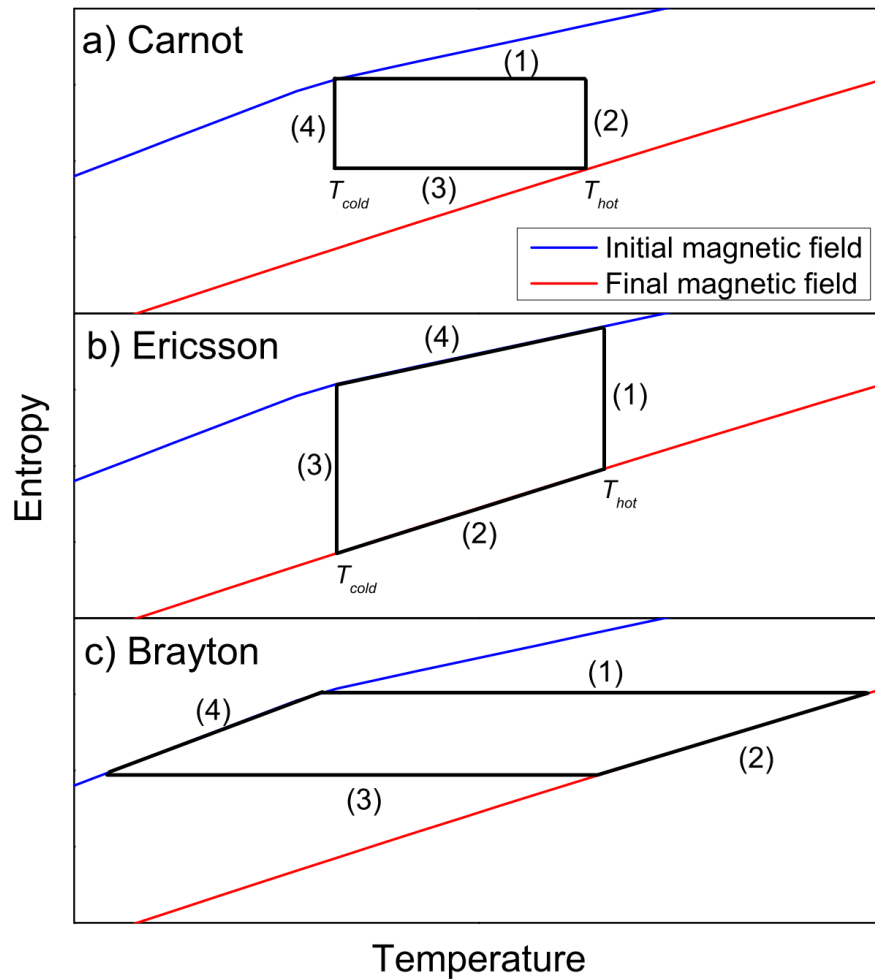


Figure 1.15: Different thermodynamic cycles possible for magnetocaloric refrigeration systems. [4]

There have been many designs of magnetic refrigerators proposed, and aside from the thermodynamic cycle on which they rely, they can also be conceptually differentiated by the type of magnet used for the magnetization of the magnetocaloric component [49]. The least common magnets used are superconducting magnets, which were used in the first magnetic refrigeration device, but have not been included in many others due to the difficulty of keeping the superconductor below its critical temperature, which requires liquid nitrogen and extra energy expenditure to maintain it. [50] Non-superconducting electromagnets are a more popular design feature in magnetic refrigerators, but because electricity is needed to send current through the coils of the magnet, these designs are generally less common as well [51, 52]. The most promising designs feature permanent magnets because they don't require electric generation [53]. There have been several attempts to quantify the effectiveness of permanent magnet refrigeration designs, and the figure of merit in these studies have usually focused on the mass of the magnets and magnetocaloric materials, as well as the volume of the region of high magnetic flux density. [54, 55]. Bjørk et al. defined parameter, P_{field} , which is the amount of time the magnetic flux is being “wasted”, i.e. how much time spent without a magnetocaloric sample in the field. This parameter is included in the figure of merit they defined, Λ_{cool} :

$$\Lambda_{cool} = \left(\langle B^{2/3} \rangle - \langle B_{out}^{2/3} \rangle \right) \frac{V_{field}}{V_{mag}} P_{field} \quad (1.20)$$

where $\langle B^{2/3} \rangle$ is the volume average of flux density in the high flux area between the permanent magnets, $\langle B_{out}^{2/3} \rangle$ is the volume average of the flux density in the area where the magnetocaloric material is taken to be demagnetized, V_{field} is the volume of the high flux area, and V_{mag} is the volume of the permanent magnets. This figure of merit allows for robust assessment of a diverse set of designs, particularly because it normalizes by the volume of magnetic material and volume of the high flux region, reducing each design primarily to geometric efficiency. These parameters are labeled on an example design for a system

featuring a Halbach cylindrical permanent magnet (Fig. 1.16).

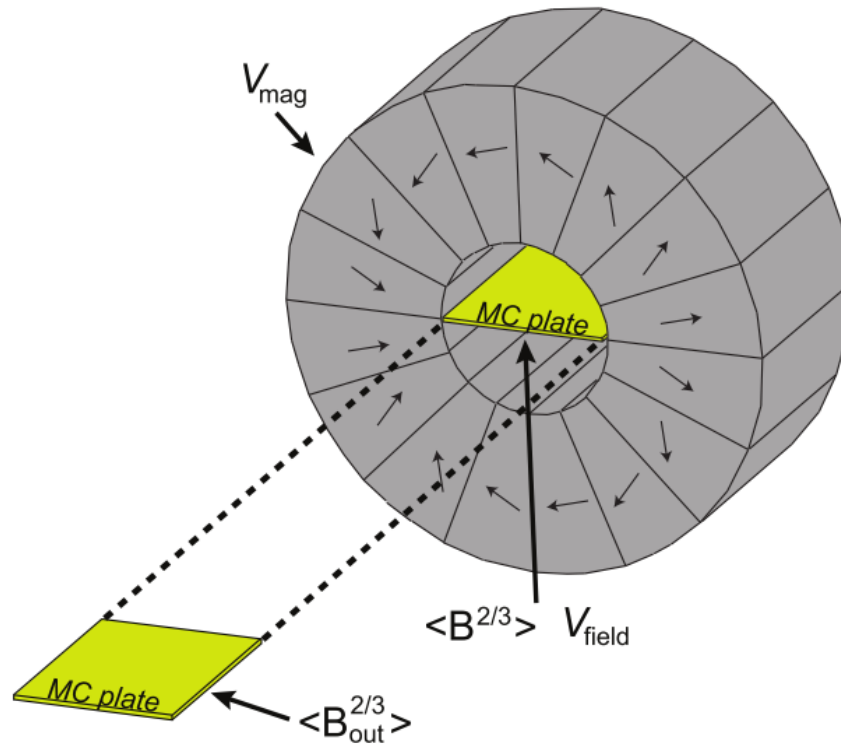


Figure 1.16: A Halbach cylinder with labelled design parameters.

The Halbach cylinder, which has a ring of permanent magnets with rotated orientations to maximize flux, is a common design feature in this type of system, which has a central cavity into which the magnetocaloric material is inserted. This design requires that the magnetocaloric component be moved while the permanent magnet remains stationary in order to vary the magnetic field felt by the magnetocaloric component. The downside of this design, however, is that it necessitates that the permanent magnet's flux be unused for half the cycle (the time during which the plate is removed) [56]. A solution to this problem is the inclusion of rotating components, such as a rotating disk made up of magnetocaloric plates that passes over a permanent magnet. This ensures that there is always a plate in the magnetic flux lines, and the cooling occurs when the plates are opposite the permanent magnet. [57]

Some refrigerator designs currently in development commercially are based around the

use of several magnetocaloric materials with different T_c values, which would be stacked in sequence. These designs rely on magnetocaloric materials with large changes in entropy over a small temperature range. On their own, a material like this would not be viable, but stacking several materials with slightly different peak transition temperatures allows each material to pass through its transition and lower the temperature of the system enough that the next material in the sequence then experiences a larger temperature change. These designs seek to bypass the issue of developing materials with broad ΔS curves, but are inefficient due to the large amount of material that is not in use during each cycle (in the stack of MCE materials). These designs can also fail quickly if a demagnetization cycle does not result in the correct temperature change, or if the synthesis of the materials in each plate does not result in the exact correct composition to achieve the desired T_c . Thus, the focus of most designs is maximizing efficiency of broader transitions that do not require stacking of different materials. However, most designs do general involve stacks of thin plates of magnetocaloric material for the purpose of efficient heat removal. Removing excess heat with cooling fluid works more efficiently with greater surface area contact with the magnetocaloric material, so designs of MCE refrigerators typically include the material pressed into stacks of thin plates, or other porous structures which allow for fluid flow. [58, 59]

Thus, in addition to the refrigeration capacity and Curie temperature of a magnetic material, there are other factors which much be accounted for when determining a material's fitness for magnetic refrigeration applications, such as its heat capacity and thermal conductivity, both of which affect the ability of the system to change temperature and expel excess heat. These properties can be measured experimentally for a clearer picture of the potential for magnetic refrigeration with a specific material. Other properties, such as corrosion resistance, become important when we consider the design of the magnetic refrigerators because the magnetocaloric component will be continuously interacting with cooling fluid. When modeling magnetocaloric systems, then, it is necessary to account for the cooling fluid viscosity, heat capacity, and flow rate, as well as the time required for one cycle and total

system size. [56]

Magnetocaloric materials can also be utilized in more specialized applications, such as ferrofluidic cooling systems. Ferrofluids are stable suspensions of magnetic nanoparticles in a liquid which can be manipulated by magnetic fields. The benefit of using ferrofluids as a coolant are that the system does not require a fluid pump, as the coolant can be drawn through the system using thermal and magnetic field gradients [60]. A self pumping system (Fig. 1.17) uses the presence of a permanent magnet to draw the ferrofluid towards the heat load of the system. The heated fluid experiences a decrease in magnetization, but this magnetization increases as the ferrofluid cools and moves towards the heat sink. The thermal gradient in the system thus also produces a magnetic gradient which keeps the fluid in motion. [5, 61]

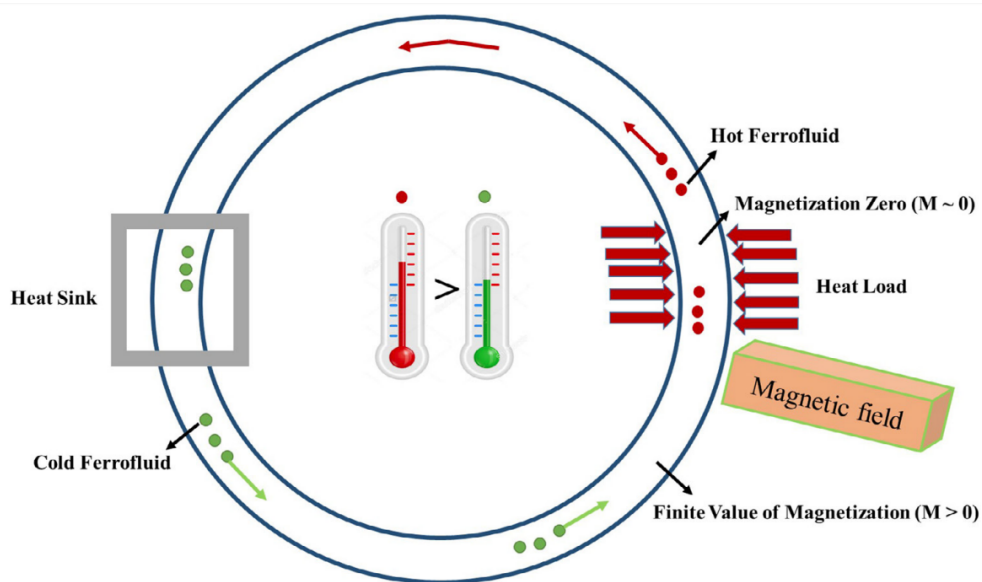


Figure 1.17: Self pumping magnetic cooling system [5]

These systems cool more efficiently when the nanoparticles have a large magnetocaloric response around the operating temperature of the system. The nanoparticles will experience a temperature decrease after passing through the heat load when they are no longer in the flux path of the permanent magnet because they will undergo demagnetization. This appli-

ation requires the additional assessment of a material's properties and structural integrity in nanoparticle form, which can be vastly different from the bulk properties.

Another specialized use for magnetocaloric cooling is in systems in which a thin film of magnetocaloric material is applied to the outside or inside of a part which is both prone to overheating, and which produces some amount of magnetic flux due to currents passing through the system. Though less well studied, I imagine some potential applications to be coatings on automotive parts and pieces in experimental measurement systems prone to overheating. Given the past studies of high entropy alloys for structural applications and oxidation resistance, magnetocaloric high entropy alloys could be uniquely suited for this specialized applications, particularly in extreme environments that will require significant structural integrity.

1.3.3 Current Magnetocaloric Materials of Interest

Magnetocaloric materials fall into two classes: (1) first order magneto-structural phase transitions (FOMP) and (2) higher order magnetic transitions. The first type, giant magnetocaloric effect (GMCE) materials, exhibit a large and narrow peak magnetic entropy change accompanying a magneto-structural phase transition. These materials exhibit a large peak entropy change, but have FWHM ranges of only a few Kelvin, and this transition is often accompanied by undesirable thermal hysteresis that prevents the magnetocaloric cooling cycle to be repeated [62–64]. Use of these materials in magnetic refrigerator requires stacking of materials with different T_c 's to span a relevant thermodynamic cycle; the pitfalls of this design were discussed in section 1.3.2. Materials with a higher order magnetic phase transition usually show a lower peak entropy change, but a broader peak results in an enhanced refrigerant capacity [47, 65, 66]. These materials have reduced hysteresis loss and tunable Curie temperature, T_c [67–69]. Optimum materials possess features of each class: (a) large peak entropy change, (b) large refrigerant capacity, (c) limited thermal hysteresis and (d) resistance to thermomechanical fatigue. This will most likely be achieved by tuning the com-

position of a system in such a way that forces the magnetic transition close to the point at which a first order transition becomes higher order, and some work has been done specifically to explore systems in which this is possible. [4, 70–72]

Gadolinium is the only element with T_c already at room temperature, but it is rare, expensive, and possesses a uniaxial crystal structure making it magnetically hard and hysteretic, and thus is not a viable option for large-scale use. Dozens of materials have been studied for their magnetocaloric properties over the past few decades, but many still rely on rare earth metals to lower T_c or have working temperature ranges outside of the desired range (i.e. much higher or lower than room temperature) [73]. Fig. 1.18 is a compilation of the major groups of magnetocaloric materials studied showing both the transition temperatures achieved and the adiabatic demagnetization temperature change with one cycle. Though large temperature changes are achieved by several material groups, the four largest ($\text{La}(\text{Fe},\text{Si})_{13}\text{H}_{0.5-1.5}$, $\text{Gd}_5\text{Si}_{1.98-2.09}\text{Ge}_{1.91-2.02}$, Fe_2P , and Ni-Mn-In-(Co)) all experience first order transitions, and thus have small working temperature ranges that hinder commercialization, as well as thermal hysteresis that results in lost energy and lower efficiency. [48]. Notable materials with higher order magnetocaloric transitions include several Gd-based alloys like $\text{Gd}_5\text{Si}_{2.5-4}\text{Ge}_{0-1.5}$, Gd_7Pd_3 and $\text{Gd}_5\text{Bi}_{0-2.5}\text{Sn}_{0.75-3}$. [74–76] $\text{Er}(\text{Co}_{0.8}\text{Fe}_{0.2})_2$, $\text{MnFeP}_{0.5}\text{As}_{0.44}\text{Ge}_{0.06}$, and Mn_3Sn_2 are other non-Gd containing MCE alloys with higher order transitions. [77–79] However, none of these materials to date are commercially viable for refrigeration due to their low value of ΔS_M or T_c not close enough to room temperature.

Previous magnetocaloric materials synthesized by the McHenry group were studied by Huseyin Ucar, and the two most promising resultant alloys are included at the bottom of Table 4.2. This research began with studies of nanocomposite alloys such as $(\text{Fe}_{70}\text{Ni}_{30})_{89}\text{Zr}_7\text{B}_4$ [80], but produced more promising magnetocaloric materials through mechanical alloying of Fe-Ni nanoparticles. Ucar et al. demonstrated that the magnetocaloric properties of these nanoparticles could be optimized by controlling the oxidation kinetics of the ball milling process in which they were produced ($\text{Fe}_{70}\text{Ni}_{30}$ in Tab. 4.2) [81]. They then explored the effect

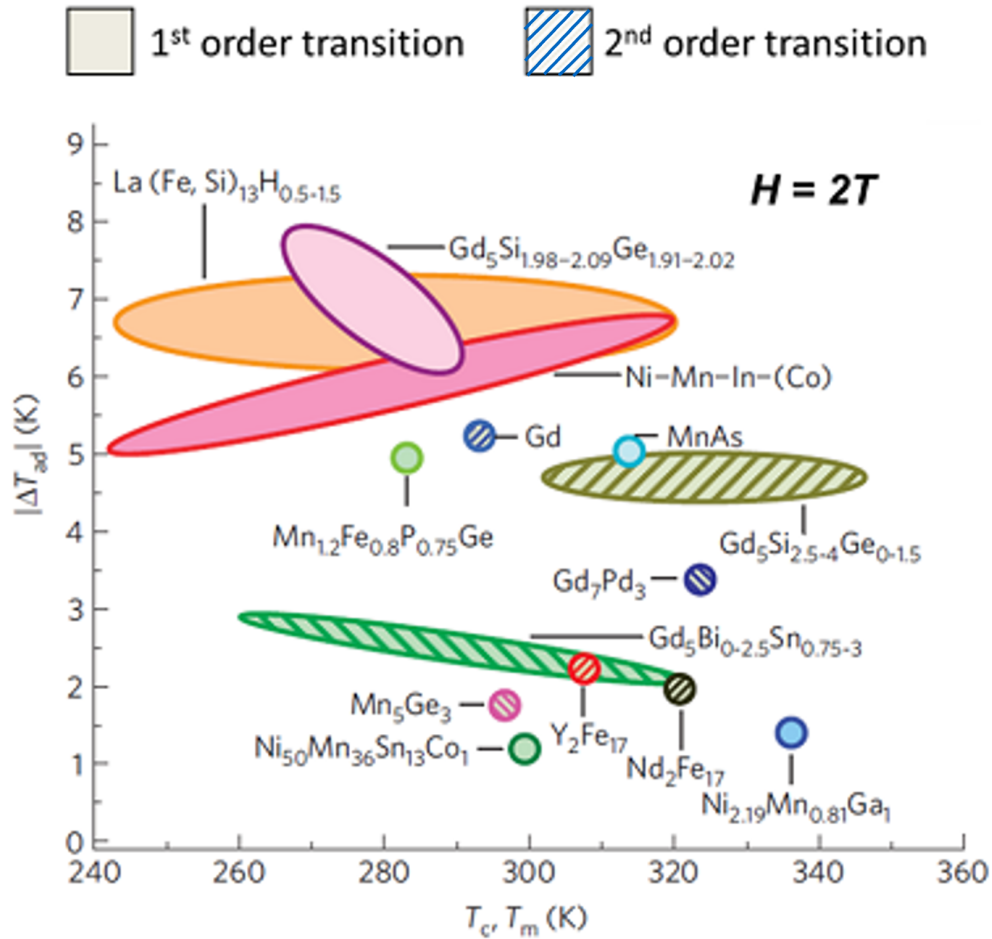


Figure 1.18: 2012 compilation of classes of MCE materials considering T_c and ΔT achieved for each. [6]

of small additions of molybdenum to these nanoparticles ($(\text{Fe}_{70}\text{Ni}_{30})_{96}\text{Mo}_4$ in Tab. 4.2) [82]. Additionally, they demonstrated the limitations of Arrott-Noakes fitting of magnetization curves, and found that a combined fit with a modified Handrich-Kobe equation better models low temperature magnetocaloric behavior. [83]

I now turn my focus to determine the viability of high entropy alloys as magnetocaloric materials. These multicomponent alloys undergo higher order magnetic transitions, which are broadened through compositional disorder-derived distributed exchange interactions [81–85]. They are of interest because the multicomponent nature allows T_c tuning and control of the refrigeration capacity through the breadth of the higher order transition. Broadening

due to random distribution of magnetic atoms on an fcc lattice [86] is less than the resulting broadening from positional disorder derived distributions previously observed in Ni-Fe-based amorphous alloys [80].

Very few magnetocaloric high entropy alloys have been studied for their magnetocaloric properties. Several groups have characterized the four component high entropy alloy Fe-CoNiCr, which has $T_c=130\text{K}$ for equiatomic compositions [87–90]. I propose working specifically with alloys containing five or more components in equiatomic amounts given that the most viable four component magnetic alloys (those containing Fe,Co,Ni and an additional metal) have already been studied and not shown to be viable alloys for these applications. Few groups have gone beyond four component magnetic HEAs. Lucas et al. [91] characterized the magnetic behavior of FeCoNiCrPd_x for $0 \leq x \leq 2$, and this alloy’s magnetocaloric behavior is included for comparison in Table 3.2 for comparison with my own alloys of focus. Na et al. identified FeCoNiCrAl as a viable high entropy alloy for magnetocalorics, as it has a $T_c=277\text{K}$ and a magnetic saturation of 25 emu/g. They do not give information on the magnetic entropy change or refrigeration capacity, so direct comparison with my alloys is not possible. [92] Koželj et al. have characterized the magnetically soft HEA FeCoNiPdCu, but not specifically for magnetocaloric applications. [93] The only rare-earth containing HEA is the alloy GdDyErHoTb, which has a larger refrigeration capacity, but at the cost of incredibly expensive materials, and an HCP crystal structure with some amount of phase segregation suggesting that it is not a true solid solution. [94]

1.4 High Entropy Alloys

1.4.1 Structure and Physics

There are several competing definitions of what classifies as a high entropy alloy, but they are most broadly defined as alloys containing three or more elements in close to equiatomic proportion, which are randomly distributed in on a crystal lattice (Fig. 1.19) [95].

Some sources raise this number to four or five elements based on calculations of the configurational entropy [96]. This randomized distribution on a crystal lattice is known as a solid solution, and there are several factors that determine whether a set of atoms will form a solid solution under the proper synthesis conditions (rapid solidification). The Hume-Rothery rules, developed by Oxford metallurgist William Hume-Rothery, are a set of general parameters by which a solute in a metal must abide in order to dissolve into that metal [97–100]:

- The atomic radii of the solvent and solutes differ by less than 15%
- The crystal structure of the solvent and solutes must be similar
- The solvent/solutes have similar electron valency
- The solvent/solutes have similar electronegativity

There are exceptions to these rules, particularly the condition that the crystal structure of the elemental components be similar, but the general accuracy of these rules have been shown to be empirically true in countless alloy systems. Though Hume-Rothery's rules were written based mostly off of his research on two-component alloys, these rules are still valid for more complex systems, including high entropy alloys. When a single solute does not dissolve in a solvent, the result is decomposition which forms clusters of pure solute, or formation of intermetallics. This decomposition is possible in alloys intended to be high entropy if they still form as crystalline structures. However, when considering a system with several atomic species like a high entropy alloy, if the Hume-Rothery rules are not followed, it may also take the form of a metallic glass. Metallic glasses are amorphous disordered metal alloys formed through rapid solidification, and generally they do not require the atomic species to be in equiatomic amounts.

The complex interactions between multiple atomic components makes predicting what will successfully form a single phase alloy more difficult, so the Hume-Rothery rules alone are not enough to assess the viability of a set of atoms to form a high entropy alloy. The total

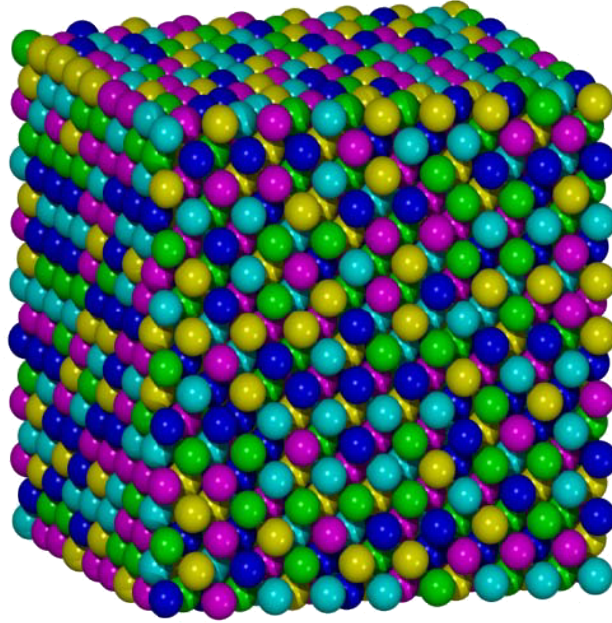


Figure 1.19: Rendering of a 5-component high entropy alloy. [7]

energy of the system is also important, particularly the entropy terms of the system. The most significant is the configurational entropy, which is determined by the mole fractions of each component of the alloy:

$$\Delta S_{config} = -R \sum_i X_i \ln(X_i) \quad (1.21)$$

The broadest definition includes alloys containing only three components, and there have been several three and four component high entropy alloys identified such as MnNiFe, CoCrMnNi, CoFeMnNi, TaNbVTi, and WNbMoTa. [101–103] However, Yeh’s definition of a high entropy alloys is an alloy with a composition of at least five elements because that number has been calculated to be the point at which the mixing entropy typically balances the mixing enthalpy and allows for the formation of a solid solution [96]. The mixing enthalpy will be dependent on the electronegativity and valency of each atom, considerations already made by the Hume-Rothery rules. Troparevsky et al. assessed the efficacy of predicting the total mixing enthalpy of a system using an enthalpy matrix made up of binary alloy terms

and demonstrated that this predicts to a large degree whether a system will be stable, but they found that this is still not entirely straightforward or accurate for some systems, for example CrMnFeTiNi, which precipitates a second phase despite having the same calculated mixing enthalpy as CrMnFeCoNi, which does not. [104] Several groups have assessed other parameters for potential correlations to high entropy alloy formation, but are unsuccessful in finding an absolute rule. For example, Zhang et al. proposed valence electron concentration as a potential parameter for formation of solid solutions where pure face centered cubic (FCC) phases would only form when the concentration was greater than $8 e^-/\text{atom}$, but this only correlated for FeCoNiCr based alloys—the alloys containing manganese (Mn) did not follow the same rule. [105] It is also thought that lattice distortion caused by the different atomic sizes of the constituents contributes to the phase stability of the single phase, as lattice distortion hinders atomic movement and slows down diffusion of atoms. [106]. As previously discussed in terms of the Hume-Rothery rules, however, we see that there is a limit to this effect; at a certain size difference, it will no longer be energetically favorable for the atoms to fit on a crystal lattice with each other, and the structure becomes amorphous. A more in depth discussion of all of these structural considerations can be found in Miracle and Senkov's 2017 review paper on high entropy alloys [107].

1.4.2 Previous Study and Applications

High entropy alloys arose as a response to a demand for novel alloys for specialized applications, intended to improve upon the existing traditional alloy systems which contain 1 or 2 primary elements. There are around 30 traditional alloy systems that have been studied extensively, such as steels, aluminum alloys, etc. Though many new processing techniques have been developed to create alloys with novel and desirable properties, high entropy alloys introducing the idea of alloys which do not have a primary constituent. [96,107] High entropy alloys have been studied for a broad range of applications in search of attractive mechanical, electrical, thermal, and magnetic properties. The biggest draw of developing these alloys

is that the properties will be a result of a “cocktail” effect in which the properties are a composite of the properties of the constituents. For example, the oxidation resistance of an alloy is increased when some of the contributing components have greater oxidation resistance; the density of an alloy is lower when some lightweight elements are added. Increased hardness has also been reported and is thought to be caused by strain due to the presence of different atomic sizes which hinder movement of dislocations. [108]. The majority of research on high entropy alloys has been focused on structural applications, but attractive corrosion resistance or electrical properties as well as magnetic properties have been studied through the lens of HEAs as well. Magnetic high entropy alloys almost always contain iron, cobalt, and nickel to maximize the magnetic moment, but there have been attempts to create high entropy alloys with rare earth components, the most significant being the HEA GdDyErHoTb, though this alloy shows some phase segregation and thus is not a truly single phase solid solution HEA. [94] Many of the major alloy groups studied for structural applications are BCC HEAs which have a common base of Cr, Fe, and Ni. These include CrFeCoTiNi, AlCoCrCuFeNiB, AlCoCrCuFeNi, AlCoCrFeMoNi, AlCrFeMnNi, and CoCrFeNiFeNi, all of which were studied for high temperature, high strength applications such as use in turbine blades [109]. The vast majority of HEAs studied thus far contain Cr, Fe, and/or Ni, but there are a small number of HEAs based on Ti, including MnFeCoTi_{0.5–2.5}VZr, TiZrNbHfTa, TiV_{0–1}ZrNbMo, TiCrZrNbMo_{0.5}Ta_{0.5}, and NbCrMoTiAl_{0.5}, all of which were studied for mechanical properties as well. [110–112]

1.5 Hypothesis

I set out to explore several hypotheses that focus on providing evidence that magnetic high entropy alloys have properties that could make them uniquely suitable for magnetocaloric applications:

- (1) The random distribution of several magnetic atoms in high entropy alloys will result

in a broadened magnetocaloric effect which will increase the refrigeration capacity through widening the full width half max of the magnetic entropy curves.

- (2) This broadening is the summation of several discrete exchange interactions between nearest and next nearest neighbors of different atomic species in these alloys.
- (3) The compositions of these magnetic high entropy alloys can be varied to alter the magnetic properties of the alloy, such as the saturation magnetization and the Curie temperature (T_c), which must be tuned to room temperature for my materials to be viable magnetic refrigeration candidates.

After this initial exploration, I then began a deeper probing of the FeCoNiCuMn HEA for more fundamental information on the magnetic exchange interactions in the system. Mössbauer spectroscopy experiments led us to develop three more hypotheses focused on exchange interactions in the system, which I set out to provide evidence for using applied pressure experiments:

- (4) The T_c of these alloys can be shifted using applied pressure because the strength of each discrete interaction will change
- (5) The change in magnetic behavior with applied pressure will be due to a change in both atomic spacing and d-orbital spatial extent of the atomic species, and these changes will affect the individual exchange interaction strengths between atoms.
- (6) The low temperature magnetic behavior observed on zero field cooling is due to a weak antiferromagnetic phase which arises due to the large number of antiferromagnetic exchange interactions present in these alloys

I present evidence that magnetic high entropy alloys with near room temperature T_c and a broad magnetocaloric response can be synthesized in Chapter 3, and that this magnetic behavior is due to a distribution of discrete exchange interactions, which we can observe

using Mössbauer spectroscopy in Chapter 4. I also show that the composition slightly of these alloys in order to achieve room temperature T_c values, which is also discussed in Chapter 4. I present data confirming that the application of pressure will change T_c , and I present data and analysis based on the idea that the magnetic behavior depends on atomic spacing as well as d-orbital contraction in Chapter 5. Hypothesis (6) will require further work to validate or refute, but possible explanations and future experiments to explore them are discussed in Chapter 6. Further planned experiments will also expand on the exploration of the exchange interactions under the influence of pressure and temperature changes as a means to provide further evidence for hypothesis (4).

Chapter 2

Experimental Techniques and Sample Preparation

2.1 Sample Production

2.1.1 Arc Melting and Melt Spinning

Our alloys are produced in a two step process. Arc melting uses a charged plasma beam to melt together pure elemental components into a homogeneous ingot of material, and the ingot is remelted multiple times in order to encourage homogeneity of the elemental distribution. [113] The chamber and sample itself are water-cooled through copper plates. To reduce oxidation of the sample components, the chamber is pumped down to -1 atm and refilled to a slight negative pressure (-0.3 atm) with argon gas. A piece of zirconium is melted first, which removes residual oxygen from the chamber. (Fig. 2.1)

This ingot is then melt-spun, a process also known as planar flow casting (Fig. 2.2) [9]. This process requires first melting the ingot in a boron nitride crucible to 150K above its melting point using an RF induction copper coil. The opening in the crucible is situated close to a chilled, spinning wheel, and then negative pressure is used to force the melted ingot through the hole and onto the wheel. This rapidly solidifies the alloy at rates up to

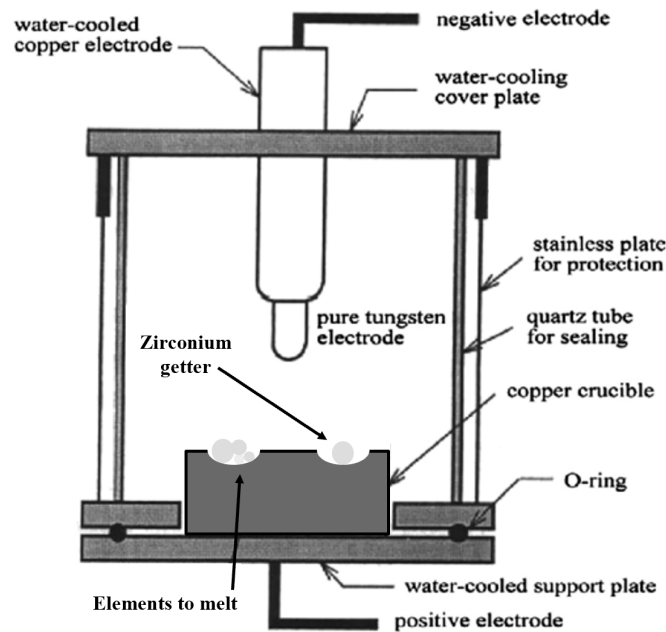


Figure 2.1: Diagram of the arc melting chamber. Alloys are heated and mixed with the plasma arc several times to ensure homogeneity. Adapted from [8]

10^6K/s , which ensures that my samples are quenched rapidly enough to form a metastable single phase solid solution. If the melt were cooled slowly, intermetallics would be likely to form. [114]

2.1.2 Thin Film Sputtering

A thin film version of the bulk high entropy alloys are also of interest because it would allow me to probe my alloy system with experiments not possible to perform on bulk samples, as long as the properties of the thin film are relatively similar to those of the bulk. One example is coherent x-ray scattering, which would allow us to observe the amount of magnetic (and atomic) disorder in my system at the nanometer scale. There are several experiments that rely on reflectance measurements which would require a highly polished, atomically flat sample as well.

I sputtered thin films in an AJA Orion Series sputtering system with the help of Vara

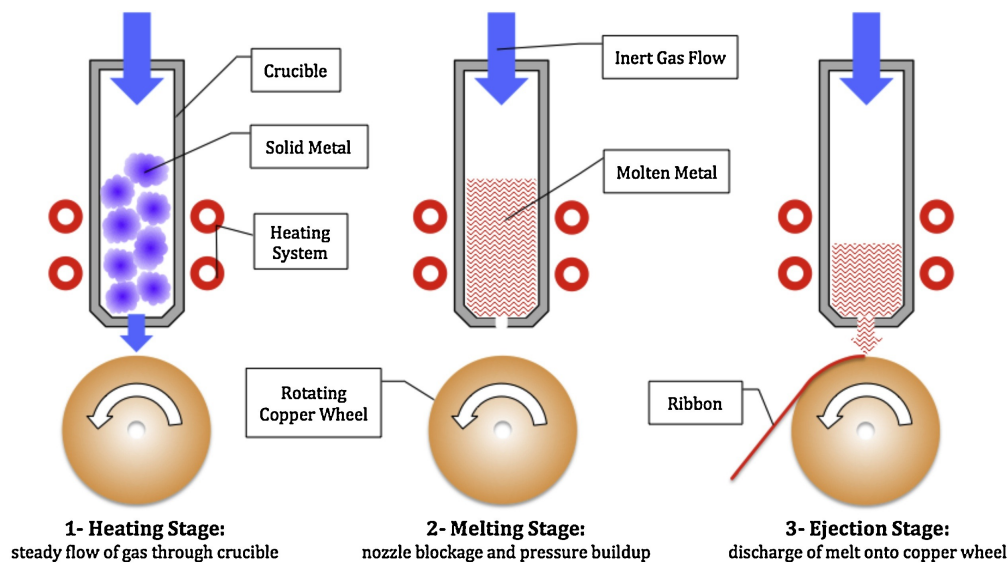


Figure 2.2: Diagram of the melt spinning process. Alloys are rapidly quenched in the ejection stage. [9]

, using a target with nominal composition of equiatomic FeCoNiCuMn. Sputtering is a physical vapor deposition process in which ionized noble gases, typically argon, are used to bombard a solid target, causing the ejection of atoms from the target. These atoms are sublimated and move towards a silicon substrate where they are deposited. Sputter deposition is a useful process for creating thin films with a thickness estimated by the sputtering rate of the target atoms. Every atom has a different sputtering rate due to the different energy required to sublimate each atomic species. These sputtering rates differ for atoms from elemental targets versus targets of multiple atoms due to the interactions between the atoms in the alloy targets, so it can be difficult to predict the final composition of the sputtered thin film based on elemental sputtering rates. The pressure inside the chamber during deposition also affects the sputtering rate and is a variable that must be considered.

A full assessment of the compositional, structural and magnetic differences between these thin films and their bulk counterparts can be found in Appendix A.2.

2.1.3 Compositional Analysis

Inductively coupled plasma (ICP) atomic emission spectroscopy (AES) was used to determine the composition of bulk alloys in powder form. ICP analysis requires ionizing the sample with plasma; these ions are then passed into a mass spectrometer which separates ions by their charge to mass ratio to determine elemental species. The sensitivity of ICP-AES is 0.1%, and the full set of ICP data taken for alloys in FeCoNiCuMn can be found in Appendix A.1.

The thin film samples of my alloys were analyzed for accurate compositional data using x-ray photoelectron spectroscopy (XPS), which measures the number and energy of electrons escaping the sample as it is excited with a beam of x-rays. The full compositional results can be found in Appendix A.2. With the help of collaborators at NASA Glenn, we analyzed three 20nm thin films using XPS; one film was sputtered in a 10 mTorr Ar environment. Two films were sputtered in a 5 mTorr Ar environment, and both were analyzed to see the variation between sputtering sessions under identical settings. The calculated compositions from the XPS analysis are listed in Table A.2.

2.2 Structural Characterization

2.2.1 X-Ray Diffraction

XRD measurements are typically taken by focusing a beam of mono-dispersive x-rays on a sample and measuring the diffracted x-rays at varied angles (Fig. 2.3). Bragg's law relates the wavelength of incoming photons (λ) to the planar spacing of a sample (d) and the angle at which these photons will be diffracted from these planes (θ) such that they constructively interfere with one another:

$$2d\sin(\theta) = \lambda \tag{2.1}$$

The diffracted peaks present will indicate the sample's crystal structure, and the indexed peaks can be used to calculate the lattice spacing. [115] Every plane of atoms in the sample can diffract x-rays, but the presence of certain atoms can prevent x-rays from being diffracted. For FCC crystals, we can calculate the scattering conditions which will allow for diffraction from the geometry of the crystal containing N atoms at positions notated as R_j for N total positions, and the geometry of the incident and scattered x-rays in reciprocal space (inverse to real space). The incident beam vector and scattered beam vector, k_o and k_s respectively, both have the same amplitude, $\frac{2\pi}{\lambda}$. Q , the scattering vector in reciprocal space, is the difference between these two vectors:

$$Q = |k_s| - |k_o| = 4\pi \frac{\sin(\theta)}{\lambda} \quad (2.2)$$

The wavefunction of the scattered wave will be the sum of the waves from all N atoms in the crystal:

$$F_{hkl} = \sum_{j=1\dots N} f_j e^{-iQ \cdot R_j} = \sum_{j=1\dots N} f_j e^{-2\pi i(hx_j + ky_j + lz_j)} \quad (2.3)$$

where f_j is the atomic form factor for atom j, Q is represented as the direction of the vector normal to a plane (hkl), and the atomic positions R are represented by their lattice positions in 3D space (for example, an atom in the middle of a BCC lattice would have $R=1/2,1/2,1/2$). To calculate the structure factor for a specific lattice, we must identify the sites and coordinates of each atom. FCC lattices have N=4 atoms in one cell; at the origin, (0,0,0), and on each of the three faces closet to the origin: (1/2,1/2,0), (1/2,0,1/2), and (0,1/2,1/2). Substituting these positions into Equation 2.3 results in:

$$F_{hkl} = f \left(1 + e^{-i\pi(h+k)} + e^{-i\pi(k+l)} + e^{-i\pi(h+l)} \right) \quad (2.4)$$

Thus the intensity of peaks in FCC diffraction patterns will be $4f$ for planes for which h,k, and l are all even or all odd, but will be 0 when this is not true. As a result, the lowest

peak in an FCC pattern is of the (111) plane.

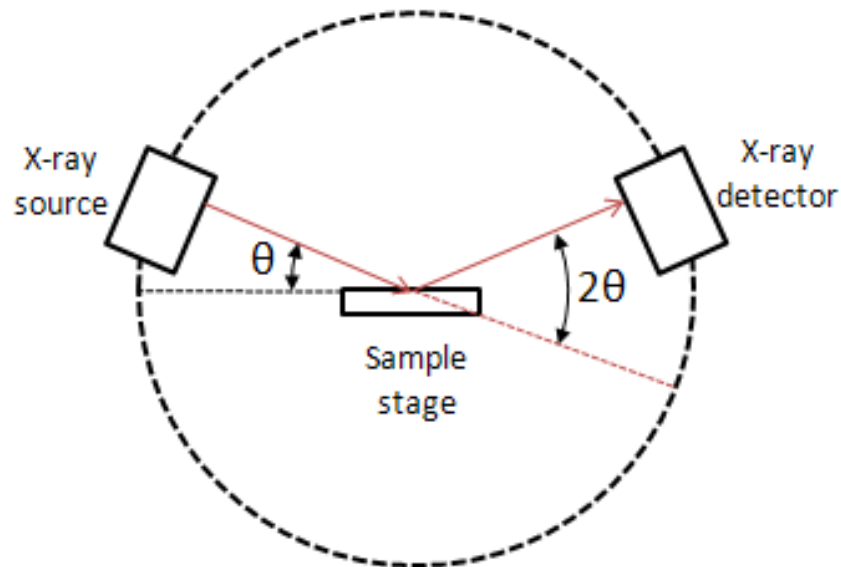


Figure 2.3: Diagram of the experimental setup of x-ray diffraction, demonstrating the frame of reference for the angle of diffraction. [10].

X-ray diffraction can also be performed by using a broad spectrum of radiation (called “white radiation”) and a fixed angle to fulfill the requirements of Bragg’s law—then, each diffraction peak is defined by its diffraction energy instead of the angle of the incoming beam. This type of spectrum is known as energy dispersive XRD, and these types of measurements are often performed using synchrotron radiation. I performed my data collection at Argonne National Lab’s Advanced Photon Source, which allowed us to probe a sample with an energy range of 10 keV–60keV. The advantage of these measurements is that these spectra can be acquired in seconds, and the intensity of the peaks is often larger, which allows weaker peaks to become more well-resolved. As the data taken through energy dispersive XRD will be in terms of energy instead of diffraction angle, the data is plotted as intensity versus the scattering vector, Q (equation 2.2).

Because Q is defined by both θ and λ ($\lambda = \frac{hc}{E}$), it is the same value regardless of the collection energy and angles, and is useful for direct comparison of spectra. Conversion to Q

is also the easiest way to convert data from one type of spectrum to the other. Regardless of whether data is collected from angle dispersive or energy dispersive, we expect to see some amount of broadening of the peaks caused by both instrumental and sample factors. For an infinitely long, single crystal (one grain that is all oriented in the same direction) measured with a source which produces only one monochromatic x-ray, the diffracted peaks would be infinitely thin. Broadening is an indication that multiple energies close to the “ideal” energy are still being constructively diffracted, which points to imperfections in the system or the sample. Instrumental factors that cause broadening include finite size of the incident beam of x-rays, finite size of parameters such as the diffraction slits modifying the beam, the small spread of energies produced by the x-ray source, and misalignment of the sample with respect to the x-ray source. Sample factors which cause broadening of the peak include small grain sizes, lattice distortion caused by strain in the sample, and inhomogeneous compositions throughout the sample. [116]

2.2.2 Scanning Electron Microscopy and Electron Dispersive Spectroscopy

Scanning electron microscopy uses a focused beam of electrons to take images of samples at much higher resolution than is possible with optical spectroscopy. This is due to the fact that the wavelength of an electron can be roughly a thousand times smaller than a photon, depending on the energy of the photon and the accelerating voltage of the electron. The electron beam is rastered over a rectangular area on the sample, and the number of electrons measured by a detector gives an intensity for each point which translates into a greyscale image. There are two types of electrons which can be detected; secondary electrons are the electrons emitted after an atom is excited by an electron from the beam, whereas backscattered electrons are electrons from the beam which bounce off the sample without being absorbed. The type of electron measured depends on what information we want from the sample.

Energy dispersive spectroscopy (EDS) is a technique often implemented within an SEM in which a sample is stimulated with a beam of electrons, and electrons in the atoms are excited to higher energy levels. As they relax back to their lower level, they emit an x-ray of characteristic energy. These x-rays can be measured for specific points across a sample to obtain a compositional mapping for an individual point, a line across the sample, or an area of the sample. EDS is an incredibly useful tool for diagnosing phase segregation and contamination in samples, but typically is only accurate compositionally within a few percent. More precise compositional information requires the techniques discussed in section 2.1.3.

2.2.3 Differential Scanning Calorimetry

Differential scanning calorimetry is a characterization technique which measures the heat flow required to heat a sample as well as the heat required to heat a well characterized reference sample. The difference between these measurements gives us a heat flow curve which can be used to calculate heat capacity of the sample. There should be a small peak in the heat flow during magnetic transitions because these transitions are non-disruptive and typically cause a small change in properties of the material. Heat flow curves will show a large peak for disruptive phase transformations like crystallization or a crystal-structure change. Positively changing peaks indicate an endothermic change (as more heat is being put into the material at that temperature) and negatively changing peaks indicate an exothermic change.

2.3 Magnetic Characterization

2.3.1 Vibrating Sample Magnetometry

A vibrating sample magnetometer (VSM) measures the change in magnetic flux through a magnetic sample as it is vibrated perpendicular to an applied magnetic field. The VSM

used for these measurements was a Quantum Design Model P525. The temperature range of the PPMS is 2K to 1000K.

There are several ways to calculate or approximate the Curie temperature of a material from the magnetization versus temperature curves obtained with a VSM. The first is by identifying the inflection point of the magnetization curve by plotting the derivative of the $M(T)$ data, and then extending the curve along this slope until it reaches 0. The actual magnetization data will never reach zero due to the fact that a magnetic field must be applied to measure the magnetization, so raw magnetization data will have a “tail” that trails off to 0 at higher temperatures. Another way to find T_c is to fit the data to the Arrott-Noakes equation of state:

$$M^{1/\beta} = A(T - T_c) + B\left(\frac{H}{M}\right)^{1/\gamma} \quad (2.5)$$

This equation combines several asymptotic components of magnetic behavior in a linear way. The parameters A , B , $1/\gamma$ and $1/\beta$ are optimized for best fit to the experimental data, and values of T_c are varied. For most magnetic materials, the value of $1/\gamma$ is around 0.75, and the value of $1/\beta$ is 2.5. Plots of $M^{2.5}$ vs $\left(\frac{H}{M}\right)^{0.75}$ for a range of temperatures, T , then produces a series of parallel straight lines. The line which goes to 0 at $M=0$ will correspond to T_c since that is when the y-intercept term, $A(T-T_c)$, will be 0. (Fig. 2.4) [11,117] The Arrott-Noakes equation of state is often used to scale magnetocaloric data for the magnetic entropy change in the ferromagnetic to paramagnetic phase transition for a variety of materials onto a single master curve [118]. The master curve functional form is developed from the Arrott-Noakes equation of state and plots the magnetic entropy change, ΔS by its maximum value and plot with respect to a reduced temperature, θ measured with respect to reference temperatures,

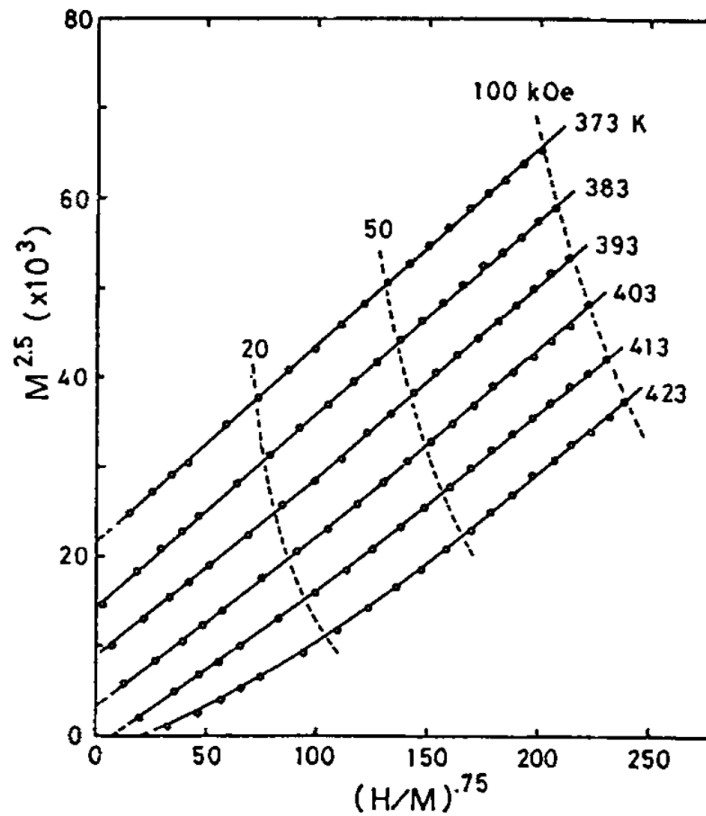


Figure 2.4: Arrott Noakes plot for an $\text{Fe}_{75}\text{Pt}_{25}$ alloy with T_c between 403K and 413K. [11]

T_{r1} and T_{r2} above and below the Curie temperature T_c such that:

$$\theta = \begin{cases} \frac{T-T_c}{T_{r1}-T_c}, & T \leq T_c \\ \frac{T-T_c}{T_{r2}-T_c}, & T > T_c \end{cases} \quad (2.6)$$

More complicated fitting is possible using Landau formalism, particularly for analysis of magnetic asymmetry in systems with distributed exchange. [84, 119] However, for basic determination of T_c , my data is almost always fit by extending the slope from the inflection point in the data, which is determined by calculating the derivative of the curve (Fig. 2.5). For magnetocaloric materials, the inflection point in the data corresponds to the peak of the magnetic entropy curve because the curve is proportional to the slope of $M(T)$ —therefore, I

often report T_{peak} instead of T_c for simplicity.

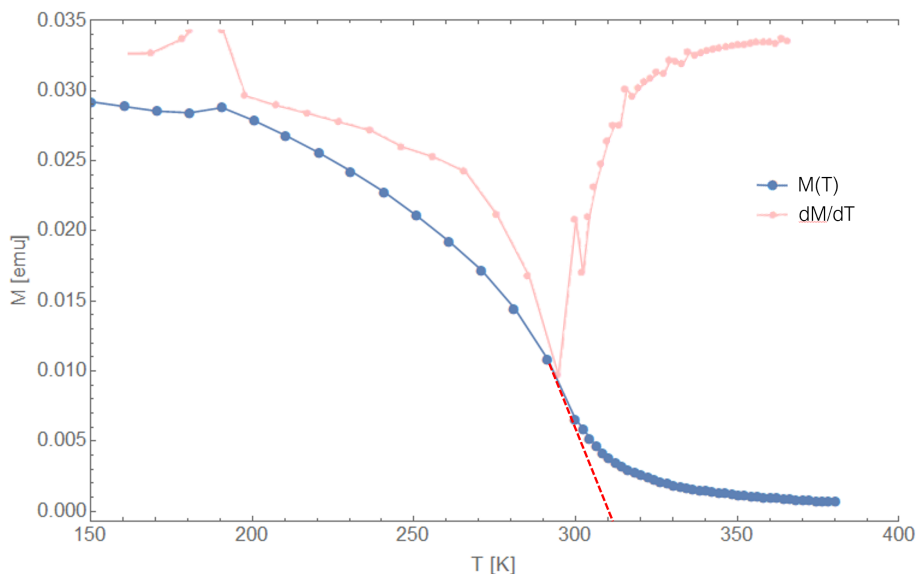


Figure 2.5: A magnetization versus temperature curve with the derivative curve, dM/dT overlaid to show the calculated inflection point. The slope at the inflection point is extended down until it intersects with the x axis in order to calculate T_c .

2.3.2 Mössbauer Spectroscopy

Atomic nuclei experience energy level transitions upon the absorption or emission of a gamma ray, and these transition energies are influenced by the atom's compositional, electronic, and magnetic environment. These shifts in the energy levels are known as hyperfine interactions and are incredibly small compared to the recoil energy an atom experiences when probed with spectra of gamma rays, making it impossible to observe these energy transitions with resonance fluorescence. However, recoilless emission and absorption of gamma rays, known now as the Mössbauer effect, was discovered in 1957 and is possible when the absorbing nucleus is contained within a solid, unreactive matrix [120]. This containment increases the effective mass of the nucleus, decreasing recoil greatly, and recoil is eliminated entirely if the energy of the gamma ray is too low to cause phonon transmission through the sample. In a recoilless event, a nucleus that absorbs a gamma ray of a certain energy will

then emit a gamma ray of the same energy (Fig. 2.6).

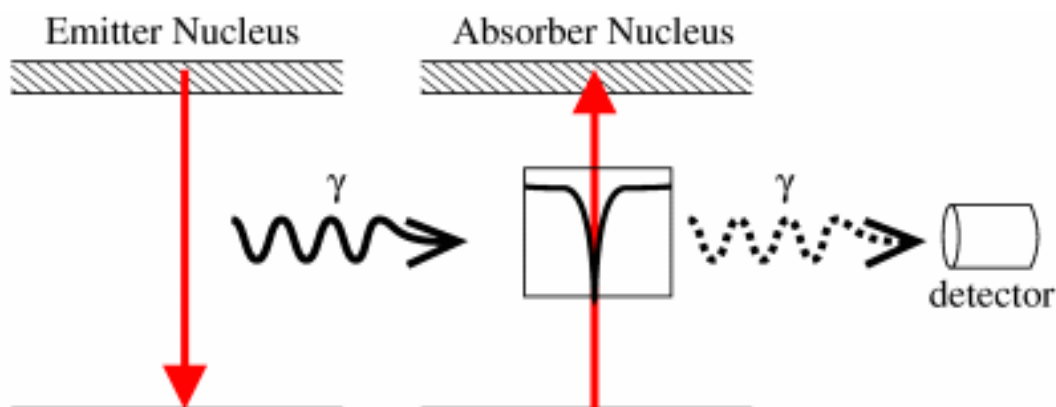


Figure 2.6: Experimental setup of Mössbauer spectroscopy measurements. If the emitter and absorber nuclei are identical, the transmission spectrum will be a simple peak, as it appears above. [12]

Therefore, in order to study a sample, the emitting nuclei of the source must be the same as the absorbing nuclei—for identical nuclei (in identical environments) this transmission will always occur. For an absorber nucleus in a different environment, however, the emitted gamma ray must be altered as well. This is done using the Doppler effect; the emitting source is moved forward or backwards at specific speeds reported in units of mm/s, and because the change in energy is so small, the transmission spectra are typically reported in terms of intensity of transmission versus source velocity for simplicity. [12,121] It is important to note that this technique investigates the environment surrounding one specific atomic species.

There are three primary environmental factors that will influence the energy levels of the absorber nuclei: isomer shift, quadrupole splitting, and Zeeman splitting. The isomer shift (chemical shift) corresponds to the electric monopole interaction between the nuclear charge distribution and the potential generated by the electronic charge distribution penetrating the nucleus. As a result of this interaction, the nuclear energy level will be shifted by a very small amount relative to the emission source (Fig. 2.7), which is different for each nuclear state. The isomer shift can be readily computed from a Mössbauer spectrum as the distance of the resonance line from zero Doppler velocity. Quadrupole splitting occurs due

to the presence of an electric field, and it results in the splitting of the central peak (known as a singlet) into two peaks, a doublet; it is also seen as a measure of the asymmetry of the magnetic contributions due to Zeeman splitting. Zeeman splitting is the splitting in energy levels due to the presence of magnetic dipoles (Fig. 2.7) and the magnetic hyperfine interaction between the magnetic dipole moment of the absorber nucleus and the magnetic hyperfine field surrounding it results in six peaks, a sextet (Fig. 2.8 shows an ideal example of this). The transmitted Mössbauer spectrum is then a superposition of singlets, doublets and sextets which need to be deconvoluted to obtain the Mössbauer parameters corresponding to the hyperfine interactions present in the sample [122]. The fitting of Mössbauer spectra is incredibly complex and requires the use of computational software which can optimize several variables for the best fit of the superposition of the isomer shift, quadrupole splitting, and Zeeman splitting. The theoretical peak shape is a Lorentzian fit, and any deviation from a perfect fit for each peak is an indication of imperfections in the sample, or improper fitting through the software due to constraints in the system (such as defining the isomer shift to be a physically impossible value). Multicomponent systems are especially challenging to fit properly as there are multiple magnetic interactions in the system, so the magnetic behavior will not lead to a single sextet in the spectrum, but several overlapping sextets which must be fit properly to calculate the strength of the field between the Fe^{57} atoms and each of its neighbors.

The hyperfine field surrounding the absorber nucleus can be thought of as the effective magnetic field of the sample acting at the location of the nucleus. When the hyperfine parameters fluctuate from one site to another, they give rise to hyperfine magnetic field distributions, which are obtained through the optimal fitting of the spacing and intensity of every individual set of peaks caused by Zeeman splitting in the Mössbauer spectrum [123]. The average hyperfine field gives us a measure of the strength of the average magnetic strength of atoms surrounding the absorber atoms in an alloy, which in a disordered solid solution should give a good estimate of the overall magnetic response of the alloy given that

each species of atom will sit in a similar environment. The presence and absence of these hyperfine fields distinguishes ferromagnetic and paramagnetic phases.

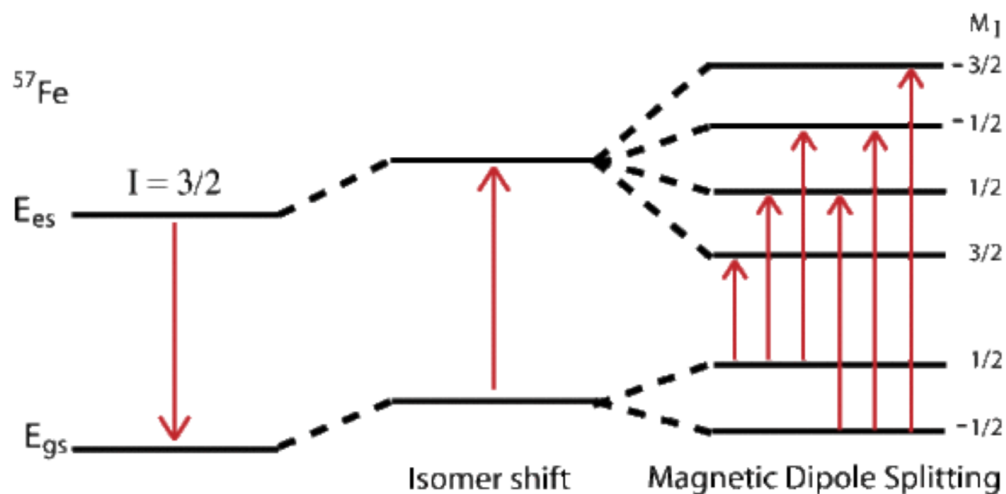


Figure 2.7: Electronic energy levels experiencing Zeeman splitting due to magnetic dipoles (right). [13]

The Mössbauer spectra obtained for my alloys were taken using a ^{57}Co gamma ray source embedded in a Rh matrix. This emitter nucleus is used to probe ^{57}Fe atoms because of its gamma ray energies, so all spectra and hyperfine field distributions are explorations of the local environment surrounding ^{57}Fe atoms in my alloys. The concentration of the ^{57}Fe isotope in naturally occurring iron is only around 2%, so in a sample containing around 20% Fe, the gamma rays are only probing around 0.4% of the atoms in the alloy.

2.3.3 Magneto-Optical Kerr Effect

MOKE imaging uses polarized light to probe a magnetic sample; a ray of polarized light is directed at the sample at an angle, and the polarization is rotated upon reflection after it interacts with the magnetic domains in the sample. The reflected polarized light is measured with a photovoltaic diode. Because the light is reflected, the domains can only be imaged if the sample is close to atomically smooth. The thin film version of my high entropy alloys were used for these measurements, after structural and magnetic measurements confirmed

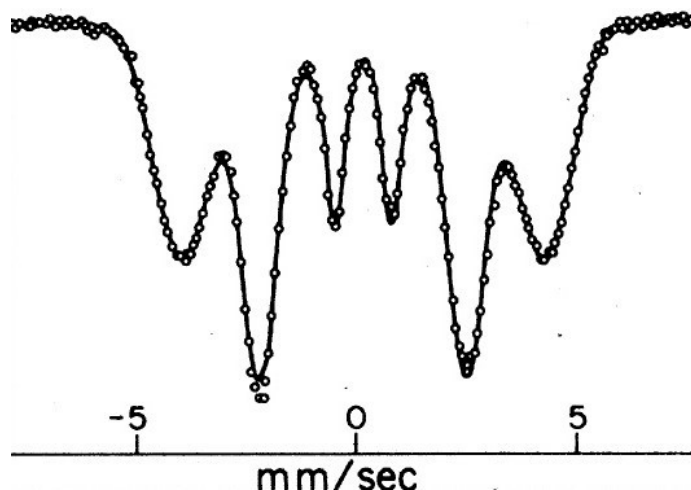


Figure 2.8: Example Mössbauer spectra for gamma rays after passing through $\text{Fe}_{80}\text{B}_{20}$. All six peaks due to Zeeman splitting are clearly defined. [14]

they were similar enough to the bulk for fair comparison of results.

The system used for any MOKE measurements allowed for low temperature measurements down to 10K as the sample is kept in a cryostat environment, and also allowed for measurements with applied fields up to 0.8T.

2.4 Applied Pressure Experiments

2.4.1 High Pressure XRD

High pressure x-ray diffraction was performed at Argonne National Lab's HPCAT 16-BM-B high pressure station. To apply hydrostatic pressure (evenly from all sides), I use specially designed boron nitride (BNi) Paris Edinburg ceramic cells (Fig. 2.9) which house small amounts of sample (<1mg). [124–126] The HPCAT 16-BM-B station uses a diamond anvil to compress the cell; the internal pressure of the sample is calculated using a well-characterized gold reference piece, which is also placed in the BNi cell. The x-rays can be focused on different parts of the cell so that it passes through the reference and sample separately. The diamond anvil cell can induce internal pressures up to 7 GPa.

Instead of the angle of acquisition being varied and the energy of the x-rays remaining

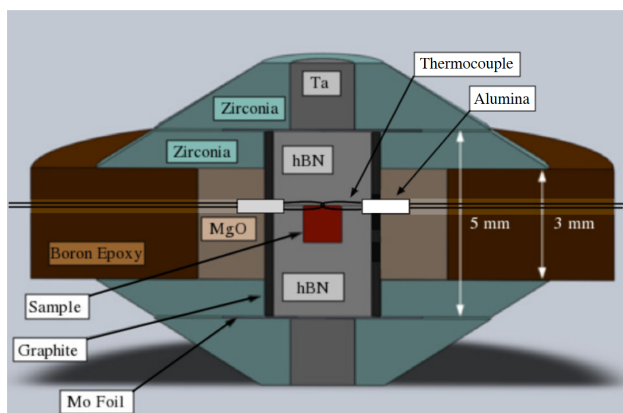


Figure 2.9: Diamond anvil cell designed to apply uniform pressure to samples

constant, the photon source provides a large range of x-ray energies known as “white radiation”, and the relative angle between the sample and x-ray source remains constant, which means that the detector is measuring the full spectrum of diffraction at any given time (Fig. 2.10). [127] Photons outside of the desired energy range are filtered out.

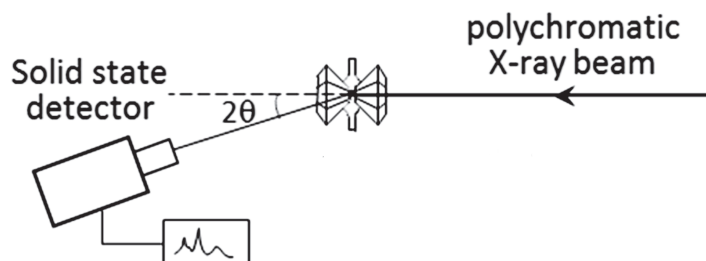


Figure 2.10: Beamline setup in which white radiation passes through the pressure cell into a solid state detector.

2.4.2 High Pressure Magnetometry

High pressure magnetometry measurements were taken at Lawrence Livermore National Lab in a superconducting quantum interference device (SQUID) magnetometer. The samples were placed inside a small Mcell 10 pressure cell (Fig. 2.11) which allows for uniform applied pressures up to 1 GPa. Pressure is applied with a Mpress Mk2 press and the desired

pressure is maintained by tightening the locknuts before loading the sample into the SQUID. A SQUID magnetometer measures magnetic moment using Josephson junctions, which is a superconducting tunnel junction which has a small current traveling through it. The magnetic flux from an external magnetic field from a magnetic sample will produce an additional current traveling through the loop to cancel the flux. This allows for the measurement of incredibly small magnetic fields, and is more sensitive than vibrating sample magnetometers.

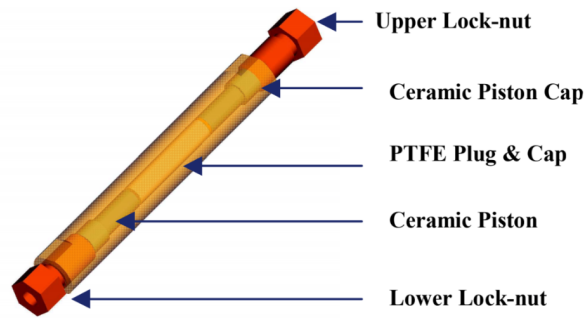


Figure 2.11: Mcell 10 pressure cell, which houses the sample in the TPF E plug and is mounted in a SQUID system. [15]

Chapter 3

Developing Magnetocaloric HEAs in the FeCoNiCuX System

3.1 Basis of Alloy Development and Curie Temperature Engineering

To ensure my initial attempt at developing a magnetocaloric high entropy alloy was reasonably broad and meticulous in its theoretical grounding, I began this study by synthesizing a large range of HEAs with one variable element. Based on the increase of entropy calculated from equation 1.21 and the literature on previous HEAs of interest, I decided to develop HEAs containing a minimum of five elements. I first developed a four element starting composition which maximized the configurational entropy while also keeping the saturation magnetization of the alloy high. The periodic table restricts us magnetically to three ferromagnetic elements with high T_c , so the first three components are iron, cobalt, and nickel. Pure iron has the highest magnetization, but combining the three elements in equal atomic amounts increases configurational entropy of the system considerably while maintaining a fairly large magnetization, and results in a distribution of ferromagnetic exchanges interactions in the system: Fe-Fe, Co-Co, Ni-Ni, Fe-Co, Fe-Ni, and Co-Ni.

However, the T_c of the three component alloy FeCoNi is still much higher than the desired room temperature range. Several groups have looked at four component high entropy alloys containing iron, nickel and cobalt [92], but the most well documented and best suited for magnetocaloric applications, FeCoNiCr, has been shown to have some phase instability, meaning that evidence of phase segregation has been found. This is significant as phase segregation would degrade the magnetic properties of the original alloy over time. [88]

This led us to chose a different fourth element, copper, to the FeCoNi basis, which increases the configurational entropy of the system by 26% ($S=\ln(3)$ to $S=\ln(4)$). Copper was chosen as it is weakly diamagnetic, which means it is repelled by magnetic fields and does not contribute a magnetic moment or exchange energy to the system. However, it does exhibit a small amount of RKKY coupling, which is the interaction between nuclear spins of neighboring atoms and conduction electrons in atoms. Conduction electrons are the non-localized electrons which make up the electron cloud in transition metals—this creates a correlation energy between the two nuclei. Compared with the ferromagnetic components, however, copper is not greatly influenced by surrounding magnetic moments [128]. The atomic size of copper is also close to the atomic radii of iron, cobalt, and nickel, which means it is more likely to form a solid solution with them than a much larger element. Copper does not af-

Composition	T_c (Exp)
FeCoNiCu	> 1000K
FeCoNiCuMo	580K
FeCoNiCuPt	930K
FeCoNiCuV	160K
FeCoNiCuGa	800K
FeCoNiCuAg	1000K
FeCoNiCuMn	405K
FeCoNiCuGaV	120K
FeCoNiCuVPt	667K
FeCoNiCuGaPt	625K
FeCoNiCuGaVPt	109K

Table 3.1: T_c of several 5+ component HEAs.

fect the strength of the pairwise ferromagnetic interactions already present but does dilute them by filling sites that would have held a magnetic element, decreasing the number of

magnetic nearest neighbors and leading to a greater percentage of weaker second and third neighbor interactions, which means the value of T_c as well as the saturation magnetization are lowered. However, $T_c > 1000\text{K}$ for equiatomic FeCoNiCu, so a single diluent is not enough to achieve a room temperature T_c . At this point it should be noted that all of these elements have an FCC primary phase or allotrope at room temperature (a phase which is not necessarily the dominant phase at that temperature, but can still be formed under the right conditions), so it is not unreasonable or surprising that these magnetic alloys form an FCC phase given that they are all similar in size and are able to close pack. From here, the higher configurational entropy that comes with a fifth element has to work against the effects of different atomic sizes, electronegativity, and other issues which cause segregation in alloys according to the Hume Rothery rules.

Several transition metals were added as fifth, sixth, and sometimes seventh elements to this base system in equiatomic amounts to observe the effect of each on the magnetic and structural properties of the system. The preliminary analysis of this broad selection of alloys was solely focused on T_c for each alloy to observe the difference from FeCoNiCu, and Table 3.1 lists these results. All six and seven element alloys were created for the purpose of observing how two elemental additions that produced five element alloys with T_c very far above or below room temperature would behave when combined. None of these alloys yielding promising results as the addition of extra elements diluted the magnetization and did not result in any alloys with T_c close enough to room temperature for further consideration, but some are included to demonstrate the result of different elemental combinations. For example, Pt and V were combined due to the fact that Pt as a fifth element did not lower T_c significantly, but V lowered T_c to well below room temperature. However, the combination of the two led to an alloy with T_c still significantly above room temperature despite a large decrease in magnetization due to V. It should also be noted that at this point, the crystal structure of each alloy in Table 3.1 was not measured, so it is possible that some of these alloys did not form a single phase HEA.

From the group of five component alloys, four were selected for further study of the structural and magnetic properties to determine fitness for magnetocaloric applications: 1) FeCoNiCu**Ag**, 2) FeCoNiCu**Mn** 3), FeCoNiCu**Pt**, and 4) FeCoNiCu**Mo**. These four were chosen because each addition had different characteristics that greatly affect the magnetic properties of an alloy.

1) FeCoNiCuAg:

Silver is a diamagnetic metal, and thus its main contribution to the FeCoNiCu system is dilution, similar to the role of Cu. Through RKKY interactions, it does exhibit slight contact polarization in alloys which could contribute to the magnetization [129].

2) FeCoNiCuMn:

Manganese is antiferromagnetic at nearest neighbor distances, so close Mn-Mn bonds will contribute antiferromagnetic interactions and thus negative exchange to the system, lowering T_c in the material. The pairwise interactions Mn-Ni, Mn-Co, and Mn-Fe are antiferromagnetic at these distances as well, further contributing to the lowering of T_c . [130] The increased number of exchange interactions broadens the exchange distribution, which should increase refrigeration capacity by increasing the FWHM of the entropy curve, but the negative exchange will lower the overall magnetization, decreasing ΔS_{peak} .

3) FeCoNiCuPt:

Platinum is a Stoner enhanced metal, which means that on its own it is paramagnetic, but its weak paramagnetic magnetic moment is bolstered by electronic proximity to ferromagnetic elements like Fe, Co, and Ni. This gives rise to additional Fe-Pt, Co-Pt, and Ni-Pt exchange interactions which should broaden the ΔS curve and increase refrigeration capacity as well. [131–134]. As these are positive interactions, T_c will be lowered only by dilution.

4) FeCoNiCuMo:

Molybdenum contributes virtual bound states to the alloy due to its valence difference with the magnetic constituents of the alloys. This causes free electrons to become bound to specific energy bands, thus removing them from contributing to the magnetic spin of the

system. This can lower T_c , but will simultaneously lower the magnetization [135–137].

3.2 Structural Characterization

High entropy alloys are a solid solution of randomly distributed atoms on a lattice. As discussed in section 1.4.1, the unique properties of HEAs rely on this random distribution, as atomic ordering and clustering tend to negatively affect the properties and weaken the alloy. To ensure my alloys were structurally single phase, I first performed x-ray diffraction (XRD) on each sample, which gave us the crystal structure and lattice parameters of each. The resulting XRD peaks for all four alloys are shown in figure 3.1. Each of the four alloys in question exhibits a face centered cubic (FCC) crystal structure, and all alloys have similar lattice parameters. Each peak in Fig. 3.1 was indexed for the corresponding set of FCC planes. This served to identify the obvious presence of a second phase in the alloys, which would produce extraneous peaks if they had a different crystal structure or lattice parameter. There is evidence of a small amount of a second crystal structure in FeCoNiCuAg evidenced by the few small peaks indexed as BCC peaks in Fig. 3.1, indicating a BCC structure. However, a lack of these extra peaks does not confirm that the distribution of the atoms within these alloys is entirely random and single phase. Clustering of atomic species with similar lattice parameters and the same crystal structure of the bulk would not be evident through diffraction.

I then performed electron dispersive spectroscopy (EDS) in a scanning electron microscope (SEM) to map the compositions of each alloy over a selected area. Fig. 3.2 shows the combined compositional maps for each alloy on the micron scale. FeCoNiCuMn (3.2a) and FeCoNiCuPt (3.2c) both appear homogeneous at this scale. However, there is clear inhomogeneity in the FeCoNiCuAg (3.2b) and FeCoNiCuMo (3.2d) samples. The individual elemental maps reveal that in FeCoNiCuAg, there is formation of Ag clusters and Cu deficits. Though the Fe elemental map is too weak to confirm directly, pure Fe has a BCC structure

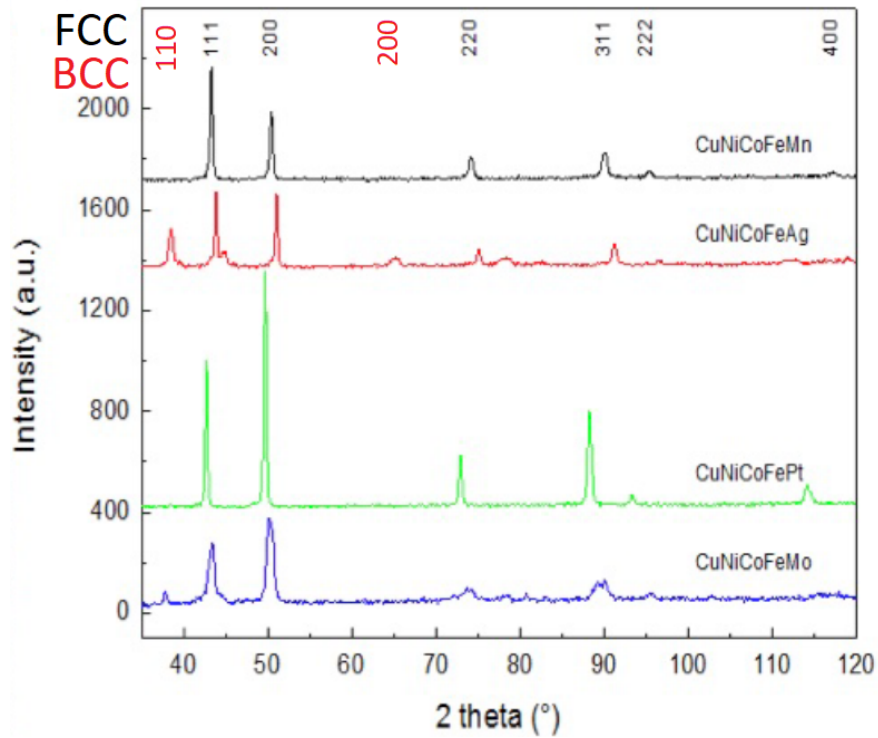


Figure 3.1: X-ray diffraction scans for each five-component HEA. FCC peaks are labelled at the top in black, and some extraneous BCC peaks labelled in red can be seen in the red spectrum of FeCoNiCuAg.

with peaks consistent with the extra peaks present in red in Fig. 3.1, which confirms some Fe segregation as well. Elemental composition maps for FeCoNiCuMo reveal that the evident clusters are Cu rich, which is unsurprising as Cu is immiscible in Mo [17] (see Appendix B, Fig. B.1 for binary phase diagram). These clusters do not result in extra peaks in the XRD scans because the crystal structure and lattice parameter of pure Cu is very close to FeCoNiCuMo (3.615 \AA). These results show that neither Ag nor Mo additions result in a single phase solid solution, which is significant because we are relying on the high entropy aspect of the alloys to broaden the magnetic response.

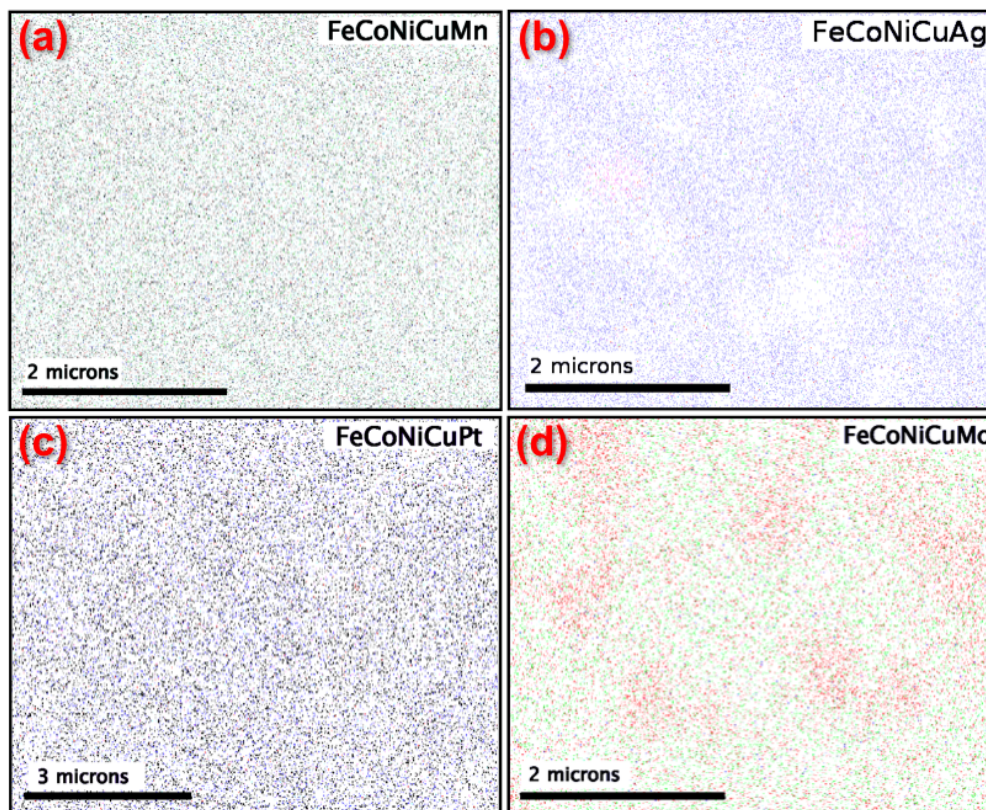


Figure 3.2: EDS composition maps of (a) FeCoNiCuMn, (b) FeCoNiCuAg, (c) FeCoNiCuPt, and (d) FeCoNiCuMo. Clustering is evident in (b) and (d).

3.3 Magnetic Characterization

I measured the Curie temperature, saturation magnetization, and refrigeration capacity using a Physical Properties Measurement System (PPMS) with a Vibrating Sample Magnetometer (VSM) head attached (Fig. 3.3). Saturation magnetization is determined by applying a large field (typically above 2T) to a sample and measuring the magnetization as it approaches 0K. T_c can be approximated as the inflection point in a magnetization versus temperature curve taken at low field, or calculated more exactly using the Arrott Noakes equation of state to fit the curve. The values of T_c I report in Tab. 3.1 and 4.2 are the approximations based on the inflection point method because the inflection point coincides with the peak of the ΔS curves for each alloy. The refrigeration capacity requires measuring several magnetization versus field curves at temperatures ranging above and below T_c . These

values for the four alloys of interest are compiled in Tab. 3.2.

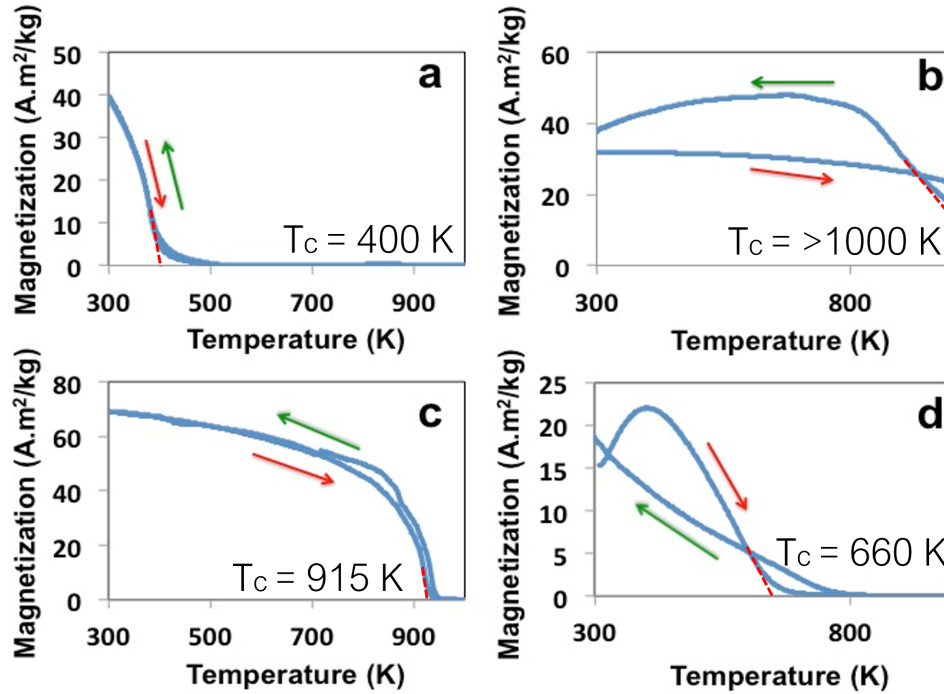


Figure 3.3: Magnetization versus temperature for (a) FeCoNiCuMn, (b) FeCoNiCuAg, (c) FeCoNiCuPt, and (d) FeCoNiCuMo. Dotted red lines indicate the inflection point slope used to calculate T_c . Green arrows indicate cooling curve and red arrows indicate heating curves.

Because platinum is a Stoner enhanced metal, additional exchange interactions were contributed to FeCoNiCuPt, resulting in the largest saturation magnetization and an increased refrigeration capacity. However, T_c is still 630K above room temperature, making this alloy unfit for commercial refrigeration applications. The additional virtual bound states caused by the presence of molybdenum lowered T_c of FeCoNiCuMo by several hundred Kelvin, but also dramatically reduced the saturation magnetization and refrigeration capacity. Diamagnetic silver did not lower T_c enough for accurate magnetic characterization, but did lower the magnetization through dilution, thus also lowering the refrigeration capacity. The addition of manganese lowered T_c to 400K, only 100K above room temperature, while still maintaining a substantial magnetic moment and refrigeration capacity. The refrigeration capacity of FeCoNiCuMn is similar to that of the FeCoNiCuPt despite FeCoNiCuPt having

a magnetic saturation (and thus ΔS value) almost twice as large as that of the FeCoNiCuMn because the presence of Mn increases the number of exchange interactions in the alloy which widens FWHM of the ΔS curve. I also note that the magnetization versus temperature curves show abnormal hysteresis upon cooling versus heating for the Ag and Mo alloys which is related to the phase segregation seen in EDS analysis; different magnetic phases which are affected by temperature form upon heating, changing the T_c and shape of the curve upon cooling. This further emphasizes the importance of a stable single phase high entropy alloy for magnetocaloric applications, as the magnetocaloric properties must remain constant for several heating and cooling cycles.

Composition	T_c (K)	M_s (emu/g)	RC (J/kg) at $H_{max}=0.55T$	Homogeneous?
FeCoNiCuMo	660	18	4	No
FeCoNiCuPt	930	70	18	Yes
FeCoNiCuAg	> 1000	36	–	No
FeCoNiCuMn	405	40	16	Yes

Table 3.2: T_c , M_s , RC, and assessment of homogeneity for HEAs.

3.4 Summary

I assessed the properties of several alloys with the structure FeCoNiCuX where X was one of several transition metals. I studied in detail the different effects of these various elements on both the structural and magnetic properties of the alloys. FeCoNiCuAg did not have a reduced T_c because Ag is diamagnetic, and the larger atomic radius of Ag caused chemical separation in the alloy. FeCoNiCuMo also suffered chemical separation, and the attractive reduction in T_c was outweighed by the much greater reduction in the magnetization and refrigeration capacity. Neither alloys are single phase solid solutions due to the existence of a second phase, which decreases the efficacy of the desired effect from high entropy mixing. FeCoNiCuPt was compositionally homogeneous and had a large magnetization and

refrigeration capacity, but T_c remained too high for these alloys to be commercially viable. Finally, FeCoNiCuMn benefited from the antiferromagnetic interactions from manganese, which lowered T_c close to room temperature while maintaining homogeneous structure and a competitive refrigeration capacity. FeCoNiCuMn and FeCoNiCuPt both exhibit promising magnetic properties as well as structural homogeneity, but the former was chosen for further study because of its more attractive T_c and due to the price of Pt, which is more expensive, and therefore less viable, for commercial production of bulk alloys. [138, 139]. I can also posit that the Mn contribution was the most successful in creating a suitable HEA partially because it follows the Hume-Rothery rules for solid solution formation given that it is very similar in atomic size, electron valency, and electronegativity to Fe, Ni, Co, and Cu.

Chapter 4

Analysis of Compositional Variation In FeCoNiCuMn System

4.1 Psuedo-Binary Compositional Variations in System

In chapter 3 I found that the addition of antiferromagnetic manganese, which contributes negative exchange interactions to the system, dramatically lowers T_c of the alloy from over 1000K to 400K. To further tune T_c of alloys in the FeCoNiCuMn alloy system to achieve values even closer to room temperature, I studied several alloys where the Mn content was increased in equal amounts to another element being decreased. This variation is called a psuedo-binary as it mimics the changing compositions in a binary alloy system by changing only two elements at a time, but contains other elements whose compositions are remaining constant. For a five component alloy in which Mn is always varied, there are then four possible pseudo-binary alloy systems: $\text{FeCoNiCu}_{1-x}\text{Mn}_{1+x}$, $\text{FeCoNi}_{1-x}\text{CuMn}_{1+x}$, $\text{FeCo}_{1-x}\text{NiCuMn}_{1+x}$ and $\text{Fe}_{1-x}\text{CoNiCuMn}_{1+x}$. The two element variation ensured that the changes observed could be attributed to the compositional decrease of one specific atom, as all other elemental compositions are kept constant at 20%. Table 4.1 shows calculations for

# of Equiatomic Components	$ S_{config} $ J/mol K	$ S_{2-equi} - S_{config} $ J/mol K	% Increase from S_{2-equi}
2	0.693	0	0%
3	1.099	0.405	58%
4	1.386	0.693	100%
5	1.6094	0.916	132%
Pseudo-Binary Composition	S_{config}	$ S_{5-equi} - S_{config} $	% Decrease from S_{5-equi}
19.5/20.5	1.6093	1.25E-4	0.007%
19/21	1.6089	5E-4	0.03%
18.5/21.5	1.6083	1.13E-3	0.07%
18/22	1.6074	2E-3	0.124%
17.5/22.5	1.6063	3.1E-3	0.195%
17/23	1.6049	4.5E-3	0.28%

Table 4.1: Top: Configurational entropy calculated for equiatomic alloys with different number of components. Right columns show the difference between the calculation and a binary alloys (S_{2-equi}), and the % S increases. Bottom: Configurational entropy calculated for small psuedo-binary departures from equiatomic in 5-component alloys. Right columns show the net difference from equiatomic, and the % S decreases.

the configurational entropy (equation 1.21) of 2, 3, 4, and 5 component equiatomic alloys, as well as the entropy for 5 component alloys in which two atoms are varied in a psuedo-binary, to show how much entropy is lost as I explore these small compositional departures to tune T_c . The configurational entropy increases by 132% as I move from a binary equiatomic alloy to a 5-component equiatomic alloy, but the configurational entropy decreases less than half a percent as I depart from equiatomic by a few atomic percent in a psuedo-binary. Thus, I concluded it was unlikely that the small compositional changes required to tune T_c would result in instability of the single phase solid solution.

This proved to be accurate for my alloy system; each variation achieved a T_c at room temperature with very small compositional changes ($x < 0.1$), and all alloys were confirmed to be single-phase, FCC solid solutions using x-ray diffraction. Fig. 4.1 shows the relationship between T_c and atomic percentage of Mn for each pseudo-binary alloy system, and it's

important to note that these relationships are not entirely linear, making it difficult to predict what T_c a more complex elemental variation will yield. The refrigeration capacity of each system was measured as well, and demonstrate a similar trend (Fig. 4.2). Of these, the Cu-Mn and Fe-Mn pseudo-binaries produced alloys with the largest RC values at a room temperature T_c . For the Cu-varied system, $\text{FeCoNiCu}_{0.95}\text{Mn}_{1.05}$ was the composition found to have a room temperature magnetic transition, with a refrigeration capacity of 13.4 J/kg at $H_{max}=0.55$ T (this scales up to 36 J/kg at $H_{max}=1.5$ T). The Fe-varied alloy with a room temperature T_c was $\text{Fe}_{0.975}\text{CoNiCuMn}_{1.025}$ and a refrigeration capacity of 14.01 J/kg at 0.55 T (which scales to 37.4 J/kg at 1.5 T).

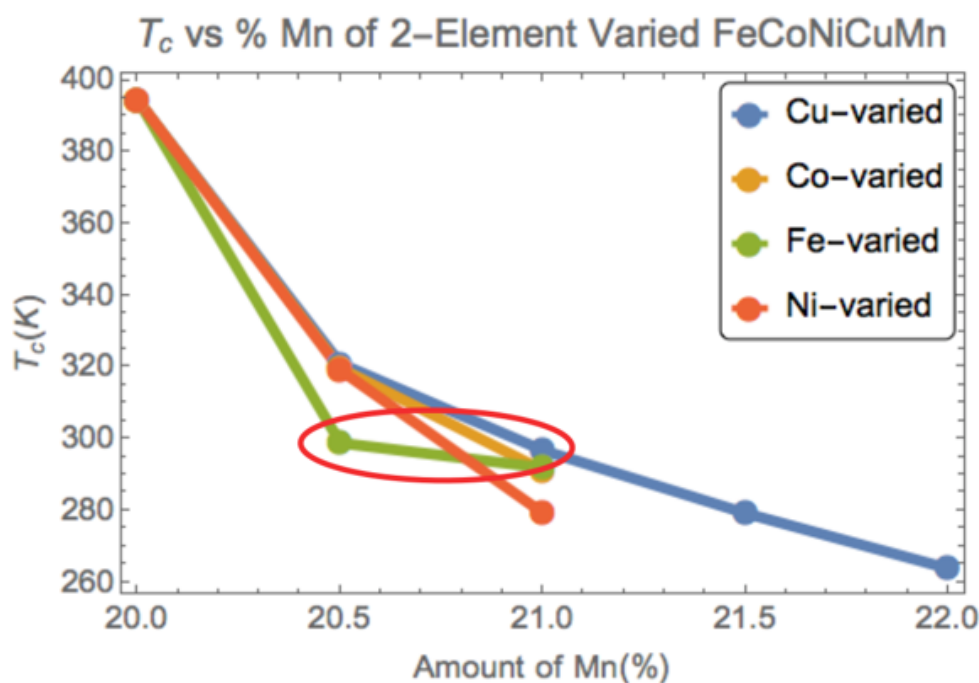


Figure 4.1: T_c values for alloys in the FeCoNiCuMn psuedo-binary systems, plotted with respect to their atomic Mn content. The two most promising alloys are circled in red.

Though the Fe-Mn varied alloy system yields a slightly larger refrigeration capacity at room temperature, it is important to remember that the magnetic transition temperature shifts upward in larger applied fields. Thus, for applications that allow for larger applied fields, I consider alloys in my system with T_c slightly below room temperature. The Cu-Mn

pseudo-binary appears to be more attractive when considering these lower T_c alloys; the decrease in Cu required to balance the increase in Mn maintains the ferromagnetic pairwise contributions in the alloy as constant; therefore the overall magnetization and refrigeration capacity decrease more slowly with higher Mn content than in the Fe-Mn pseudo-binary; we see in the move from $\text{Fe}_{0.975}\text{CoNiCuMn}_{1.025}$ to $\text{Fe}_{0.95}\text{CoNiCuMn}_{1.05}$ that there is a large reduction in RC even with a relatively small reduction in T_c .

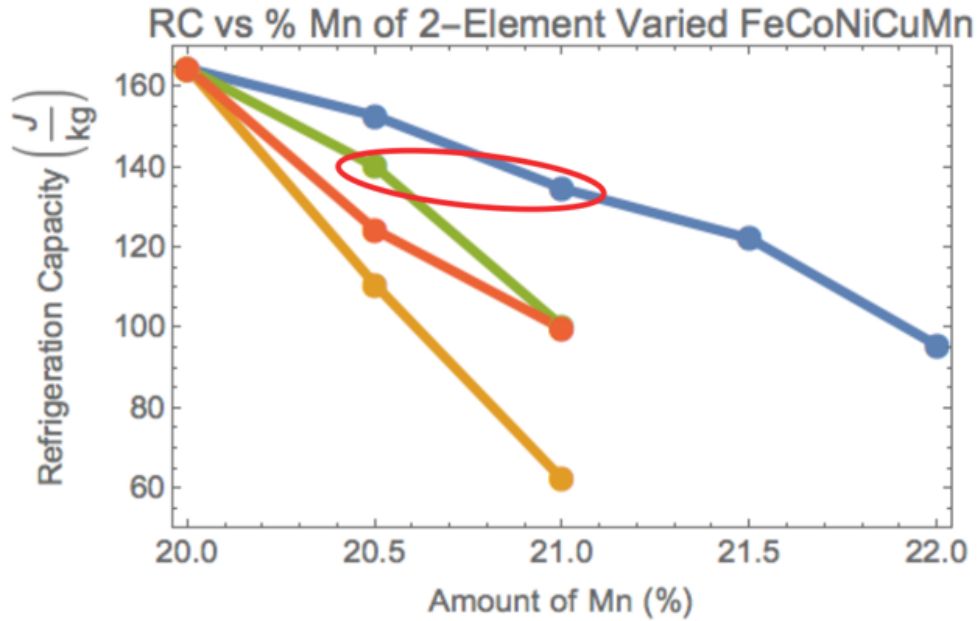


Figure 4.2: RC values for alloys in the FeCoNiCuMn psuedo-binary systems, plotted with respect to their atomic Mn content. The two most promising alloys are circled in red.

I performed thermal analysis of these alloys using differential scanning calorimetry (DSC). At the transition temperatures, these DSC measurements yield heat capacities around 250 J/kgK. For $\text{FeCoNiCu}_{0.95}\text{Mn}_{1.05}$, eq. 1.19 then yields $\Delta T_{ad}=0.8$ K for a single demagnetization cycle from a max field of 1.5 T. At $H_{max}=1$ T, this drops to $\Delta T_{ad}=0.5$ K. We can compare these values with experimental values obtained for two well-studied magnetocaloric materials, $\text{La}(\text{Fe},\text{Co},\text{Si})_{13}$ ($\Delta T_{ad}= 2.4$ K) and $\text{La}_{0.67}\text{Ca}_{0.26}\text{Sr}_{0.07}\text{Mn}_{1.04}\text{O}_3$ ($\Delta T_{ad}=1.0$ K), in an active magnetic regenerator refrigerator, to gauge our alloys effectiveness as an MCE material [52].

For comparison of their utility in commercial magnetocaloric applications, a summary of some of the most promising magnetocaloric materials can be found in Table 4.2. The alloys in Table 4.2 are restricted to those with a higher order transition, which means they have smaller ΔS_{peak} values and broader FWHMs, as they offer the most meaningful comparison. It is clear from the ΔT_{ad} calculations as well as from the comparisons in Table 4.2 that while my alloys are on par with the other high entropy alloy (FeCoNiCrPd_{0.059}), its magnetocaloric response is not large enough to make a compelling argument for commercialization, but there are several more specialized applications which merit exploring the properties of the FeCoNiCuMn system in more depth.

Composition	H_{max} (T)	T_{peak} (K)	$ \Delta S_{max} $ (J/kgK)	RC_{FWHM} at H_{max} (J/kg)	Reference
FeCoNiCu _{0.95} Mn _{1.05}	5	320	2.2	140	My work [140]
Fe _{0.975} CoNiCuMn _{1.025}	5	318	2.3	134	My work [140]
FeCoNiCrPd _{0.059}	5	150	0.8	170	[91]
Pr ₂ Fe ₁₇	1.5	305	0.75	~ 35	[141, 142]
Gd ₅ Ge ₂ Si ₂	2	240		45	[143]
Fe ₇₅ Nb ₁₀ B ₁₅	1.5	250	0.6	115	[144]
Mn _{1.1} Fe _{0.9} Pe _{0.78} Ge _{0.22}	5	280		400	[145]
Fe ₈₈ Zr ₇ B ₄ Cu ₁	1.5	300	1.3	166	[146]
Fe ₇₀ Ni ₃₀	1.5	363	0.6	158	[42]
(Fe ₇₀ Ni ₃₀) ₉₆ Mo ₄	5	300	1.67	432	[82]

Table 4.2: Summary of properties of several promising magnetocaloric materials; my current alloys of focus are listed first.

Our magnetic and thermal analysis has given us general insight into the behavior of this alloy system and its utility for magnetocaloric applications. However, the number of magnetic interactions in these alloys, both ferromagnetic and antiferromagnetic, added to the already complex requirements for high entropy alloy formation, makes these alloys incredibly interesting from a more fundamental perspective. I then turned to Mössbauer spectroscopy to observe the relationship between the pairwise exchange interactions present in these alloys and the average magnetic behavior.

4.2 Magnetic Analysis through Mössbauer Spectroscopy

4.2.1 Qualitative Observation of Exchange Interactions

Mössbauer spectroscopy (explained more fully in section 2.3.2) was performed on 11 samples in the FeCoNiCuMn alloy system in collaboration with Monica Sorescu at Duquesne University in order to explore the magnetic interactions in these samples more fully: equiatomic, two alloys in each pseudobinary extending to 21 at% Mn, and two additional alloys in the Cu-Mn pseudobinary extending to 22 at% Mn. The Mössbauer spectra, when fit for Zeeman splitting, reveal a complex hyperfine field distribution containing several discrete peaks. The peaks are not coherent enough to fit individually, which prohibits us from quantifying the amount in each distribution or assigning specific field values to each peak. However, their presence alone is enough for some qualitative discussion of these alloys. The four pseudobinaries probed, Cu-Mn, Ni-Mn, Co-Mn, and Fe-Mn, produce a range of alloys with T_c spanning from 400K to below room temperature, and the average hyperfine field of these alloys decreased with T_c (Tab. 4.2.2), but it is still non-zero for the compositions with T_c lower than room temperature. This is evidence that my materials undergo a broad, higher order magnetic transition, as a first order transition would result in a sharp drop in the average hyperfine field.

Each hyperfine field distribution exhibits a handful of peaks at several values of field strength, some which are obscured and appear as shoulders on other peaks. Several identifiable peaks are indicated by red arrows in Fig. 4.3. Though I cannot definitively quantify the number of peaks in each distribution, it is worth pointing out that the number of peaks and shoulders identified for each alloy is around six; there are six ferromagnetic pairwise interactions in each alloy (Fe-Fe, Co-Co, Ni-Ni, Fe-Co, Fe-Ni, and Co-Ni). These peaks show evidence of these individual pairwise interactions, demonstrating that the magnetic behavior is an average over these interactions and is responsible for the broad magnetocaloric response in these alloys. Past work by Kimball et al. has shown that Mössbauer spectroscopy can

Composition	% Mn	T_{peak} (K)	Average Hyperfine Field (T)	Isomer Shift (mm/s)
FeCoNiCuMn	20	395	12.68	-0.051
FeCoNiCu _{0.975} Mn _{1.025}	20.5	321	6.68	-0.056
FeCoNiCu _{0.95} Mn _{1.05}	21	297	5.07	-0.086
FeCoNiCu _{0.925} Mn _{1.075}	21.5	279	3.73	-0.09
FeCoNiCu _{0.9} Mn _{1.1}	22	264	3.41	-0.08
FeCoNi _{0.975} CuMn _{1.025}	20.5	319	7.08	-0.025
FeCoNi _{0.95} CuMn _{1.05}	21	280	4.45	-0.094
FeCo _{0.975} NiCuMn _{1.025}	20.5	320	7.33	-0.037
FeCo _{0.95} NiCuMn _{1.05}	21	292	4.79	-0.09
Fe _{0.975} CoNiCuMn _{1.025}	20.5	299	6.24	-0.079
Fe _{0.95} CoNiCuMn _{1.05}	21	292	4.43	-0.09

Table 4.3: Mössbauer spectroscopy data for FeCoNiCuMn pseudo-binaries.

identify antiferromagnetic behavior in Fe-Mn alloys, even with spectra that do not have fully resolved six peaks due to Zeeman splitting. [123] The FeCoNiCuMn spectra collected are weak because they were obtained at room temperature, near T_c for these alloys, but spectra taken at a lower temperature would allow more resolved peaks, which could allow us to examine the antiferromagnetic interactions in these alloys as well.

4.2.2 Quantitative Analysis of Hyperfine Field Distributions

Though the hyperfine field distributions for the Mössbauer spectra are too weak to fit, we can use the corresponding average hyperfine fields to reveal the contributions from each atom to the changing values. Table 4.2.2 lists the average hyperfine fields in each alloy, which indicates the average strength of the exchange interactions between the atoms, alongside the transition temperature, T_{peak} (or T_c) for each alloy and the isomer shift (all raw spectra and hyperfine field distributions are included in Appendix C.1). Because the isomer shift is a measure of Coulomb interactions in the alloy, it should be larger as the density of the s-orbit electrons increase, or conversely as there is less d-electron screening of the s-orbitals. We see this reflected in the isomer shift values for these alloys, which increase with Mn content as Mn contains fewer d-orbital electrons than the other atoms present.

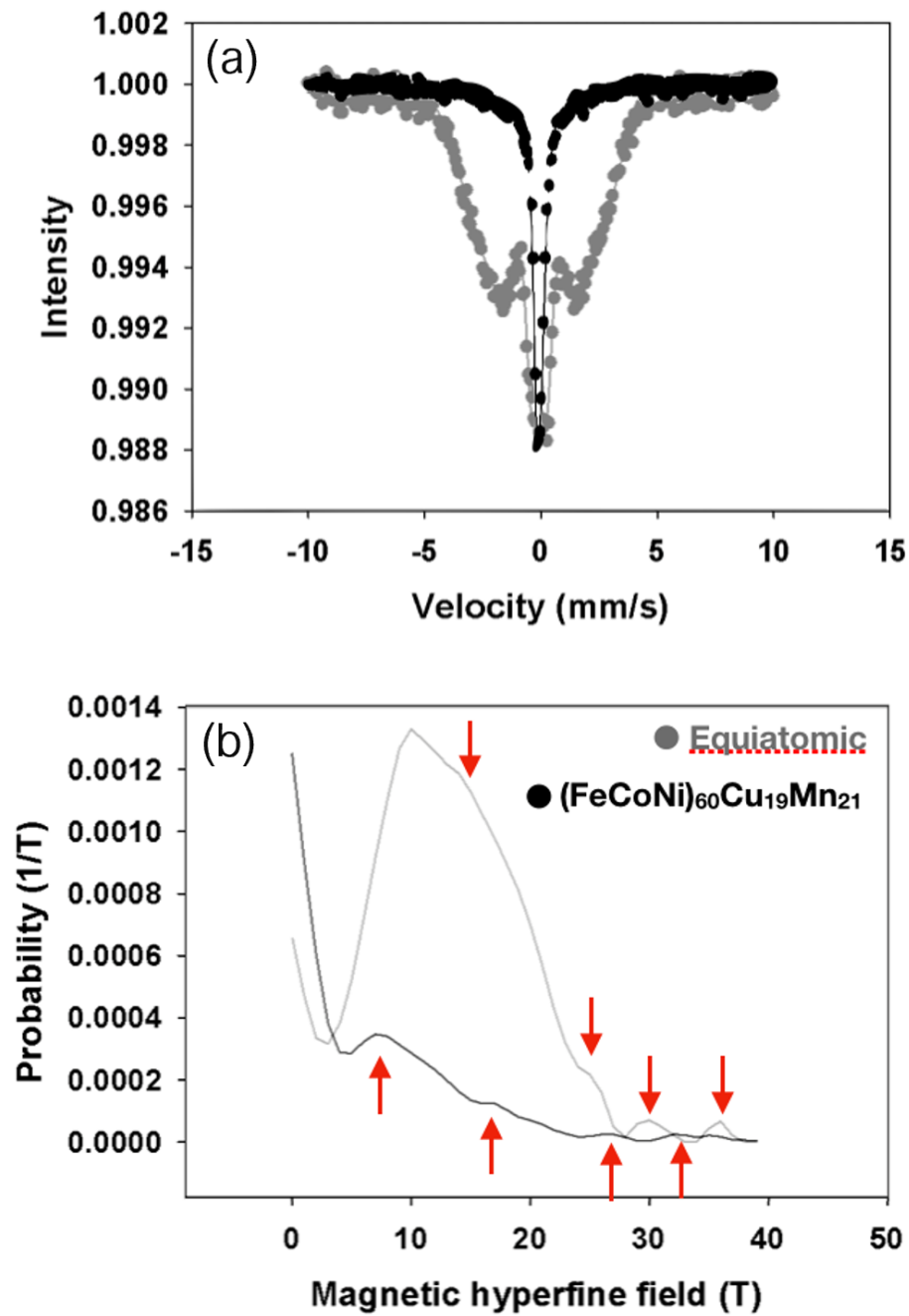


Figure 4.3: Top: Mössbauer spectra for two HEA alloys. Bottom: Corresponding HFDs, with discrete peaks and shoulders denoted with red arrows.

The average hyperfine fields decrease linearly with the T_{peak} values, a correlation strong enough that I can use it to gain further information about the system (Fig. 4.4). We can see at the low T region of the plot that the Cu-Mn pseudobinary begins to level off as it approaches lower T_c values, but the majority of the data lies on a line with a maximum $\langle HFD \rangle$ deviation of $\pm 0.35T$. Thus, a calculated or experimental value of the average hyperfine field can be used to estimate T_c of an alloy, and vice versa, within this range. This is also significant as it allows to assess the contributions from the individual atomic species in the system.

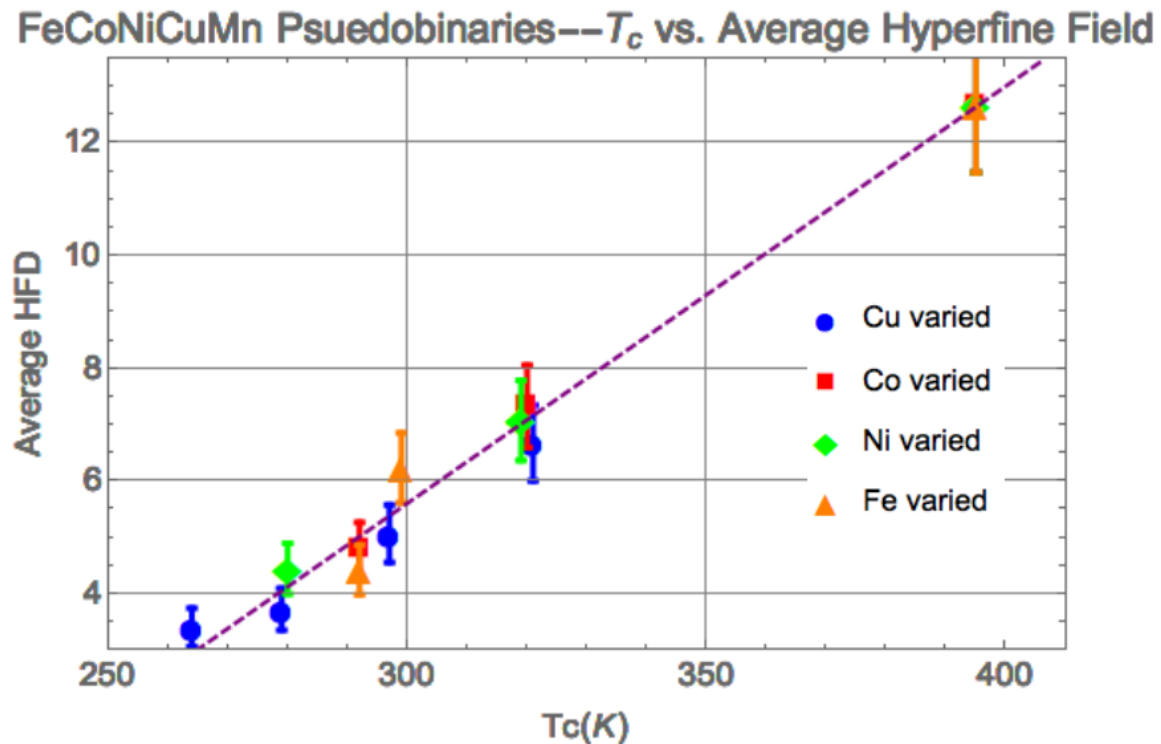


Figure 4.4: T_c of pseudo-binary alloys plotted against average hyperfine field, demonstrating that the relationship is composition-independent for small variational changes.

To calculate the contribution from each element to the average hyperfine field, I follow the model laid out in Brent Fultz' 1993 paper [147], which investigates the change in hyperfine fields experienced by Co atoms in BCC solid solutions as a function of the composition of the nearest and next nearest neighbors, also known as the addition perturbation model. The

model begins by defining the hyperfine field of the solid solution as the hyperfine field of pure Co, H_o , plus a perturbation, ΔH :

$$H = H_o + \Delta H \quad (4.1)$$

This perturbation can be broken into three terms:

$$\Delta H \approx n_1 \Delta H_1^x + n_2 \Delta H_2^x + \kappa c \quad (4.2)$$

where n_1 and n_2 refer to the number of nearest and next nearest neighbors, respectively, and ΔH_1^x and ΔH_2^x refer to the contributions from each set of neighbors. All further neighbors, whose contributions to the hyperfine field are relatively weak, are wrapped into the κc term, where κ is the average concentration dependence of the perturbations, and c is the concentration of solute atoms. Though this model is based around a single solute in a BCC lattice, it is easily extended to other systems, and has been used to explore many atomically ordered systems [30, 148–154]. However, there are several instances of this model being used to explore atomically disordered additions or entirely disordered systems as well, often in Fe-Ni binary alloys [155–161]. To model an FCC crystal, the neighbor terms are changed to $n_1=12$ and $n_2=6$. It's important to note that though there is a term for further neighbors, this consideration is less important for an FCC alloy, in which electrons are more localized to the atoms given the close packed structure, versus a BCC alloy. [162] In section 4.2.1, I provide qualitative evidence of local moment interactions in my alloys through the discrete peaks visible in the hyperfine field distribution. The H_o term is now defined as the average hyperfine field of the equiatomic FeCoNiCuMn alloy, and the ΔH contribution is broken into several solute terms:

$$\Delta H = \Delta H_{Ni} + \Delta H_{Fe} + \Delta H_{Mn} + \Delta H_{Cu} + \Delta H_{Co} \quad (4.3)$$

and it follows that the average contribution from all is a sum of the average of each:

$$\langle \Delta H \rangle = \langle \Delta H_{Ni} \rangle + \langle \Delta H_{Fe} \rangle + \langle \Delta H_{Mn} \rangle + \langle \Delta H_{Cu} \rangle + \langle \Delta H_{Co} \rangle \quad (4.4)$$

Because we cannot get accurate variance information from the hyperfine field distributions, we do not have enough information to distinguish between nearest and next nearest neighbor. This would require data from twice as many alloys in the FeCoNiCuMn HEA family. However, as long as my alloys are truly randomly distributed solid solutions, this is not as important a distinction for us to make (versus an ordered alloy in which site-specific information would be desirable). The terms in the ΔH expressions, then, can be lumped together into one new value, G_x , where G is the average of the near neighbor and next nearest neighbor influence:

$$\langle \Delta H \rangle = \sum_x c_x (12\Delta H_1^x + 6\Delta H_2^x) = \sum_x c_x G_x \quad x = \{Ni, Fe, Mn, Cu, Co\} \quad (4.5)$$

Thus the final expression for the perturbations due to the change in composition for my alloys simplifies to:

$$\langle \Delta H \rangle = c_{Fe} G_{Fe} + c_{Cu} G_{Cu} + c_{Mn} G_{Mn} + c_{Ni} G_{Ni} + c_{Co} G_{Co} \quad (4.6)$$

With enough different alloys, and accurate compositional data for each alloy (the full compositional data of these alloys is listed in Appendix A.1), the values of G_x for each atom can be calculated using the average hyperfine field values listed in Table 4.2.2. The resulting values of G_x are listed in Table 4.4. These values validate the assumptions I have made about each element's contribution the system based on their elemental properties. The largest positive contributions come from Co and Ni, which are ferromagnetic with large magnetic moments, and the larger moment and T_c of Co over Ni correlates to a larger contribution. Fe has a noticeably smaller contribution, and I suggest that this is due to the decreased atomic distance

between Fe atoms in these alloys. While BCC Fe is ferromagnetic, FCC Fe is antiferromagnetic, so it is possible that the closer packing in these alloys approaches the crossover point. Given that G is a reflection of the sum of both nearest and next nearest neighbor atoms, it is likely that the nearest neighbors of Fe are contributing antiferromagnetic exchange, but the next nearest neighbors are contributing ferromagnetic exchange, and the sum of the average of this results in a net positive exchange for Fe. This gives us further insight into the antiferromagnetic interactions in the alloy, which are lowering both the magnetization and T_c . Cu is not expected to change the hyperfine field drastically as it is diamagnetic, but the small amount of RKKY coupling Cu experiences does give it a slightly positive contribution. Finally, antiferromagnetic Mn causes a large, negative contribution to the average hyperfine field.

Element	$G_x \left(\frac{T}{\text{atom}\%} \right)$
Co	2.165
Fe	0.215
Ni	0.839
Cu	0.136
Mn	-3.058

Table 4.4: Contributions to average hyperfine field from each element.

I developed alloys in the FeCoNiCuMn system with more than two elements varied, allowing us to assess the validity of these results, as well as the limits of the linearity of the average hyperfine field versus T_c . The alloys $\text{Fe}_{19}\text{Co}_{20}\text{Ni}_{19}\text{Cu}_{19}\text{Mn}_{23}$ and $\text{Fe}_{19}\text{Co}_{20}\text{Ni}_{19}\text{Cu}_{20}\text{Mn}_{22}$ were estimated to have $T_c=248\text{K}$ and $T_c=294\text{K}$ from the calculated values, while the experimental values of T_c were found to be 225K and 319K . This demonstrates that the Fultz model can estimate T_c values within 25K for this system. At and above 24% Mn, there is a low temperature phase which arises which drastically affects the shape of the magnetization curves and suggests the presence of a second magnetic phase (discussed further in chapter 6), at which point we lose the linearity of the T_c vs HFD relationship.

This approach could also be used to characterize and make predictions in other similar systems (for example, a system with Cr replacing some Mn) provided that some data about

an alloy in the system, or the Mössbauer spectra, has been obtained, but I have not done further work to confirm this experimentally.

4.3 Summary

I present Mössbauer spectra obtained for four psuedo-binary alloy systems branching from equiatomic FeCoNiCuMn. The hyperfine field distributions calculated for these spectra have several distinct peaks which is evidence of the discrete exchange interactions between the magnetic components of the alloys, and I demonstrated a simple model for calculating the contributions of each atom to the average hyperfine field. I found that the values estimated T_c within 25K for two new alloys in the system.

Chapter 5

The Effects of Pressure on the FeCoNiCuMn System

5.1 High Pressure X-Ray Diffraction

Applied pressure has been shown to affect the stability of the crystal phase of a material, an effect observed in several materials, particularly multiple component alloys. [163–165] Because exchange interactions are highly sensitive to atomic distance, applying pressure large enough to compress the unit cell could also cause a shift in magnetic behavior and magnetic phase transition temperatures.

The first high pressure experiment run on an FeCoNiCuMn alloy was at Argonne National Lab on the Advanced Photon Source at the high pressure HP-CAT 16-BM-B station, and x-ray diffraction patterns were taken under various applied hydrostatic pressures. These patterns are obtained differently than the XRD patterns obtained in Carnegie Mellon's characterization facility; instead of the angle of acquisition being varied and the energy of the x-rays remaining constant, the photon source provides x-rays across the desired energy spectrum (photons outside of this range are filtered out) and the relative angle between the sample and x-ray source remains constant.

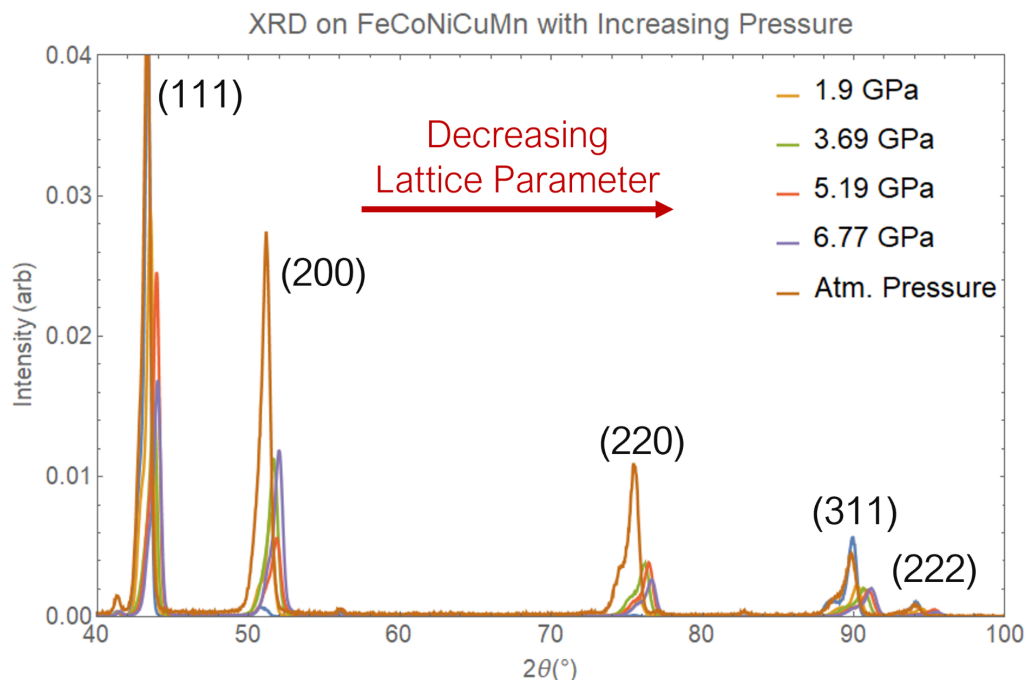


Figure 5.1: Diffraction peaks for FeCoNiCuMn with applied pressure. Shoulders present on all patterns (including atmospheric pressure) are due to copper clustering.

The diffraction peaks obtained at Argonne National Lab using the high pressure x-ray diffraction station (Fig. 5.1) did not reveal any destabilization of the lattice or formation of intermetallics. A shoulder present on all of the diffraction peaks, including on the patterns taken before any pressure was applied (ruling out pressure-induced lattice splitting), was determined to be due to be a small unincorporated clustering of copper, which was confirmed through analysis of the peaks using Rietveld refinement [166]. Given that copper is more likely to segregate than the other atoms in these alloys, this is not surprising. Small amounts of clustering like this would typically be lost in the noise of the spectrum among larger samples, but the geometry of the pressure cell allows for a very small amount of sample, meaning any compositional fluctuation present will be more noticeable. This is not a major cause for concern over the high entropy nature of my alloys as I have seen no other indications of phase separation through compositional mapping with EDS, nor are there any bumps in the magnetization curves or heat capacity curves suggesting segregation, but this does

indicate that meticulous incorporation of elements during the arc melting process is crucial for optimal homogeneous mixing in these alloys.

The change in lattice parameter, and thus unit cell volume, can be calculated from the location of the diffraction peaks with respect to applied pressure. We can then calculate the bulk modulus, defined as:

$$\text{bulk modulus} \equiv \frac{\Delta P}{-\Delta V/V} = -V \frac{dP}{dV} \quad (5.1)$$

The bulk modulus of FeCoNiCuMn is listed in Table 5.1 along with the bulk moduli of each elemental component, the average of these components, and other alloys for comparison. We can see that the bulk modulus of FeCoNiCuMn is greater than the average of each component, evidence of the “cocktail” effect often discussed to explain the properties of high entropy alloys. As HEAs have previously been studied for structural applications, this is not surprising, but this is significant in that most of the structural HEAs have a BCC crystal structure. These alloys then belong to a small group of FCC HEAs with advantageous strength properties that have been identified thus far. [167, 168] This increased

Element/Alloy	Bulk Modulus (GPa)
FeCoNiCuMn	175
Fe	119
Co	180
Ni	180
Cu	123
Mn	120
Elemental Average	144
Cast Brass	116
Stainless Steel	160

Table 5.1: Bulk modulus of FeCoNiCuMn compared with elemental components, and other common alloys.

bulk modulus is likely due in part to the added strain on the lattice caused by slightly different atomic sizes of each atom, which discourages diffusion or other movement of atoms.

For systems in which all of the contributing factors that lead to peak broadening can be clearly identified and quantified, the amount of strain from the atomic size differences could be calculated using a Williamson-Hall plot, in which peak broadening (β_{total}) is separated into two components, β_L for grain size broadening, and β_e for strain broadening. [169–171] However, the grain structure of these alloys is small (10nm subgrains in as-cast samples) and irregular, which creates too much variability in peak broadness to be able to gain meaningful values of strain from this type of analysis.

5.2 High Pressure Magnetization Measurements

I have also obtained magnetization versus temperature data for FeCoNiCu_{0.95}Mn_{1.05}, which has $T_c=305\text{K}$ for at atmospheric pressure in collaboration with Scott McCall at Lawrence Livermore National Lab. The samples were prepared by first being cooled to 5K in zero applied magnetic field from room temperature, and then the magnetization was measured from 5K to 350K, and then down to 5K again under the influence of a 20 Oe applied field in a SQUID magnetometer.

Under the conditions of zero field cooling, we can observe two magnetic transitions upon heating: one, the ferromagnetic to paramagnetic transition, T_c , and the second, a transition that appears to show a net magnetization near zero that transitions rapidly to the ferromagnetic phase, and is labelled T_n in Fig. 5.2. This transition is still not well understood, but it is discussed in more detail in Chapter 6 and is the focus of future work.

We can analyze the change in T_c with respect to pressure using the Ehrenfest equation, which is derived from the Gibbs free energy and is the higher order equivalent of the first order Clausius-Claperyon equation:

$$\frac{dP}{dT} = \frac{\Delta s}{\Delta v} \quad (5.2)$$

The Clausius-Claperyon equation correlates $\frac{dP}{dT}$ with the change in entropy and change in volume of the unit cell over a phase transition; as the unit cell does not experience a volume

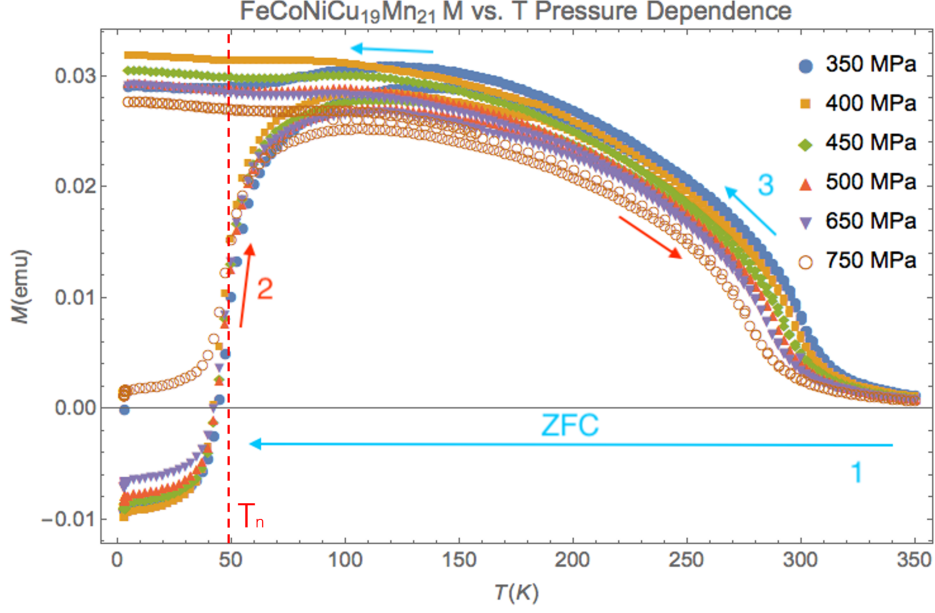


Figure 5.2: Plot of magnetization vs. temperature at several applied pressures. Each measurement follows the pattern: (1)ZFC to 5K, (2) 20Oe field heating to 350K, (3) 20Oe field cooling back to 5K.

change during higher order transitions, $\Delta V = 0$. We can derive the higher order Ehrenfest equation for a continuous phase transition by first recognizing that $\Delta S = 0$ for a higher order transition. [172,173] This can be broken into partial derivatives:

$$\Delta S = \left(\frac{\partial \Delta S}{\partial T}\right)dT + \left(\frac{\partial \Delta S}{\partial P}\right)dP = 0 \quad (5.3)$$

However, the term $\frac{\partial \Delta S}{\partial T}$ can be written in terms of the change in the heat capacity:

$$\frac{\partial \Delta S}{\partial T} = \frac{\Delta C_P}{T} \quad (5.4)$$

In the second term, we can rewrite the partial derivative using a Maxwell relation, and then substitute the value for the change in thermal expansion coefficient, α , which is a measure of how much a material's volume changes in response to temperature:

$$\frac{\partial \Delta S}{\partial T} = -\frac{\partial \Delta V}{\partial T} = -\Delta \alpha V_m dP \quad (5.5)$$

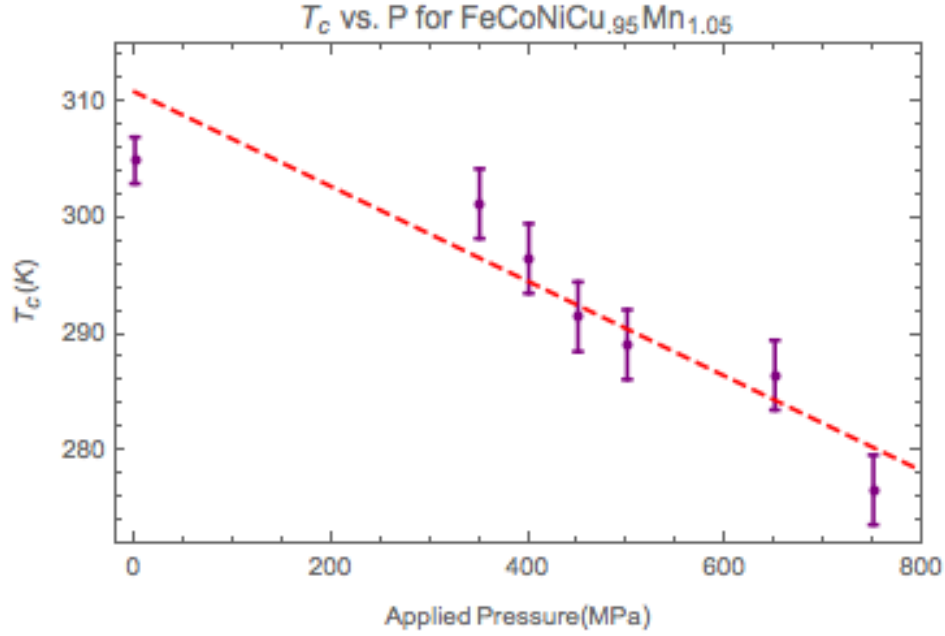


Figure 5.3: The relationship between applied pressure and measured T_c values, which is fairly linear.

Making these substitutes into equation 5.3 results in the equation:

$$\Delta S = 0 = \frac{\Delta C_P}{T} dT - \Delta \alpha V_m dP \quad (5.6)$$

When we simplify this equation to get $\frac{dT}{dP}$, we arrive at the Ehrenfest equation:

$$\frac{dT_c}{dP_o} = \frac{TV_m \Delta \alpha}{\Delta C_P} \quad (5.7)$$

where V_m is the volume of the magnetic phase, $\Delta \alpha$ is the change in the thermal expansion coefficient, and ΔC_p is the change in the heat capacity over the phase transition. The change in $\frac{dT_c}{dP} = -3.33 \text{K/kbar}$. A negative change in $\frac{dT_c}{dP}$, and thus a negative change in $\Delta \alpha$ is common in many magnetic systems, such as iron-nickel alloys and rare earth-iron alloys, and the values of each system's $\frac{dT_c}{dP}$ is roughly the same as the value calculated for FeCoNiCuMn. [174–176]

Though it is not the main focus of this work, many magnetocaloric materials are also studied for barocaloric properties—that is, a change in temperature with applied pressure. The value

of $\frac{dT_c}{dP}$ is not large enough to consider my alloys viable barocaloric materials.

Though the ΔS_M vs T curves and RC values were not calculated for each alloy, we can see from Fig. 5.2 that the magnetic saturation decreases slightly as applied pressure increases. A decrease in magnetization will lower ΔS , which lowers the refrigeration capacity, so it is possible to conclude that the application of pressure also decreases the magnitude of the magnetocaloric response of $\text{FeCoNiCu}_{0.95}\text{Mn}_{1.05}$, and The small barocaloric response of these alloys is not enough to compensate for this loss of magnetocaloric response. Despite this, the application of pressure is an important tool for understanding the underlying magnetic interactions in these alloys.

5.3 Analysis of Pressure Effects on D-Orbital Spatial Extent

In section 1.2.2, I gave an overview of the physics which led to the creation of the Bethe-Slater curve, which demonstrates the empirical relationship between magnetic exchange and atomic spacing normalized by d-orbital spatial extent for the transition metal elements which exhibit ferromagnetic or antiferromagnetic exchange.

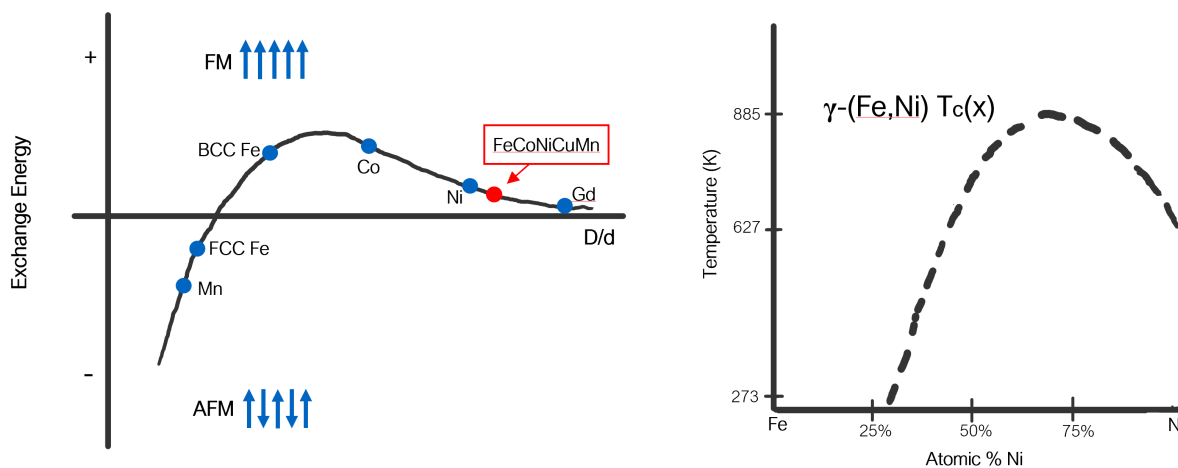


Figure 5.4: (a) Bethe Slater Curve, showing the empirical relationship between J_{ex} and D/d_{d3} . (b) T_c of the disordered FCC Fe-Ni phase. [16]

The Bethe-Slater curve is often used to highlight changes in exchange with changing atomic spacing, D , for example in Mn-Bi and alloys where increased Mn-Mn distance results in a switch from antiferromagnetic to ferromagnetic exchange [38–40]. However, consider the change of T_c of the (FCC) disorder γ -Fe-Ni phase with composition (Fig. 5.4b) [16,177]. Since FCC Fe and Ni have very similar atomic size and lattice constants, the systematic changes of T_c is not explained by atomic spacing alone. Both FCC Ni and FCC Fe fall directly on the Bethe-Slater curve, the latter on the antiferromagnetic region of the curve. Compositions in the binary alloys mimic the shape of the curve through the entirety of the range. I therefore consider a compositional dependence of J_{ex} arising from d-orbital contraction. The change in T_c for the Fe-Ni alloys depends on band filling causing d-orbital spatial extent contraction with increasing Ni concentration. Thus I consider atomic spacing, D , and d-orbital spatial extent, d , as distinct variables to assess changes in J_{ex} . Expanding the Bethe Slater curve as a sum of partial derivatives, for a composition variable, x :

$$\frac{\partial J(\frac{D}{d})}{\partial x} = \frac{\partial J}{\partial(\frac{D}{d})} \left(\frac{1}{d} \frac{\partial D}{\partial x} - \frac{D}{d^2} \frac{\partial d}{\partial x} \right) = \frac{\partial J}{\partial(\frac{D}{d})} \left(\frac{1}{d} \frac{\partial D}{\partial x} - \frac{D}{d} \frac{\partial \ln d}{\partial x} \right) \sim \frac{\partial J}{\partial(\frac{D}{d})} \left(- \frac{D}{d} \frac{\partial \ln d}{\partial x} \right) \quad (5.8)$$

The $\frac{\partial J}{\partial(\frac{D}{d})}$ term is from the slope of the Bethe-Slater curve itself, and the final derivative is dominated by the change in d-orbital spatial extent, $\frac{\partial \ln d}{\partial x}$. Given this evidence for the importance of d-orbital extent on assessing change in magnetic exchange, I can similarly assess the magnetic behavior of a system under applied pressure:

$$\frac{\partial J(\frac{D}{d})}{\partial P} = \frac{\partial J(\frac{D}{d})}{\partial(\frac{D}{d})} \frac{\partial(\frac{D}{d})}{\partial P} = \frac{\partial J}{\partial(\frac{D}{d})} \left(\frac{1}{d} \frac{\partial D}{\partial P} - \frac{D}{d^2} \frac{\partial d}{\partial P} \right) = \frac{\partial J}{\partial(\frac{D}{d})} \left(\frac{1}{d} \frac{\partial D}{\partial P} - \frac{D}{d} \frac{\partial \ln d}{\partial P} \right) \quad (5.9)$$

Note that the leading term again reflects the slope of the Bethe-Slater curve, which can be positive or negative depending on where on the curve we start. The term in parentheses can also be positive or negative depending on the relative importance of the pressure

dependence of the lattice constant (interatomic spacing) or the extent of the d-orbitals.

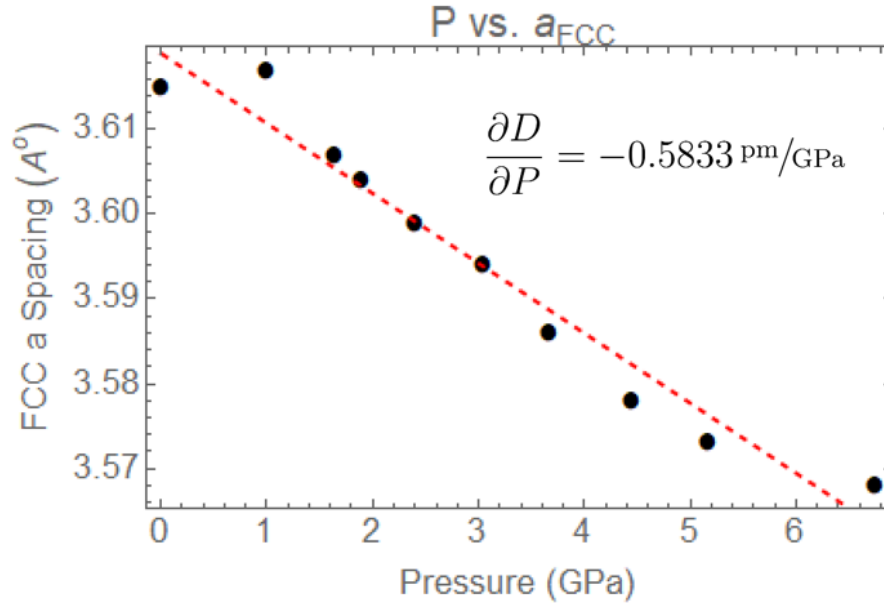


Figure 5.5: (a) P vs a (lattice spacing) for FeCoNiCuMn derived from high pressure XRD data. From this data I calculated the change in atomic spacing, $D = \frac{a}{\sqrt{2}}$.

The term $\frac{\partial J}{\partial \left(\frac{D}{a}\right)}$ is taken from the slope of the Bethe Slater curve, which we can parameterize based on expectation values of the radius of the d-orbitals. D and $\frac{\partial D}{\partial P}$ can be obtained from atmospheric and high pressure x-ray diffraction (XRD) data (Fig. 5.1) of FeCoNiCuMn. Peaks were indexed to an FCC structure and the lattice constants and d-spacings were determined using the Bragg equation. Fig. 5.5 illustrates the pressure dependence of the lattice spacing, a_{FCC} , derived from the parameters calculated from the XRD pattern. From this data I determined the change in atomic spacing ($\frac{D_{FCC}}{\sqrt{2}}$). The $\frac{\partial D}{\partial P}$ term in equation 5.9 is thus -0.583 pm/GPa.

Fig. 5.2 illustrates magnetization versus temperature curves for the FeCoNiCu_{0.95}Mn_{1.05} alloy under pressure. The data shows T_c for this alloy decreases with increasing applied pressure. T_c was estimated from inflection points on the magnetization curves, and calculated more precisely using an Arrott-Noakes equation of state [117] to fit to ensure an accurate value of the derivative, $\frac{\partial T_c}{\partial P}$, which is equal to -40.8 K/GPa. From the change in T_c with pressure (Fig. 5.3) we can estimate the value of $\frac{\partial J \left(\frac{D}{a}\right)}{\partial P}$ using mean field theory [178]:

$$J_{ex} = \frac{3k_b T_c}{2S(S+1)} \quad (5.10)$$

The mean field value of S for these alloys was estimated to be $S=1.5$ based on elemental values and comparison with similar alloys and their location on the Slater-Pauling curve. However, it should be noted that the fits are not particularly sensitive to variation of S with different S replicating the compositional trends with values of d scaled upwards. The calculations assume localized d -electrons. This is consistent with evidence for discrete local pairwise exchange interactions observed in the hyperfine field distributions by Mössbauer spectroscopy that I have previously reported. [179] This experimental data, along with assumptions from prior work, allows us to solve equation 5.9 for the $\frac{\partial \ln d}{\partial P}$ term and calculate the expectation value of the d -orbital radius of the FeCoNiCuMn HEA as a function of P (Fig. 5.6a). The calculations assume the alloy to lie on the righthand side of the Bethe-Slater curve based on its electrons to atom ratio and approximate d -orbital extent at $P=0$, which are close to solid state values calculated by Slater and Mann [34, 180].

Our results clearly show the d -orbital contraction, accompanying d -band filling and nuclear screening, is important to understanding J_{ex} in alloys. While the Bethe Slater curve is often used to describe the variation of J_{ex} with large atomic spacing variations [38, 39], d -orbital contraction must be considered to precisely account for its variation in disordered alloys with similar interatomic spacings. This is an important consideration in my analysis of $T_c(P)$. Considering changes in atomic spacing (D) alone, we would expect T_c to increase with P in the FeCoNiCuMn HEA given that $T_c(P=0)$ places it just below Ni on the Bethe Slater curve, and decreasing D independent of d would move the point to the left. However, I experimentally observe a decrease in T_c (movement to the right), which I calculate to be explained by a small decrease in the d -orbital spatial extent (a 3.5% decrease at $P=1\text{GPa}$). Because the d -orbital radius decreases more rapidly than the atomic spacing, the $\frac{D}{d}$ ratio increases (Fig. 5.6b).

The relative importance of d -orbital contraction on J_{ex} is evaluated considering the first

and second terms in equation 5.9 separately. The differential in the first term accounts for the change in atomic spacing (D), while the second term depends on the change in d-orbital spatial extent. A direct comparison of the size of each term (Fig. 5.7) shows that, particularly at low pressures, the change in d-orbital radius dominates the overall change in exchange J_{ex} . If we directly compare the change in D and d , ($(\frac{dD}{dP})$ vs $(\frac{dd}{dP})$), the derivative terms intersect at 7GPa, after which the $\frac{dD}{dP}$ derivative becomes the larger of the two. However, the non-derivative multipliers for each term scale the influence of each such that the $(\frac{dd}{dP})$ term always contributes more significantly to changes in J_{ex} . Therefore it would require an enormous applied pressures to cause a change in sign in J_{ex} . Thus, the inclusion of d-orbital contraction is essential to understand variations in J_{ex} in these HEAs. The initial contraction is postulated to be so large due to the compressibility of the free electrons allowed by their increased density in the FCC interstices of the alloy. This charge redistribution decreases the amount of d-orbital screening between atoms. However, Coulomb repulsion between s and d electrons eventually impedes this compression as orbitals necessarily push closer to the nucleus of neighboring atoms. The crossover at higher applied pressures may provide the driving force for their rotation in a structural or magnetic phase transformation.

There are limits to the conclusions I can draw from these results, primarily due to the distribution of magnetic exchange resulting from the sum of discrete interactions among various magnetic atoms. Mean field theory can only provide an estimate of the exchange energy for this system based on averages. The breadth of the magnetic transitions reflects the fluctuations in exchange interactions about this average and is a function of the d-orbital extent, also averaged over several atomic species. Nevertheless, this analysis clearly illustrated the relative significance of d-orbital contraction as compared with traditional analysis of interatomic spacings alone in determining J_{ex} .

5.4 Summary

Applied pressure is a powerful tool for probing alloy systems and gaining a better understanding of their structural and magnetic properties. High pressure x-ray diffraction revealed a large bulk moduli aided by negative strain in the system which bolsters the conventional idea of high entropy alloys experiencing an advantageous “cocktail effect” upon mixing. High pressure magnetometry showed that the Curie temperature of these alloys decreases with applied pressure, contrary to our original predictions based on a simplistic view of the Bethe-Slater curve. I then combined the $M(T)$ pressure data, pressure-varied crystallographic data, and inferences about d-orbital behavior from the disordered γ phase Fe-Ni T_c to demonstrate the importance of considering atomic spacing and d-orbital spatial extent as separate variables when discussing changes in magnetic exchange energy under pressure. I showed that the pressure dependent T_c for FeCoNiCuMn alloys can be understood to be primarily due to the contraction of d-orbitals.

Further applied pressure work on the effects of pressure on these alloys will be to use Mössbauer spectroscopy under high pressure to observe the change in the strength of the discrete exchange interactions visible in the hyperfine magnetic fields. In chapter 6, I will go into more depth about the low temperature transition seen in figure 5.2 which did not shift with applied pressure as one may have expected.

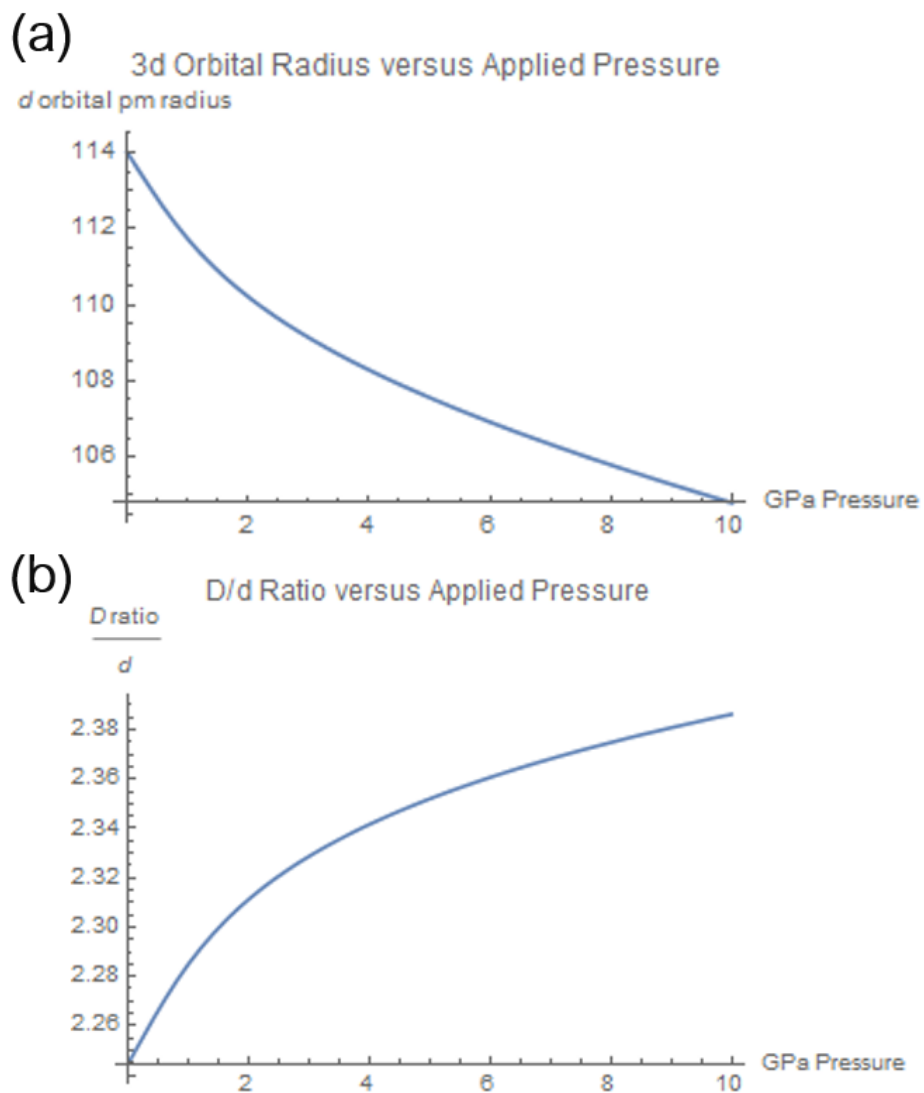


Figure 5.6: (a) d orbital diameter versus applied pressure for the $\text{FeCoNiCu}_{19}\text{Mn}_{21}$ alloy. (b) $\frac{D}{d}$ ratio with applied pressure, which increases despite both D and d decreasing with pressure.

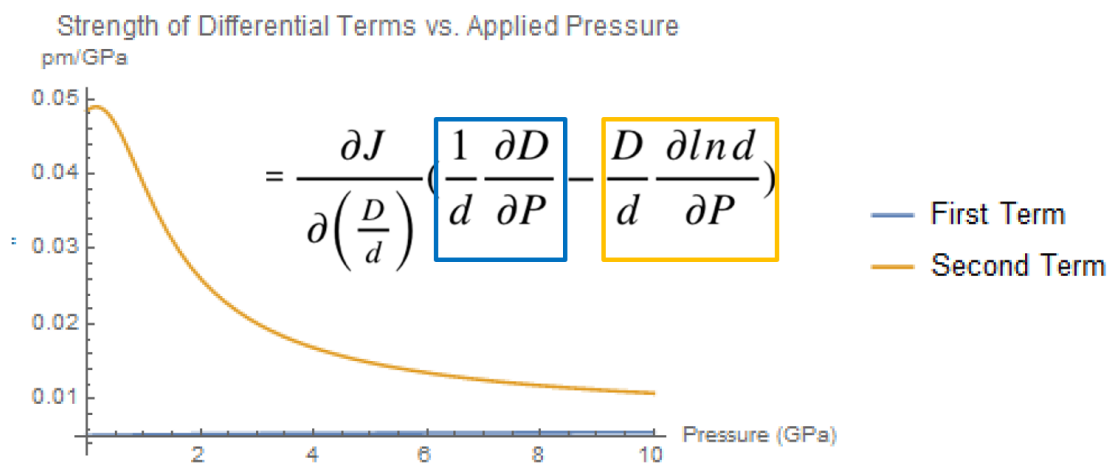


Figure 5.7: Magnitude of first term and second term from parentheses in equation 5.9.

Chapter 6

Analysis of Low Temperature

Magnetic Transition in FeCoNiCuMn System

Zero field cooling is a process in which a magnetic sample is first heated above its Curie temperature (until it is paramagnetic), and then cooled to a lower temperature without the influence of an applied magnetic field. Zero field cooling measurements are performed to reveal magnetic behavior that may be masked by applying a field with cooling, and may also show evidence of thermal hysteresis in a magnetic material. Zero field cooling of alloys in the FeCoNiCuMn system (to 5K) reveals a low temperature magnetic transition in the field heated magnetization versus temperature curve which is not observed upon field cooling. In near equiatomic FeCoNiCuMn it is a weak effect—this transition is not present even under cooling fields as small as 20Oe, the smallest field that can be applied with accuracy in the PPMS. However, upon zero field cooling, some amount of decreased magnetization is present upon heating with up to 5000 Oe applied upon measurement (Fig. 6.1)

This effect has been found to occur at 50K among alloys in each of the pseudo-binary variations of FeCoNiCuMn, so it is not sensitive to small compositional changes (Fig. 6.2).

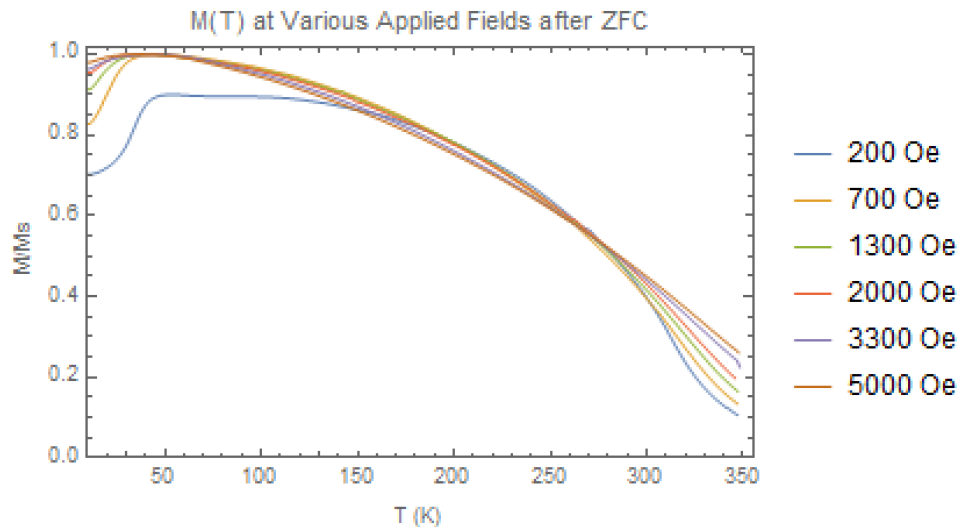


Figure 6.1: Magnetization heating curves at different applied fields, taken after zero field cooling.

We can see in the pressure dependence data for these alloys (Fig. 5.2) that the transition temperature also does not shift with applied pressure. It is also necessary to point out that the non-zero offset of each curve before the transition is likely due to remnant magnetization in the superconducting solenoid used to produce magnetic fields in the PPMS system. It is incredibly difficult to completely remove the remnant field in the solenoid, and thus there will always be a small applied field that changes between measurements which are dependent on the last measurement made. I consider several different potential explanations for this behavior.

6.1 Magnetic Domain Formation

The first cause to consider is that this behavior is due to demagnetization effects due to the formation of magnetic domains upon zero field cooling. If magnetic domains formed upon cooling, they would require an applied field of a certain strength to rotate the domains in the field direction. For a small field, this rotation would not take place until a high enough thermal energy was reached as well. Domain rotation could explain why the

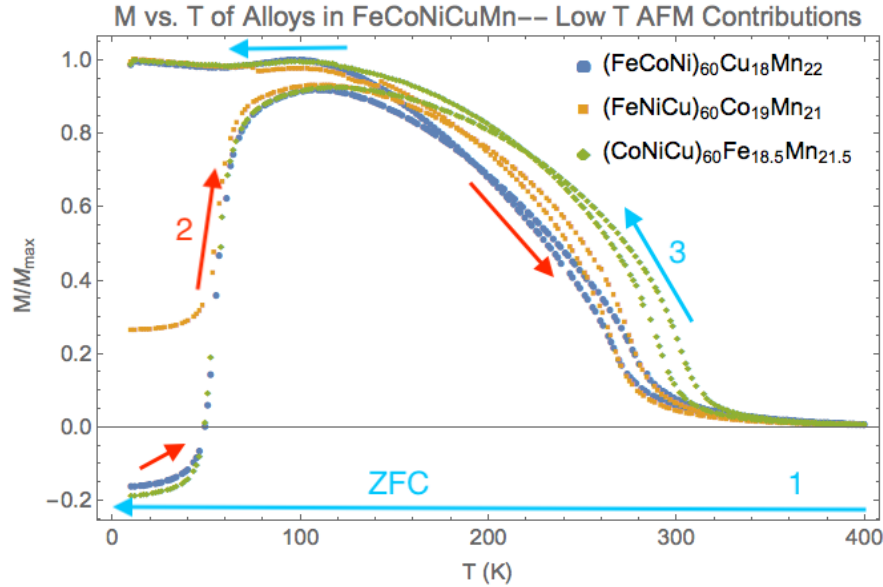


Figure 6.2: Magnetization vs. temperature measurements (with ZFC) demonstrating that the low temperature transition is not changed with small compositional variation.

transition is not observed to change with applied pressure while the ferromagnetic to paramagnetic transition does, as it is a structural effect. To assess whether domains were forming, I zero field cooled the samples to 100K (above the transition temperature observed) and measured magnetization versus temperature upon heating for the samples measured in Fig. 6.2. Because domains would form continuously as the sample is cooled, we would expect to still see some evidence of the sample transitioning from a demagnetized state to magnetized if domains were the cause of this transition. However, no such transition was observed in these measurements. This does not rule out domains entirely, as very weak domains may not be observable under these measurements. To observe the domain behavior directly, we must perform low temperature magneto-optical Kerr effect (MOKE) measurements to obtain direct images of the magnetic domain formation. These MOKE measurements will be part of the future work done to complete this project.

6.2 Antiferromagnetic Exchange

Another possible cause of the low temperature transition is antiferromagnetic exchange in these alloys, which would be caused primarily by the presence of manganese and close-packed iron. The Néel temperature of this phase would be lower than pure Mn ($T_n=100\text{K}$) at 50K, but this would not be surprising due to the influence of ferromagnetic exchange from the presence of other atoms surrounding the atoms contributing antiferromagnetic exchange. [181] This type of antiferromagnetic to ferromagnetic transition has been observed in several alloy systems, such as Fe-Rh and SmCrO_3 . [182–189] The study of this effect in SmCrO_3 describes a system in which there is a frozen fraction of antiferromagnetic states corresponding to kinetic behavior in the material. This is hypothesized to be a nonequilibrium magnetic state with a configuration of ferro- or ferrimagnetic and antiferromagnetic clusters frozen in the sample, which is overcome more easily with larger fields. This paper performs several experiments worth replicating for my own alloys to better explore the low T behavior. However, the effect I see seems much weaker than the effect they observe as this effect is overcome with a 20Oe cooling field, though we do see this behavior remains weakly present after zero field cooling upon the application of fields up to 5000 Oe (0.5T).

The evidence that complicates the antiferromagnetic state hypothesis is the fact that this transition was not found to change with applied pressure (Fig. 5.2). Because the applied pressure is forcing the atoms in the alloy closer together, this should change the strength of the exchange interactions. We see that this is the case for the ferromagnetic to paramagnetic transition at 300K, but this does not occur at the 50K transition. Studies of the effects of pressure on antiferromagnetic states due to manganese bonds in other alloys show that the transition is field dependent as well as pressure dependent, as the applied pressure stabilizes the antiferromagnetic phase as manganese is pushed closer together (T_N increases) [190]. Though we do not observe this for our alloys, it may be because of the presence of other atoms whose exchange interactions upon applied pressure increase at a similar magnitude with opposite sign as the antiferromagnetic manganese and iron interactions. This would

be possible specifically because of the presence of nickel and cobalt—as we can see from the Bethe-Slater curve (Fig. 1.10), both atoms should experience an increase in exchange bond strength as their atomic spacing decreases.

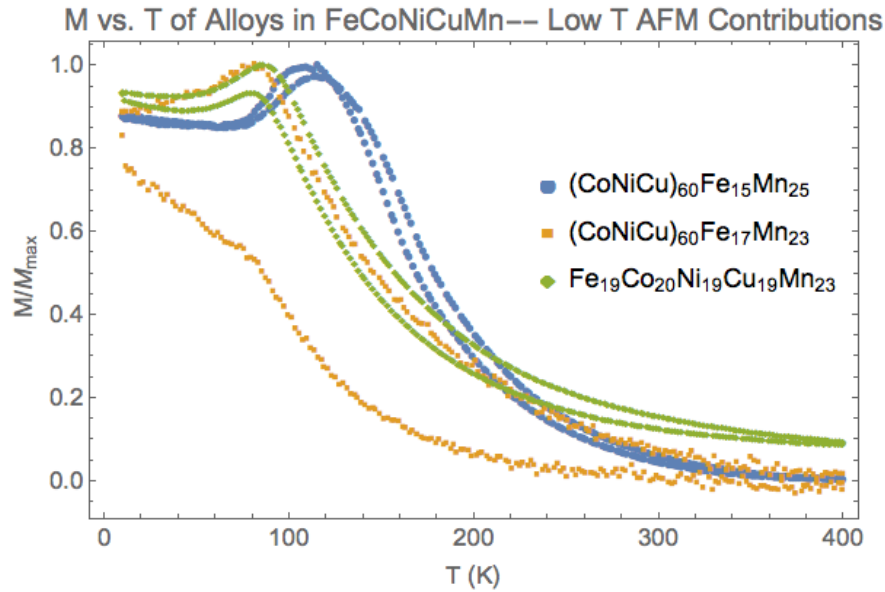


Figure 6.3: Magnetization vs. temperature measurements for alloys with greater compositional variation showing the emergence of a low temperature dip in the magnetization.

As we increase the manganese content in these alloys (at% Mn > 23%), we can see a dip in the magnetization at low temperatures that remains during field cooling (Fig. 6.3). This dip contributes validity to the idea of an antiferromagnetic phase that is getting stronger, and its occurrence is around the Néel transition of manganese (100 K). X-ray diffraction (XRD) of these alloys confirms that they are single phase at room temperature, and electron dispersive spectroscopy (EDS) confirms that there is no obvious clustering of manganese causing the dip, though nanoscale analysis such as atomic probe spectroscopy would be necessary to confirm this more definitively. The decrease in magnetization at 115K after the magnetization reaches a maximum in the magnetization versus temperature curve for high Mn samples may then be the result of competing magnetic exchange strengths instead of an outright transition.

Exploration of samples with greater compositional variation may yield more definitive

information on the antiferromagnetic behavior and give us insight into the weaker effect observed in the samples with near-equiatomic compositions. The most direct way to explore this behavior further in both cases would be to perform Mössbauer spectroscopy below the transition temperature on these alloys, as we would expect to see significant change in the hyperfine field distributions above and below the transition for an antiferromagnetic phase, as peaks in the distribution would arise, disappear, and change in intensity fairly rapidly.

6.3 Summary

I have identified a low temperature transition in the FeCoNiCuMn that I am still working to explain, but have provided evidence for two potential explanations. I have increased the compositional variation in the system to a point at which this low temperature transition is strong enough to be seen upon field cooling, but further study will require direct imaging using low temperature MOKE and probing with antiferromagnetic sensitive techniques at low temperatures. I also hope to take these measurements at low temperatures under applied pressure, which will confirm whether the relative summed strength of the ferromagnetic interactions and antiferromagnetic interactions is unchanged upon applied pressure despite individual values changing, explaining why the transition is not observed to shift in Fig. 5.2.

Chapter 7

Conclusions and Future Work

The focus of this research project for the last four years has been to develop magnetic high entropy alloys for magnetocaloric applications. I began with three main hypotheses:

- (1) The random distribution of several magnetic atoms in high entropy alloys will result in a broadened magnetocaloric effect which will increase the refrigeration capacity through widening the full width half max of the magnetic entropy curves.
- (2) This broadening is the summation of several discrete exchange interactions between nearest and next nearest neighbors of different atomic species in these alloys.
- (3) The compositions of these magnetic high entropy alloys can be varied to alter the magnetic properties of the alloy, such as the saturation magnetization and the Curie temperature (T_c), which must be tuned to room temperature for my materials to be viable magnetic refrigeration candidates.

Our work began by synthesizing several high entropy alloys of the form FeCoNiCuX and determining the most promising alloy to study further through magnetic and structural analysis. Because of the lower T_c , high magnetization, and structural homogeneity, FeCoNiCuMn was identified as the most viable alloy for magnetocaloric refrigeration, validating hypothesis 1. I began more in depth exploration of this high entropy alloy system

by synthesizing pseudo-binary alloys in which one element was decreased in tandem with an increase in manganese in order to study the influence of each atomic species on the system and determine the composition of alloys in the system with room temperature T_c with the highest refrigeration capacity, providing clear evidence validating hypothesis 3. Two alloys, $\text{Fe}_{0.975}\text{CoNiCuMn}_{1.025}$ and $\text{FeCoNiCu}_{0.95}\text{Mn}_{1.05}$, had the largest refrigeration capacities, which were roughly 140 J/kg at a 5T applied field. This RC value is not large enough to make these alloys commercially viable for large-scale magnetocaloric refrigeration, but the interesting magnetic properties of this specific alloy system warranted further exploration which could contribute to the development of other useful magnetic high entropy alloys in future work.

I turned to Mössbauer spectroscopy to better understand the individual magnetic exchange interactions in these alloys, and the hyperfine field distributions revealed discrete exchange interactions which are the primary cause of the broad magnetocaloric effect exhibited by this alloy system, verifying hypothesis 2. From these hyperfine field distributions, I calculated the contribution of each atom to the average strength of the alloys' internal hyperfine fields, and concluded that the low contribution from Fe is a result of the presence of both antiferromagnetic and ferromagnetic exchange between Fe atoms, which average out to a low, positive contribution. This interesting result led to more questions, particularly about how much the application of pressure could reveal about the complex magnetic behavior of the system. This led to the creation of two more hypotheses:

- (4) The T_c of these alloys can be shifted using applied pressure because the strength of each discrete interaction will change
- (5) The change in magnetic behavior with applied pressure will be due to a change in both atomic spacing and d-orbital spatial extent of the atomic species, and these changes will affect the individual exchange interaction strengths between atoms.

I first measured the magnetic behavior of these alloys under applied pressure and ob-

served the change in magnetization versus temperature of $\text{FeCoNiCu}_{0.95}\text{Mn}_{1.05}$ with applied pressure and found that T_c for these alloys decreases with applied pressure, verifying hypothesis 5. However, it was immediately clear that a simple explanation of decreasing atomic spacing could explain the decrease in T_c given the location of the FeCoNiCuMn on the Bethe Slater curve. I then calculated the change in the expectation value of the d-orbital radius alongside the change in atomic spacing for these alloys. These calculations demonstrated that consideration of the change in d-orbital extent upon applied pressure for these magnetic alloys is not only important, but absolutely crucial to understanding the magnetic behavior of these alloys, verifying hypothesis 5.

Our original hypothesis 6 has yet to be verified experimentally, but I still provide some evidence which could be used to support two potential explanations for a low temperature magnetic transition observed for these alloys upon zero field cooling. Low temperature magnetic probing at various fields suggests a weak antiferromagnetic phase, but future work using low temperature MOKE imaging will help to directly image the magnetic behavior over this transition and will be required to fully explain the observed behavior. Additionally, future work on this project will be focused on obtaining Mössbauer spectra for alloys under applied pressure and at low temperatures using the Advanced Photon Source (APS) at Argonne National Lab, both to observe this transition further, and to understand the complex shifts in exchange energy that occur with applied pressure at temperatures which will produce well-resolved spectra. Future work on these alloys could also include other composition focused experiments to observe whether there is any nano-scale segregation occurring which is not captured in EDS experiments. These would be achieved through atom probe tomography or anomalous XRD experiments [115].

Future magnetocaloric alloy research in the group outside of the FeCoNiCuMn system will extend high entropy ideas to ordered alloy systems. Ordered alloy systems such as $\text{La}(\text{Fe},\text{Si})_{13}$ will be altered such that high entropy configurations will be introduced to the $(\text{Fe},\text{Si})_{13}$ site and potentially also to the La site, which would work to broaden the magnetic

entropy curve of these typically first-order magnetic alloys in a similar fashion to the pure HEAs studied in this work.

Bibliography

- [1] J. C. Slater. The ferromagnetism of nickel. II. temperature effects. *Phys. Rev.*, 49:931–937, Jun 1936.
- [2] NDT Resource Center. The hysteresis loop and magnetic properties (retrieved from <https://www.nde-ed.org>).
- [3] V. Franco. Determination of the magnetic entropy change from magnetic measurements: the importance of the measurement protocol. *Lake Shore Cryotronics, Inc.*, Application Note.
- [4] V. Franco, J.S. Blázquez, J.J. Ipus, J.Y. Law, L.M. Moreno-Ramírez, and A. Conde. Magnetocaloric effect: From materials research to refrigeration devices. *Progress in Materials Science*, 93(112-232), 2018.
- [5] V. Chaudhary, Z. Wang, A. Ray, I. Sridhar, and R. V. Ramanujan. Self pumping magnetic cooling. *Journal of Physics D: Applied Physics*, 50(03LT03), 2017.
- [6] J. Liu, T. Gottschall, K. P. Skokov, J. D. Moore, and O. Gutfleisch. Giant magnetocaloric effect driven by structural transitions. *Natural Materials*, 11(620), 2012.
- [7] S. Wang. Atomic structure modeling of multi-principal-element alloys by the principle of maximum entropy. *Entropy*, 15(12), 2013.
- [8] Y. Y. Chen, T. Duval, U.D. Hung, J.W. Yeh, and H.C. Shih. Microstructure and electrochemical properties of high entropy alloys—a comparison with type-304 stainless steel. *Corro. Sci.*, 47:2257–2279, 2005.
- [9] A.A. Shirzadi, T. Koziel, G. Cios, and P. Bala. Development of auto ejection melt spinning (AEMS) and its application in fabrication of cobalt-based ribbons. *J. Mat. Proc. Tech.*, 264:377–381, 2019.
- [10] J. Grebenkemper. Powder x-ray diffraction (retrieved from <http://chemwiki.ucdavis.edu>).
- [11] H. Hiroyoshi, A. Hoshi, H. Fujimori, and Y. Nakagawa. Arrott-Noakes plots for magnetization of some 3d-transition metals and alloys in high magnetic fields. *J. Phys. Soc. Jap.*, 48(3):830, 1980.

- [12] D. Evans. Introduction to Mössbauer spectroscopy (retrieved from <http://www.rsc.org/Membership/Networking/InterestGroups/MossbauerSpect>, 2014).
- [13] Chemistry LibreTexts. Mössbauer spectroscopy (retrieved from <https://chem.libretexts.org>).
- [14] J. Van Lierop and D.H. Ryan. Selective excitation double Mössbauer spectroscopy. *Hyper. Inter.*, 141/142(1):141–144, 2002.
- [15] EasyLab Technologies Ltd. *EasyLab Mcell 10 User Guide*.
- [16] M. E. McHenry and D. E. Laughlin. “*Magnetic Properties of Metals and Alloys. Chapter 19 of Physical Metallurgy - 5th Ed.*”. Elsevier, 2015.
- [17] K. Uruga, K. Sawada, Y. Enokida, and I. Yamamoto. Liquid metal extraction for removal of molybdenum from molten glass containing simulated nuclear waste elements. *J. Nucl. Sci. Tech.*, 45(10):1063–1071, 2008.
- [18] R. H. Davies, A.T. Dinsdale, J.A. Gisby, J.A.J. Robinson, and S.M. Martin. MT-DATA - thermodynamics and phase equilibrium software from the national physical laboratory. *CALPHAD*, 26(2):229–271, 2006.
- [19] C.W. Bale, E. Bélisle, P. Chartrand, S.A. Deckerov, G. Eriksson, A.E. Gheribi, K. Hack, I. H. Jung, Y. B. Kang, J. Melançon, A. D. Pelton, S. Petersen, C. Robelin, J. Sangster, P. Spencer, and M.A. Van Ende. FactSage thermochemical software and databases. *CALPHAD*, 54:35–53, 2016.
- [20] J.O. Andersson, T. Helander, L. Höglund, P.F. Shi, and B. Sundman. Thermo-Calc and DICTRA, computational tools for materials science. *CALPHAD*, 26:273–312, 2002.
- [21] A. Bravais. Mémoire sur les systèmes formés par les points distribués régulièrement sur un plan ou dans l’espace. *J. Ecole Polytech*, 19:1–128, 1850.
- [22] B.R. Braeckman and D. Depla. On the amorphous nature of sputtered thin film alloys. *Acta Materialia*, 109:323–329, 2016.
- [23] G.E.R. Schulze. *Metallphysik: Ein Lehrbuch*. Berlin, Akademie-Verlag, 1st edition, 1967.
- [24] J. C. Slater and H. C. Verma. The theory of complex spectra. *Phys. Rev.*, 34(2):1293–1322, 1929.
- [25] P. Weiss. L’hypothese du champ moléculaire et la propriété ferromagnétique. *J. Phys.*, 6:661, 1907.
- [26] W. Heisenberg. On the theory of ferromagnetism. *Z. Phys.*, 49:619, 1928.

- [27] W. Kohn and L. Sham. Self-consistent equations including exchange and correlation effects. *Phys. Rev.*, 140(A1133), 1965.
- [28] P. Hohenberg and W. Kohn. Inhomogeneous electron gas. *Physical Review*, 136(3B):B864–B871, 1964.
- [29] H. Ebert, D. Kodderitzsch, and J. Minar. Calculating condensed matter properties using the KKR-Green’s function method – recent developments and applications. *Rep. Prog. Phys.*, 74(096501), 2011.
- [30] J. M. MacLaren, T. C. Schulthess, W. H. Butler, R. A. Sutton, and M. E. McHenry. Calculated exchange interactions and Curie temperature of equiatomic B2 FeCo. *J. Appl. Phys.*, 85:4833–4835, 1999.
- [31] P.A.M. Dirac. *Principles of Quantum Mechanics*. International Series of Monographs on Physics. Oxford University Press, 4th edition, 1982.
- [32] W. Heitler and F. London. Wechselwirkung neutraler atome und homöopolare binding nach der quantenmechanik. *Zeit. Phys.*, 44:455–472, 1927.
- [33] H. A. Bethe and A. Sommerfeld. *Handbuch der Physik 24*. J. Springer, 1933.
- [34] J. C. Slater. Atomic shielding constants. *Phys. Rev.*, 36:57–64, 1930.
- [35] J. C. Slater. Electronic structure of alloys. *J. Appl. Phys.*, 8:385, 1937.
- [36] J. R. Smith, H. Schlosser, W. Leaf, J. Ferrante, and J. H. Rose. Global expression for representing cohesive-energy curves. *Physical Review B*, 44(17):9696–9699, 1991.
- [37] R. Stuart. Direct exchange in ferromagnets. *Physical Review*, 120(2), 1960.
- [38] A. Bruno and J. P. Lascaray. Nearest and next nearest neighbor exchange interaction between magnetic ions in II VI semimagnetic semiconductors. *Journal of Crystal Growth*, 101(1-4), 1990.
- [39] P. J. Webster and R. S. Tebble. Magnetic and chemical order in Pd₂MnAl in relation to order in the Heusler alloys Pd₂MnIn, Pd₂MnSn, and Pd₂MnSb. *J. Appl. Phys.*, 39(471), 1968.
- [40] B.D. Cullity and C.D. Graham. *Introduction to Magnetic Materials*. IEEE Press, John Wiley and Sons, Hoboken, NJ, 2nd edition, 2009.
- [41] M. E. McHenry and M. Lucas. *Characterization of Materials*, pages 1–12. John Wiley, New York, NY, 2nd edition, 2012.
- [42] H. Ucar. Metastable gamma-FeNi nanostructures for magnetic refrigeration near room temperature (unpublished doctoral dissertation). Carnegie Mellon University, Pittsburgh, PA. 2013.

- [43] M. E. Wood and W. H. Potter. General analysis of magnetic refrigeration and its optimization using a new concept: maximization of refrigerant capacity. *Cryogenics*, 25(12), 667-683.
- [44] V. I. Zverev, A. M. Tishin, and M. D. Kuzmin. The maximum possible magnetocaloric delta effect. *Journal of Applied Physics*, 107(043907), 2010.
- [45] W.F. Giauque and D.P. MacDougall. Attainment of temperatures below 1° absolute by demagnetization of $\text{Gd}_2(\text{SO}_4)_3 \cdot 8\text{H}_2\text{O}$. *APS Physical Review*, 43(768), 1933.
- [46] V. Franco, A. Conde, M. D. Kuz'Min, and J. M. Romero-Enrique. The magnetocaloric effect in materials with a second order phase transition: Are T_c and T_{peak} necessarily coincident? *Journal of Applied Physics*, 105(7), 2009.
- [47] K. A. Gschneidner Jr. and V. K. Pecharsky. Magnetocaloric materials. *Ann. Rev. Mater. Sci.*, 30:387–429, 2000.
- [48] E. Bruck, O. Tegus, L. Zhang, X.W. Li, F.R. de Boer, and K.H.J. Buschow. Magnetic refrigeration near room temperature with Fe_2P -based compounds. *J. All. Comp.*, 383:32–36, 2004.
- [49] R. Bjork, C.R.H. Bahl, A. Smith, and N. Pryds. Review and comparison of magnet designs for magnetic refrigeration. *International Journal of Refrigeration*, 33(3), 2010.
- [50] G. Brown. Magnetic heat pumping near room temperature. *Journal of Applied Physics*, 47(8), 1976.
- [51] C. Bahl, T. Petersen, N. Pryds, A. Smith, and T. Petersen. A versatile magnetic refrigeration test device. *Review of Scientific Instruments*, 79(9), 2008.
- [52] K. Engelbrecht, C. R. H. Bahl, and K. K. Nielsen. Experimental results for a magnetic refrigerator using three different types of magnetocaloric material regenerators. *International Journal of Refrigeration*, 34(4):1132–1140, 2011.
- [53] X. Bohigas, E. Molins, A. Roig, J. Tejada, and X. Zhang. Room-temperature magnetic refrigerator using permanent magnets. *IEEE Transactions on Magnetics*, 36, 2000.
- [54] J. H. Jensen and M. G. Abele. Maximally efficient permanent magnet structures. *Journal of Applied Physics*, 79(2), 1996.
- [55] G. Nikly and C. Muller. Technical and economical criteria to design and realize a magneto-caloric heat pump. *Proceedings of the 2nd International Conference of Magnetic Refrigeration at Room Temperature, Portoroz, Slovenia*, 2007.
- [56] K. Engelbrecht, G. Nellis, and S. Klein. Modeling the transient behavior of an active magnetic regenerative refrigerator. *International Refrigeration and Air Conditioning Conference*, 822, 2006.

- [57] C. B. Zimm, A. Sternberg, A. G. Jastrab, A. M. Boeder, Jr. L. M. Lawton, and J. J. Chell. Rotating bed magnetic refrigeration apparatus. *U.S. Patent Application, US 2002/0053209 A1*, 2002.
- [58] T. Okamura, K. Yamada, N. Hirano, and S. Nagaya. Performance of a room-temperature rotary magnetic refrigerator. *International Journal of Refrigeration*, 29(8):1327 – 1331, 2006. Magnetic Refrigeration at Room Temperature.
- [59] D. Eriksen, K. Engelbrecht, C.R.H. Bahl, R. Bjørk, K.K. Nielsen, A.R. Insinga, and N. Pryds. Design and experimental tests of a rotary active magnetic regenerator prototype. *International Journal of Refrigeration*, 58:14 – 21, 2015.
- [60] C. A. Sawyer, A. H. Habib, K. N. Collier, K. Miller, C. L. Ondeck, and M. E. McHenry. Modeling of temperature profile during magnetic thermotherapy for cancer treatment. *Journal of Applied Physics*, 105(07B320-22), 2009.
- [61] V. Chaudhary and R.V. Ramanujan. Magnetocaloric properties of Fe-Ni-Cr nanoparticles for active cooling. *Sci. Rep.*, 6:35156, 2016.
- [62] V. K. Pecharsky and K. A. Gschneidner Jr. Giant magnetocaloric effect in $\text{Gd}_5(\text{Si}_2\text{Ge}_2)$. *Phys. Rev. Lett.*, 78:4494, 1997.
- [63] V. Provenzano, A. J. Shapiro, and R. D. Shull. Reduction of hysteresis losses in the magnetic refrigerant $\text{Gd}_5\text{Ge}_2\text{Si}_2$ by the addition of iron. *Nature*, 429:853, 2004.
- [64] T. Krenke, E. Duman, M. Acet, E. F. Wassermann, X. Moya, L. Mañosa, and A. Planes. Inverse magnetocaloric effect in ferromagnetic Ni-Mn-Sn alloys. *Nat. Mat.*, 4:450, 2005.
- [65] I. Škorvánek and J. Kováč. Magnetocaloric behavior in amorphous and nanocrystalline FeNbB soft magnetic alloys. *Czech. J. Phys.*, 54 (Suppl. D):D189, 2004.
- [66] V. Franco, J. S. Blázquez, C. F. Conde, and A. Conde. A FINEMET-type alloy as a low-cost candidate for high-temperature magnetic refrigeration. *Appl. Phys. Lett.*, 88:042505, 2006.
- [67] V. Franco, J. M. Borrego, C. F. Conde, and Conde A. Refrigerant capacity of FeCr-MoCuGaPCB amorphous alloys. *J. Appl. Phys*, 100:083903, 2006.
- [68] J. J. Ipus, J. S. Blázquez, V. Franco, A. Conde, and L. F. Kiss. Magnetocaloric response of $\text{Fe}_{75}\text{Nb}_{10}\text{B}_{15}$ powders partially amorphized by ball milling. *J. Appl. Phys*, 105:123922, 2009.
- [69] K. J. Miller, M. Sofman, K. McNerny, and M. E. McHenry. Metastable gamma-FeNi nanostructures with tunable Curie temperatures. *Journal of Applied Physics*, 107(09A305-307), 2010.
- [70] J.Y.Law, V.Franco, A.Conde, S.J.Skinner, and S.S.Pramana. Modification of the order of the magnetic phase transition in cobaltites without changing their crystal space group. *J. Alloys Comp.*, 777:1080–1086, 2019.

- [71] L.M. Moreno-Ramirez, C. Romero-Muniz, J.Y. Law, V. Franco, A. Conde, I.A. Radulov, F. Maccari, K.P. Skokov, and O. Gutfleisch. The role of Ni in modifying the order of the phase transition of $\text{La}(\text{Fe,Ni,Si})_{13}$. *Act. Mat.*, 160:137–146, 2018.
- [72] L. M. Moreno-Ramirez, J. Law, C. Romero-Muniz, V. Franco, A. Conde, F. Maccari, I. A. Radulov, K. Skokov, and O. Gutfleisch. Finding the separation between first- and second-order phase transitions in $\text{La}(\text{Fe,Ni,Si})_{13}$ magnetocaloric materials. *2018 IEEE International Magnetism Conference (INTERMAG)*, 2018.
- [73] H. Ucar, J. J. Ipus, V. Franco, M. E. McHenry, and D. E. Laughlin. Overview of amorphous and nanocrystalline magnetocaloric materials operating near room temperature. *JOM*, 64(782), 2012.
- [74] E. Palacios, G. F. Wang, R. Burriel, V. Provenzano, and R. D. Shull. Direct measurement of the magnetocaloric effect in $\text{Gd}_5\text{Si}_2\text{Ge}_{1.9}\text{Ga}_{0.1}$. *Journal of Physics: Conference Series*, 200(9):092011, Jan 2010.
- [75] F. Canepa, S. Cirafici, M. Napolitano, and F. Merlo. Magnetocaloric properties of Gd_7Pd_3 and related intermetallic compounds. *IEEE Transactions on Magnetism*, 38(5):3249–3251, 2002.
- [76] R. D. Shull, V. Provenzano, A. J. Shapiro, and A. Fu. The effects of small metal additions (Co,Cu,Ga,Mn,Al,Bi,Sn) on the magnetocaloric properties of the $\text{Gd}_5\text{Ge}_2\text{Si}_2$ alloy. *J. Appl. Phys.*, 99(08K908), 2006.
- [77] X. B. Liu and Z. Altounian. Magnetocaloric effect in Co-rich $\text{Er}(\text{Co}_{1-x}\text{Fe}_x)_2$ Laves phase. *J. Appl. Phys.*, 103(07B304), 2008.
- [78] X. W. Li, O. Tegus, L. Zhang, W. Dagula, E. Bruck, K. H. J. Buschow, and F. R. de Boer. Magnetic properties of $\text{MnFeP}_{0.5}\text{As}_{0.5-x}\text{Ge}_x$. *IEEE Transactions on Magnetism*, 39(5):3148–3150, 2003.
- [79] T. Mazet, H. Ihou-Mouko, and B. Malaman. Mn_3Sn_2 : A promising material for magnetic refrigeration. *Appl. Phys. Lett.*, 89(022503), 2006.
- [80] J. J. Ipus, H. Ucar, and M. E. McHenry. Near room temperature magnetocaloric response of an $(\text{FeNi})\text{ZrB}$ nanocomposite alloy. *IEEE Transactions in Magnetism*, 47, 2011.
- [81] H. Ucar, J. J. Ipus, D. E. Laughlin, and M. E. McHenry. Tuning the Curie temperature of gamma-FeNi nanoparticles for magnetocaloric applications by controlling the oxidation kinetics. *J. Appl. Phys.*, 113:17A918–20, 2013.
- [82] H. Ucar, M. Craven, D.E. Laughlin, and M. E. McHenry. Effect of Mo addition on structure and magnetocaloric effect in gamma-FeNi nanocrystals. *Journal of Electronic Materials*, 43(1):137–141, 2014.

- [83] N. J. Jones, H. Ucar, J. J. Ipus, M.E. McHenry, and D. E. Laughlin. The effect of distributed exchange parameters on magnetocaloric refrigeration capacity in amorphous and nanocomposite materials. *Journal of Applied Physics*, 11(07A334), 2012.
- [84] K. A. Gallagher, M. A. Willard, V. Zabenkin, D. E. Laughlin, and M. E. McHenry. Distributed exchange interactions and temperature dependent magnetization in amorphous $\text{Fe}_{88-x}\text{Co}_x\text{Zr}_7\text{B}_4\text{Cu}_1$ alloys. *Journal of Applied Physics*, 85:5130–5132, 1999.
- [85] H. Ucar, J. J. Ipus, V. Franco, M. E. McHenry, and D. E. Laughlin. Overview of magnetocaloric materials operating near room temperature. *J. Met.*, 64:772–781, 2012.
- [86] J. J. Ipus, P. Herre, P. R. Ohodnicki, and M. E. McHenry. High temperature XRD determination of the BCC-FCC transformation temperature in $(\text{Fe}_{70}\text{Ni}_{30})_{88}\text{Zr}_7\text{B}_4\text{Cu}_1$ nanocomposites. *J. Appl. Phys.*, 11:07A323–07A325–27, 2012.
- [87] U. Dahlborg, J. Cornide, M. Calvo-Dahlborg, T.C. Hansen, A. Fitch, Z. Leong, S. Chambrelaud, and R. Goodall. Structure of some CoCrFeNi and CoCrFeNiPd multicomponent HEA alloys by diffraction techniques. *Journal of Alloys and Compounds*, 681, 2016.
- [88] F. He, Z. Wang, Q. Wu, J. Li, J. Wang, and C.T. Liu. Phase separation of metastable CoCrFeNi high entropy alloy at intermediate temperatures. *Scripta Materialia*, 126, 2017.
- [89] S. J. Lin J. Y. Gan T. S. Chin T. T. Shun C. H. Tsau S. Y. Chang J. W. Yeh, S. K. Chen. Nanostructured high-entropy alloys with multiple principal elements: Novel alloy design concepts and outcomes. *Adv. Eng. Mater.*, 6(299), 2004.
- [90] M.A. Lucas, D. Belyea, N. Bryant, E. Michel, Z. Turgut, S. Leontsev, J. Horwath, S. L. Semiatin, M. E. McHenry, and C. W. Miller. FeCoCr_xNi alloys for magnetic refrigeration applications. *Journal of Applied Physics*, 113(17A923-17A923-03), 2013.
- [91] D. D. Belyea, M. S. Lucas, E. Michel, J. Horwath, and C. W. Miller. Tunable magnetocaloric effect in transition metal alloys. *Scientific Reports*, 5(15755), 2015.
- [92] S.M. Na, J.H. Yoo, P. K. Lambert, and N.J. Jones. Room-temperature ferromagnetic transitions and the temperature dependence of magnetic behaviors in FeCoNiCr-based high-entropy alloys. *AIP Advances*, 8(056412), 2018.
- [93] P. Koželj, S. Vrtnik, A. Jelen, M. Krnel, D. Gačnik, G. Dražić, A. Meden, M. Wencka, D. Jezeršek, J. Leskovec, S. Maiti, W. Steurer, and J. Dolinšek. Discovery of a FeCoNiPdCu high-entropy alloy with excellent magnetic softness. *Adv. Eng. Mat.*, 21(5):1801055, 2019.
- [94] Y. Yuan, Y. Wu, X. Tong, H. Zhang, H. Wang, X.J. Liu, L. Ma, H.L. Suo, and Z.P. Lu. Rare-earth high-entropy alloys with giant magnetocaloric effect. *Acta Materialia*, 125:481 – 489, 2017.

- [95] J. W. Yeh, Y. L. Chen, S. J. Lin, and S. K. Chen. High-entropy alloys – a new era of exploitation. *Mater. Sci. Forum*, 560(1), 2007.
- [96] J.W. Yeh. Recent progress in high entropy alloys. *Annales De Chimie – Science des Matériaux*, 31, 2006.
- [97] W. Hume-Rothery and H.M. Powell. On the theory of super-lattice structures in alloys. *Zeitschrift fur Kristallographie*, 91(23), 1935.
- [98] W. Hume-Rothery. *Atomic Theory for Students of Metallurgy*. The Institute of Metals, London, 1969.
- [99] W. Hume-Rothery. The transition metals and their alloys. *Adv. Phys.*, 3:149–243, 1954.
- [100] A. H. Cottrell. *An Introduction to Metallurgy*. Edward Arnold, London, 1967.
- [101] Z. Wu, H. Bei, F. Otto, G.M. Pharr, and E.P. George. Recovery, recrystallization, grain growth and phase stability of a family of FCC-structured multi-component equiatomic solid solution alloys. *Intermetallics*, 46:131 – 140, 2014.
- [102] X. Yang, Y. Zhang, and P.K. Liaw. Microstructure and compressive properties of NbTiVTaAl_x high entropy alloys. *Procedia Engineering*, 36:292 – 298, 2012. IUMRS International Conference in Asia 2011.
- [103] O.N. Senkov, G.B. Wilks, D.B. Miracle, C.P. Chuang, and P.K. Liaw. Refractory high-entropy alloys. *Intermetallics*, 18(9):1758 – 1765, 2010.
- [104] M. C. Tropsky, R. Morris J, P. R. C. Kent, A. R. Lupini, and G. M. Stocks. Criteria for predicting the formation of single-phase high-entropy alloys. *Phys. Rev. X*, 5(011041), 2015.
- [105] W.Q. Zhang, C.S. Lou, X.C. Wu, H.M. Fu, and H.F. Zhang. Microstructures and mechanical property of AlCoNiCrFe alloy annealed in high magnetic field. *Materials Science and Technology*, 31(11), 2015.
- [106] J.W. Yeh, S.K. Chen, J.Y. Gan, S.J. Lin, T.S. Chin, T.T. Shun, C.H. Tsau, and S.Y. Chang. Formation of simple crystal structures in solid-solution alloys with multi-principal metallic elements. *Metall. Mater. Trans. A*, 35A:2533–2536, 2004.
- [107] D.B. Miracle and O.N. Senkov. A critical review of high entropy alloys and related concepts. *Acta Materialia*, 122:448–511, 2017.
- [108] R. Kozak, A. S. Sologubenko, and W. Steurer. Single phase high entropy alloys—an overview. *Zeitschrift fur Kristallographie*, 230(1), 2014.
- [109] A.C. Yeh, Y. J. Chang, C.W. Tsai, Y.C. Wang, J.W. Yeh, and C. M. Kuo. On the solidification and phase stability of a Co-Cr-Fe-Ni-Ti high-entropy alloy. *Met. Mat. Trans. A.*, 45A:184–190, 2014.

- [110] Y. F. Kao, S. K. Chen, J. H. Sheu, J. T. Lin, W. E. Lin, J. W. Yeh, S. J. Lin, T. H. Liou, and C. W. Wang. Hydrogen storage properties of multi-principal-component $\text{CoFeMnTi}_x\text{V}_y\text{Zr}_z$ alloys. *Int. J. Hydrogen Energy*, 35(9046), 2010.
- [111] O.N. Senkov, J.M. Scott, S.V. Senkova, D.B. Miracle, and C.F. Woodward. Microstructure and room temperature properties of a high-entropy TaNbHfZrTi alloy. *Journal of Alloys and Compounds*, 509(20):6043 – 6048, 2011.
- [112] O.N. Senkov and C.F. Woodward. Microstructure and properties of a refractory NbCrMo_{0.5}Ta_{0.5}TiZr alloy. *Materials Science and Engineering: A*, 529:311 – 320, 2011.
- [113] Y. Zhang. Microstructures and properties of high entropy alloys. *Prog. Mat. Sci.*, 61:1–93, 2004.
- [114] W. J. Boettinger and J. H. Perepezko. Fundamentals of rapid solidification. In *Rapidly Solidified Crystalline Alloys*. Proceedings of a TMS-AIME North East Regional Meeting, May 1-3 1985.
- [115] A. Guinier and D. L. Dexter. *X-ray Studies of Materials*. Interscience Publishers, New York, 1963.
- [116] P. Barnes, S. Jacques, and M. Vickers. Sources of peak broadening (retrieved from <http://pd.chem.ucl.ac.uk>).
- [117] A. Arrott and J.E. Noakes. Approximate equation of state for nickel near its critical temperature. *Phys. Rev. Lett.*, 19(14):786–789, 1967.
- [118] V. Franco, J.S. Blazquez, and A. Conde. Field dependence of the magnetocaloric effect in materials with a second order phase transition: A master curve for the magnetic entropy change. *Appl. Phys. Lett.*, 102:013908, 2007.
- [119] S. Kobe. *Phys. Status Solidi*, 41:K13, 1969.
- [120] Michael Kalvius and Paul Kienle. *The Rudolf Mössbauer Story: His Scientific Work and Its Impact on Science and History*. Springer-Verlag Berlin Heidelberg, Berlin, 2012.
- [121] R.H. Herber. *Mössbauer Effect, in the McGraw Hill Encyclopedia of Physics*. McGraw Hill, New York, 1982.
- [122] U. Gonser. *Mössbauer Spectroscopy*. J. Springer, 1975.
- [123] C. Kimball, W. D. Gerber, and A. Arrott. Antiferromagnetism in FCC and HCP iron—manganese alloys: Mössbauer effect. *Journal of Applied Physics*, 34(1046), 1963.
- [124] A. Yamada, Y. B. Wang, T. Inoue, W. G. Yang, C. Park, T. Yu, and G. Y. Shen. High-pressure x-ray diffraction studies on the structure of liquid silicate using a Paris–Edinburgh type large volume press. *Rev. Sci. Instrum.*, 82(015103), 2011.

- [125] G. Shen, P. Chow, Y. Xiao, S. Sinogeikin, Y. Meng, W. Yang, H.P. Lieermann, O. Shebanova, E. Rod, A. Bommannavar, and H.K. Mao. HPCAT: an integrated high-pressure synchrotron facility at the Advanced Photon Source. *High Press. Res.*, 28:145–162, 2008.
- [126] A. Leary, S. Kernion, M.A. Lucas, P. R. Ohodnicki, and M. E. McHenry. The influence of pressure on the phase stability of nanocomposite $\text{Fe}_{88}\text{Zr}_7\text{B}_4\text{Cu}_1$ during heating. *J. Appl. Phys.*, 113(17A317-317-3), 2013.
- [127] J. Liu. High pressure x-ray diffraction techniques with synchrotron radiation. *Chinese Phys. B.*, 25(076106), 2016.
- [128] K. Yosida. Magnetic properties of Cu-Mn alloys. *Physical Review*, 106(5):893–898, 1957.
- [129] M. E. McHenry, J. M. MacLaren, M. E. Eberhart, and S. Crampin. Electronic and magnetic properties of Fe/Au multilayers and interfaces. *J. Mag. Mag. Matls.*, 88:134, 1990.
- [130] D Spisák and J Hafner. Electronic and magnetic structure of Mn-Ni alloys in two and three dimensions. *Journal of Physics: Condensed Matter*, 11(33):6359–6372, aug 1999.
- [131] S. D. Willoughby, J. M. MacLaren, T. Ohkubo, S. Jeong, M. E. McHenry, D. E. Laughlin, and S-J. Choi. Electronic, magnetic, and structural properties of $\text{11}_0\text{fept}_x\text{pd}_{1-x}$ alloys. *J. Appl. Phys.*, 91 (10):8822–8824, 2002.
- [132] S. Willoughby. *Theoretical Investigations of Co-Pt Alloys and Supercells*. Ph.D Thesis, Tulane Univ., New Orleans, LA, 2002.
- [133] M. E. McHenry, J. M. MacLaren, and D. P. Clougherty. Monolayer magnetism of 3d transition metals in Ag, Au, Pd, and Pt hosts: Systematics of local moment variation. *J. Appl. Phys.*, 70:10611, 1991.
- [134] M. E. McHenry, J. M. MacLaren, and D. P. Clougherty. Monolayer magnetism of 3d transition metals in Ag, Au, Pd, and Pt hosts: Systematics of local moment variation. *Journal of Applied Physics*, 70(5932), 1991.
- [135] B.W. Corb and R.C. O’Handley. Magnetic properties and short-range order in Co-Nb-B alloys. *Physics Review B*, 31(11), 1985.
- [136] A. M. Ghemawat, M. E. McHenry, and R. C. O’Handley. Magnetic moment suppression in rapidly solidified Co-Te-B alloys. *Journal of Applied Physics*, 63, 1989.
- [137] R. L. Jacobs, E. Babic, and J. P. Xanthakis. Virtual bound states in transition metal alloys. *J. Phys. F: Met. Phys.*, 15(9):1941–1949, 1985.
- [138] M. Kurniawan, A. Perrin, P. Xu, V. Keylin, and M. McHenry. Curie temperature engineering in high entropy magnetic alloys for magnetocaloric applications. *IEEE Magn. Lett.*, 7:6105005, 2016.

- [139] Metal Prices Index. <https://www.metalprices.com/index.html>, 2017.
- [140] A. Perrin, M. Sorescu, M.T. Burton, D. E. Laughlin, and M. McHenry. The role of compositional tuning of the distributed exchange on magnetocaloric properties of high-entropy alloys. *Journal of Metals*, 69(11), 2125-2129.
- [141] P. Alvarez-Alonso, J. L. Sánchez Llamazares, C. F. Sánchez-Valdés, G. J. Cuello, V. Franco, P. Gorria, and J. A. Blanco. On the broadening of the magnetic entropy change due to Curie temperature distribution. *Journal of Applied Physics*, 115(17A929), 2014.
- [142] P. Gorria, J. L. Sanchez Llamazares, P. Alvarez, M. Jose Perez, J. Sanchez Marcos, and J. A. Blanco. Relative cooling power enhancement in magneto-caloric nanostructured Pr₂Fe₁₇. *Journal of Physics D:Applied Physics*, 41, 2008.
- [143] D.M. Rajkumar, M. Manivel Raja, R. Gopalan, and V. Chandrasekaran. Magnetocaloric effect in high-energy ball-milled Gd₅Si₂Ge₂ and Gd₅Si₂Ge₂/Fe nanopowders. *Journal of Magnetism and Magnetic Materials*, 320, 2008.
- [144] J. J. Ipus, J. S. Blázquez, V. Franco, A. Conde, and L. F. Kiss. Magnetocaloric response of Fe₇₅Nb₁₀B₁₅ powders partially amorphized by ball milling. *Journal of Applied Physics*, 105(123922), 2009.
- [145] W. Dagula, O. Tegus, B. Fuquan, L. Zhang, P. Z. Si, M. Zhang, W. S. Zhang, E. Bruck, F. R. de Boer, and K. H. J. Buschow. Magnetic-entropy change in Mn_{1.1}Fe_{0.9}P_{1-x}Ge_x compounds. *IEEE Transactions on Magnetics*, 41(10), 2005.
- [146] R. Caballero-Flores, V. Franco, A. Conde, K. E. Knippling, and M. A. Willard. Influence of Co and Ni addition on the magnetocaloric effect in soft magnetic amorphous alloys. *Applied Physics Letters*, 96(182506), 2010.
- [147] B. Fultz. *Mössbauer Spectroscopy Applied to Magnetism and Materials Science*. 1993.
- [148] H. Franke and M. Rosenberg. Influence of Fe²⁺ concentration on the Mössbauer spectra of iron-cobalt and iron-nickel ferrites. *Physica*, 86(88B), 1977.
- [149] N.N. Delyagin, A.L. Erzinkyan, V.P. Parfenova, and I.N. Rozantsev. Mössbauer studies of the states of Fe atoms in the antiferromagnetic Fe–Mn Invar alloys. *Journal of Alloys and Compounds*, 573:11–14, 2013.
- [150] J. Swierczek. Medium range ordering and some magnetic properties of amorphous Fe₉₀Zr₇B₃ alloy. *J. Magnetism and Mag. Mat.*, 322:2696–2702, 2010.
- [151] V. Y. Verchenko, A. A. Tsirlin, A. V. Sobolev, I. A. Presniakov, and A. V. Shevelkov. Ferromagnetic order, strong magnetocrystalline anisotropy, and magnetocaloric effect in the layered telluride Fe_{3-x}GeTe₂. *Inorganic Chemistry*, 54:8598–8607, 2015.

- [152] H. M. Widatallah, T. M. H. Al-Shahumi, A. M. Gismelseed, Z. Klencsár, A. D. Al-Rawas, I. A. Al-Omari, M. E. Elzain, A. A. Yousif, and M. Pekala. Structural and ^{57}Fe Mössbauer study of $\text{EuCr}_{1-x}\text{Fe}_x\text{O}_3$ nanocrystalline particles. *Hyperfine Interact.*, 205:101–104, 2012.
- [153] N. Miyajima, K. Akasaka, T. Waki, Y. Tabata, Y. Kobayashi, and H. Nakamura. Mössbauer effect of Ni-doped strontium ferrite. *Hyperfine Interact.*, 206:115–118, 2012.
- [154] V. V. Khovaylo, T. Kanomata, T. Tanaka, M. Nakashima, Y. Amako, R. Kainuma, R. Y. Umetsu, H. Morito, and H. Miki. Magnetic properties of $\text{Ni}_{50}\text{Mn}_{34.8}\text{In}_{15.2}$ probed by Mössbauer spectroscopy. *Phys. Rev. B*, 80(144409), 2009.
- [155] C. L. Chien. Mössbauer study of a binary amorphous ferromagnet: $\text{Fe}_{80}\text{B}_{20}$. *Phys. Rev. B*, 18:1003–15, 1978.
- [156] H. Qin. Composite magnetic materials based on nanocrystalline powders for high-frequency applications. *J Magn. Magn. Mat.*, 310:864–866, 2007.
- [157] C. Kuhrt and L. Schultz. Phase formation and martensitic transformation in mechanically alloyed nanocrystalline Fe–Ni. *J. Appl. Phys.*, 73(1995), 1993.
- [158] J. Restrepo, G. A. Pérez Alcázar, and A. Bohórquez. Description in a local model of the magnetic field distributions of $\text{Fe}_{1-x}\text{Ni}_x$ disordered alloys. *J. Appl. Phys.*, 81(4101), 1997.
- [159] V.V. Serikov, N.M. Kleinerman, A.V. Vershinin, N.V. Mushnikov, A.V. Protasov, L.A. Stashkova, O.I. Gorbatov, A.V. Ruban, and Yu.N. Gornostyrev. Formation of solid solutions of gallium in Fe–Cr and Fe–Co alloys: Mössbauer studies and first-principles calculations. *J. Alloys and Comp.*, 614:297–304, 2014.
- [160] V. M. Nadutov, A. V. Proshak, S. Y. Makarenko, V. Y. Panarin, and M. Y. Svavil’nyj. Creation and Mössbauer studies of high-entropy physical vapor deposition by cathode arc evaporation (PVD CAE) coating AlFeCoNiCuCr . *Mat.-wiss. u. Werkstofftech.*, 47(2-3), 2016.
- [161] J. Świerczek and A. Kupczyk. Magnetic entropy change in amorphous and partially crystallized Fe–Mo–Cu–B alloy. *Journ. Magnetism and Mag. Mat.*, 386:74–80, 2015.
- [162] J. Crangle and G. C. Hallam. The magnetization of face-centred cubic and body-centred cubic iron + nickel alloys. *Proceedings of the Royal Society A*, 272(1348), 1963.
- [163] J.A.C. Marples. The lattice parameters of alpha-manganese at low temperatures. *Physics Letters A*, 24(4):207–208, 1967.
- [164] V. V. Brazhkin and A. G. Lyapin. Lattice instability approach to the problem of high-pressure solid-state amorphization. *High Pressure Research*, 15(1), 1996.

- [165] A. G. Lyapin and V. V. Brazhkin. Pressure-induced lattice instability and solid-state amorphization. *Physical Review B*, 54(17), 1996.
- [166] B. H. Toby and R.B. Von Dreele. GSAS-II: the genesis of a modern open-source all purpose crystallography software package. *J. Appl. Crystall.*, 46(2):544–549, 2013.
- [167] K.Tang, L.B.Chen, S.Wang, R.Wei, Z.Y.Yang, F.Jiang, and J.Suna. Development of a large size FCC high-entropy alloy with excellent mechanical properties. *Mat. Sci. Eng. A*, 761(138039), 2019.
- [168] G. Qin, R. Chen, H. Zheng, H. Fang, L. Wang, Y. Su, J. Guo, and H. Fu. Strengthening FCC-CoCrFeMnNi high entropy alloys by Mo addition. *J. Mat. Sci. Tech*, 35(4), 2019.
- [169] B.E.Warren and B.L.Averbach. The effect of cold-work distortion on x-ray patterns. *J. Appl. Phys.*, 21(595), 1950.
- [170] B.E. Warren and B.L.Averbach. The separation of cold-work distortion and particle size broadening in x-ray patterns. *J. Appl. Phys.*, 23(497), 1952.
- [171] G.K.Williamson and W.H.Hall. X-ray line broadening from filed aluminium and wolfram. *Acta. Metall.*, 1:22–31, 1953.
- [172] Ph.B. Moin. Peculiarities of Ehrenfest equation for solids strained by uniaxial or hydrostatic pressure. (arXiv:1602.07656), 2015.
- [173] Ph.B. Moin. Ehrenfest equations for second-order phase transition under hydrostatic and uniaxial stresses. *Phase Transitions*, 89(11), 2016.
- [174] G. T. Alfieri, E. Banks, and K. Kanematsu. Pressure dependence of the curie temperature of ferromagnetic Laves phase alloys. *Journal of Applied Physics*, 40(1322), 1969.
- [175] M. Brouha and K.H.J. Buschow. Pressure dependence of the curie temperature of intermetallic compounds of iron and rare-earth elements, Th and Zr. *Journal of Applied Physics*, 44(1813), 1973.
- [176] K. T. Regner, S. Majumdar, and J. A. Malen. Pressure effect on the curie temperatures of transition metals and alloys. *Review of Scientific Instruments*, 84(064901), 2013.
- [177] L.J. Swartzendruber, V.P. Itkin, and C.B. Alcock. The Fe-Ni (iron-nickel) system. *Journal of Phase Equilibria*, 12(3), 1991.
- [178] H.E. Stanley. *Mean Field Theory of Magnetic Phase Transitions*. Oxford University Press, 1971.
- [179] A. Perrin, M. Sorescu, V. Ravi, M. T. Burton, D.E. Laughlin, and M. E. McHenry. Mössbauer analysis of compositional tuning of magnetic exchange interactions in high entropy alloys. *AIP Advances*, 2019.

- [180] J. B. Mann. Atomic structure calculations. ii. hartree-fock wavefunctions and radial expectation values: hydrogen to lawrencium. Technical report, LLNL, 01 1968.
- [181] L. Patrick. Antiferromagnetism of manganese. *Physical Review.*, 93(3).
- [182] C. Baldasseroni, C. Bordel, A.X. Gray, A.M. Kaiser, and F. Kronast. Temperature-driven nucleation of ferromagnetic domains in FeRh thin films. *Applied Physics Letters*, 100(262401), 2012.
- [183] X.L. Qian, D.M. Deng, Y. Jin, B. Lu, S.X. Cao, and J.C. Zhang. Complex ferromagnetic-antiferromagnetic phase transition and glass-like arrest of kinetics in $\text{Sm}_{(1-x)}\text{Ba}_{(x)}\text{CrO}_3$ ($x=0$ and 0.1). *Journal of Applied Physics*, 115(193902), 2014.
- [184] J. S. Kouvel and C. C. Hartelius. Anomalous magnetic moments and transformations in ordered FeRh alloy. *J. Appl. Phys.*, 33:1343–1344, 1962.
- [185] M. E. Gruner, E. Hoffman, and P. Entel. Instability of the rhodium magnetic moment as the origin of the metamagnetic phase transition in alpha-FeRh. *Phys. Rev. B*, 67(064415), 2003.
- [186] J. A. Ricodeau and D. Mellville. Model of the antiferromagnetic-ferromagnetic transition in FeRh alloys. *J. Phys. F: Met. Phys.*, 2:337–350, 1972.
- [187] M. A. Khan. Band theory of non-magnetic and magnetic Fe-Rh alloys. *J. Phys. F: Met. Phys.*, 9:457–466, 1979.
- [188] P. Tu, A. J. Heeger, J. S. Kouvel, and J. B Comly. Mechanism for the first-order magnetic transition in the FeRh system. *J. Appl. Phys.*, 40(1368), 1969.
- [189] M. P. Annaorazov, S. A. Nikitin, A. L. Tyurin, K. A. Asatryan, and A. Kh. Dvletov. Anomalously high entropy change in FeRh alloy. *J. Appl. Phys*, 79(1689), 1996.
- [190] D. V. Maheswar Repaka, V. Sharma, A. Chanda, R. Mahendiran, and R. V. Ramanujan. Pressure dependence of resistivity and magnetic properties in a $\text{Mn}_{1.9}\text{Cr}_{0.1}\text{Sb}$ alloys. *AIP Advances*, 7(125009), 2017.
- [191] Sputtering Yield Rates. <http://www.semicore.com/reference/sputtering-yields-reference>, 2018.
- [192] G. Carter. Preferred orientation in thin film growth—the survival of the fastest model. *Vacuum*, 56(2):87–93, 2000.

Appendix A

Sample Synthesis

A.1 ICP-AES Data

In order to perform the calculations in section 4.2 accurately, I obtained more exact compositional data for each alloy using inductively coupled plasma atomic emission spectroscopy with the help of my collaborator, Vladimir Keylin at NASA Glenn Research Center. Table A.1 shows the full results. We can see that typically, my samples contain 0.5at% less Mn than the nominal composition calls for, but the difference in Mn content between samples is still roughly accurate. The data also shows a small amount of B contamination from the BNi crucible used to hold the molten ingot in the melt spinning process. Though these compositions are close to the nominal values, their inclusion in the quantitative calculations regarding pairwise interactions through Mössbauer made a significant difference in the final calculations given how small the compositional changes between alloy are.

Sample	%Fe	%Co	%Ni	% Cu	%Mn	%B
FeCoNiCuMn	20.1	20.3	20.1	20.0	19.5	0.05
Fe _{0.975} CoNiCuMn _{1.025}	19.7	20.2	20.1	20.0	20.0	0.05
Fe _{0.95} CoNiCuMn _{1.05}	19.31	20.17	20.11	20.11	20.29	N/A
FeCo _{0.975} NiCuMn _{1.025}	20.42	19.59	20.58	20.14	19.27	N/A
FeCo _{0.95} NiCuMn _{1.05}	20.26	19.26	20.29	20.12	20.07	0.05
FeCoNi _{0.975} CuMn _{1.025}	20.32	20.31	19.76	20.20	19.41	N/A
FeCoNi _{0.95} CuMn _{1.05}	20.28	20.18	19.17	20.06	20.31	N/A
FeCoNiCu _{0.975} Mn _{1.025}	20.37	20.2	20.15	19.66	19.62	0.01
FeCoNiCu _{0.95} Mn _{1.05}	19.9	20.1	20.1	18.9	19.9	1.33
FeCoNiCu _{0.925} Mn _{1.075}	20.24	20.12	20.16	18.63	20.86	N/A
FeCoNiCu _{0.9} Mn _{1.1}	20.28	20.19	20.18	18.17	21.18	0.05

Table A.1: Atomic percentages of each atom present in bulk FeCoNiCuMn for each psuedo-binary departure from equiatomic.

A.2 Thin Film Development

A.2.1 Compositional Analysis

Table A.2 shows the compositions of three different thin films measured using XPS analysis, compared with the compositional analysis of the bulk FeCoNiCuMn alloy.

Sample	%Fe	%Co	%Ni	% Cu	%Mn	% O	%C	%B
20nm, 10mTorr	16.07	18.83	22.98	15.84	18.05	6.71	1.52	–
20nm, 5mTorr (1)	13.4	20.1	23.58	15.77	21.78	4.59	0.8	–
20nm, 5mTorr (2)	12.47	19.31	25.96	15.75	21.06	4.46	1	–
Bulk	20.1	20.3	20.1	20.0	19.5	–	–	0.05

Table A.2: Atomic percentages of each species present in sputtered thin films (measured using XPS analysis) compared with experimental bulk composition.

It is immediately obvious that the compositions of the sputtered samples deviate from the target composition by a significant amount. However, the deviation is not in direct proportion to the sputtering rates of the individual elements. Cobalt and nickel have similar

elemental sputtering rates (190 A°/sec), but the Co values are all within 1% of the desired 20%, while the amount of nickel is 3-6% greater. Elemental copper has the fastest sputtering rate (320 A°/sec), but this is not reflected in the measured compositions, as the samples all contain around 4% less copper than desired. Manganese and iron have the lowest sputtering rates (180 A°/sec), but only iron has a dramatically reduced composition compared to the desired 20%. [191] These differences may be less dramatic in a thicker sputtered sample; as an element is preferentially sputtered from the target, the target is then depleted of that element, and the remaining elements are more likely to be sputtered, balancing the composition of the film, though it will be compositionally varied with depth. I have deposited and characterized a 100nm film as well, but it has not been probed with ICP analysis, so the effect of thickness on compositional ratios is not yet known.

This table also includes extraneous elements that are present due to contamination. The main contaminant in the melt spinning process used for the bulk samples is boron, due to the boron nitride crucible in which the sample is melted before quenching, but we can see this is a very minor contamination issue, as it only accounts for 0.05% of the total composition. Carbon and oxygen are both contaminants in the sputtering process because the sample is deposited from vaporized atoms traveling through the chamber. Even at very low pressures, there will be some amount of non-argon atmosphere remaining in the chamber. We can see that this contamination is significant regardless of the chamber pressure (at least 5.39% of the atomic composition), but the higher deposition pressure sample does contain roughly 2.2% more oxygen and 0.5% more carbon in the total composition, but it's not clear whether this contamination is homogeneous in the sample or clustered on the surface.

Further work to correct the compositional deviations from equiatomic must be done for these films to be used in place of the bulk; button targets of individual elements can be placed on the main target to increase the amount of that element sputtered, but getting the balance right will likely require several iterations of deposition and measurement. We will also need to determine the spatial dependence of the oxygen and carbon contamination and

take measures to reduce it.

A.2.2 Crystallographic Characterization

Despite the obvious compositional variation, structural and magnetic characterization revealed that many characteristics of these thin films are similar to the bulk FeCoNiCuMn alloys. I first performed XRD on each film. Sputtered thin films of metals are often amorphous because the deposition is random and rapid, but crystal ordering is possible for atoms that are typically ordered in the bulk. XRD spectra of completely amorphous films will consist of a broad hump over a large range of angles, whereas a completely crystalline structure exhibit sharp diffraction peaks at specific angles. Sputtered thin films of crystalline material will often experience preferred growth of a specific plane on the substrate which has the lowest energy. Typically, this is a close packed plane which for FCC crystals is the (111) plane, though it can often depend on the crystal structure and spacing of the substrate. [192]

I performed XRD on a 20nm film and a 100nm film (both sputtered in a 5mTorr Ar environment) to explore the extent to which each film was amorphous versus crystalline, and if crystalline, how much preferential orientation occurred. I found that the 20nm film was crystalline, and strongly oriented in the (111) direction. Fig. A.1 shows the XRD pattern of the 20nm film overlaid on the bulk sample for clarity. The thin film scan is cut off at 60 degrees because of the large background peaks from the Si substrate, but no peaks were seen at higher angles. In contrast, Fig. A.2 shows the XRD pattern of the 100nm film, which has a large (111) plane diffraction peak, as well as weak peaks in the (200) and (311) orientation. While the 100nm is still clearly crystalline, it is less preferentially oriented as the increased thickness allows for more misorientation to occur as the layers deposit. Thus, both of these thin films are crystalline with the same lattice parameters as the bulk, but the 100nm film is structurally a more accurate representation of the bulk sample in terms of crystal orientation.

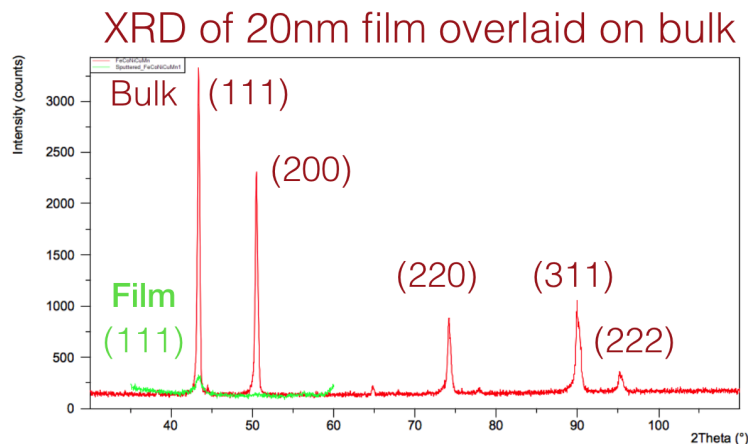


Figure A.1: X-ray diffraction of a 20nm thin film sputtered from an equiatomic FeCoNiCuMn target.

A.2.3 Magnetic Characterization

I then used the VSM attachment on the PPMS to obtain magnetization data for both film thicknesses to compare with the bulk. I obtained magnetization versus field curves at room temperature to see the extent of hysteretic behavior in these films, as well as magnetization versus temperature curves to determine how close the Curie temperature of the sputtered samples were to the bulk equiatomic FeCoNiCuMn (where $T_c=405\text{K}$). Fig. A.3 shows that temperature dependence of the magnetization of the two films is very similar close to the Curie temperature. Fitting this data gives a $T_c=419\text{K}$ for the 20nm film, and $T_c=426\text{K}$ for the 100nm film, both of which are within 20K of the bulk. However, it is important to note that these transition temperatures arise out of a different balance of exchange interactions given the large composition deviation from equiatomic observed for these films. The low temperature magnetic transition observed at 50K in the bulk samples also differs in the sputtered samples; the 20nm film experiences this transition at 50K as well, but the 100nm has a lower transition, at 40K.

The magnetization versus field measurements (Fig. A.4) give us further insight into the magnetic behavior of these films in comparison to the bulk. Bulk samples in the FeCoNiCuMn alloy system exhibit very low coercivities, on the order of 20 Oe along the easy axis

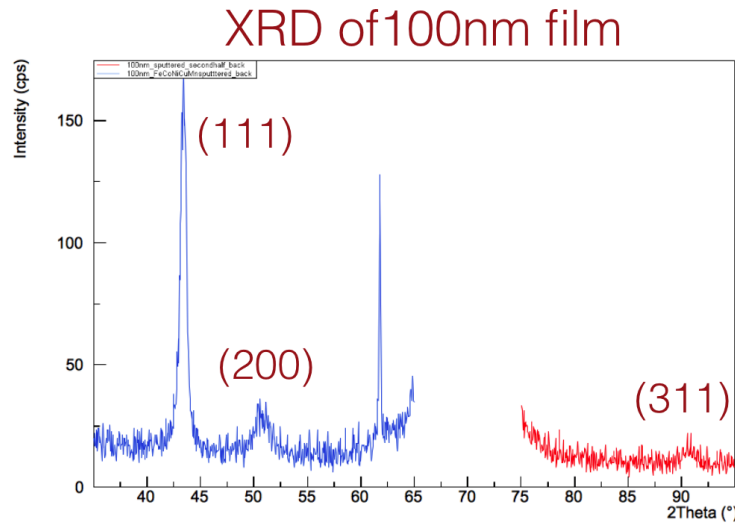


Figure A.2: X-ray diffraction of a 100nm thin film sputtered from an equiatomic FeCoNiCuMn target.

of the flake. In plane and out of plane measurements of the magnetization versus field yield different coercivities, both of which are low each that the samples can be considered soft magnetic materials, but still significantly higher than that of the bulk sample. This is due to the shape of the thin films, which inhibits rotation of magnetic moments. The in plane measurements yield higher coercivities than the out of plane, but overall require a smaller saturation field. The saturation magnetization of the films is difficult to calculate exactly as I can only estimate the total volume of film on the measured sample, but rough calculations of the saturation magnetization of each film are similar to that of the bulk sample, which is 40 emu/g. Thus in terms of magnetic behavior, both thicknesses of film are similar to the bulk sample, but the 100nm film out of plane, though T_c is higher, is the most representative of the properties of the bulk.

A.2.4 Conclusion

Compositional analysis as well as structural and magnetic measurements of thin films sputtered from an equiatomic FeCoNiCuMn target demonstrate that it is possible to develop thin film approximations of bulk high entropy alloys. Though compositional exactness will

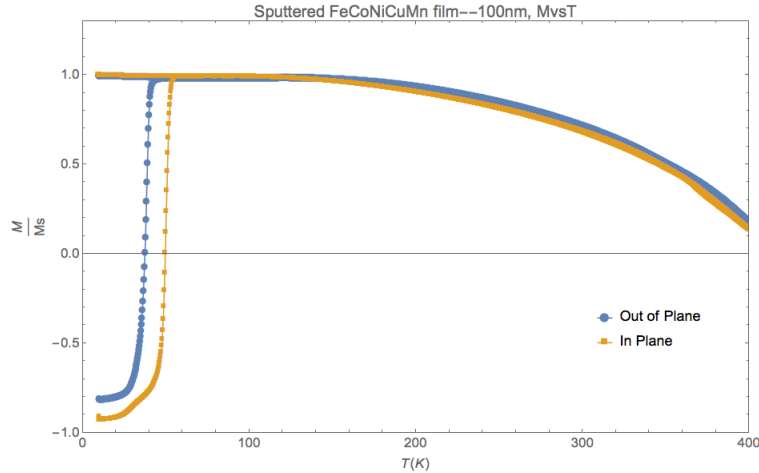


Figure A.3: Magnetization vs. temperature of the sputtered thin films, normalized for shape comparison.

Sample	In-Plane Coercivity	Out of Plane Coercivity	H_s In Plane	H_s Out of Plane
Bulk	20 Oe			
20nm film	1600 Oe	600 Oe	1500 Oe	5000 Oe
100nm film	1400 Oe	400 Oe	1500 Oe	5000 Oe

Table A.3: Coercivity and saturation fields for thin films and bulk samples of FeCoNiCuMn.

require more iterations of fine-tuning the sputtering process, preliminary crystallographic and magnetic analysis shows that the sputtered films behave similarly to the bulk alloy being replicated. The thicker of the two characterized films is less preferentially oriented and slightly less magnetically hard, but the 20nm film is still a reasonable approximation of the bulk alloys. Therefore these films are a suitable substitute for the bulk alloys in experiments requiring a thin film or highly reflective sample.

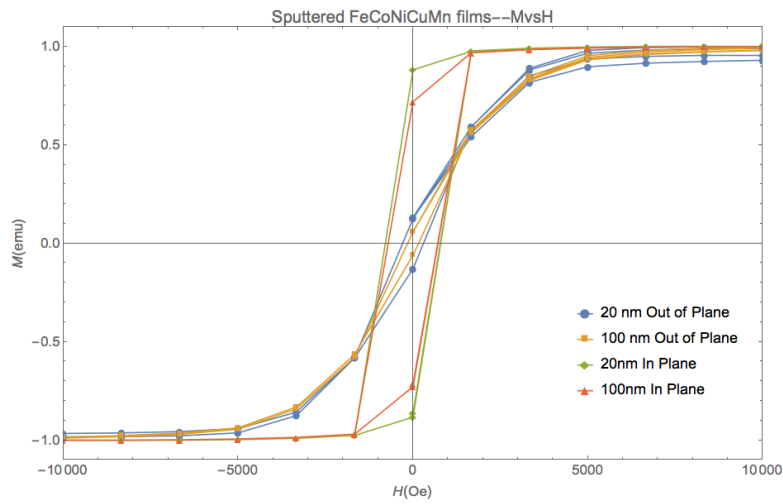


Figure A.4: Magnetization vs. field for sputtered thin films, demonstrating the in plane coercivity to be larger than out of plane for both thicknesses of film.

Appendix B

Relevant Phase Diagrams

The issue of discerning which elements will mix well together in a high entropy alloy is complicated; Hume Rothery rules are helpful, but determining the enthalpy of mixing and immiscibility of elements with each other using phase diagrams can be a helpful predictor as well, and can also be a diagnostic tool for understanding why specific segregation or intermetallics are forming. Specifically for the FeCoNiCuMn HEA system, we can see in binary phase diagrams of Mn with the other components of the alloy that Mn tends to form a single FCC phase with the other element at high temperatures. Thus, it is unsurprising that its addition leads to a single phase FCC HEA compared with other additions such as Mo.

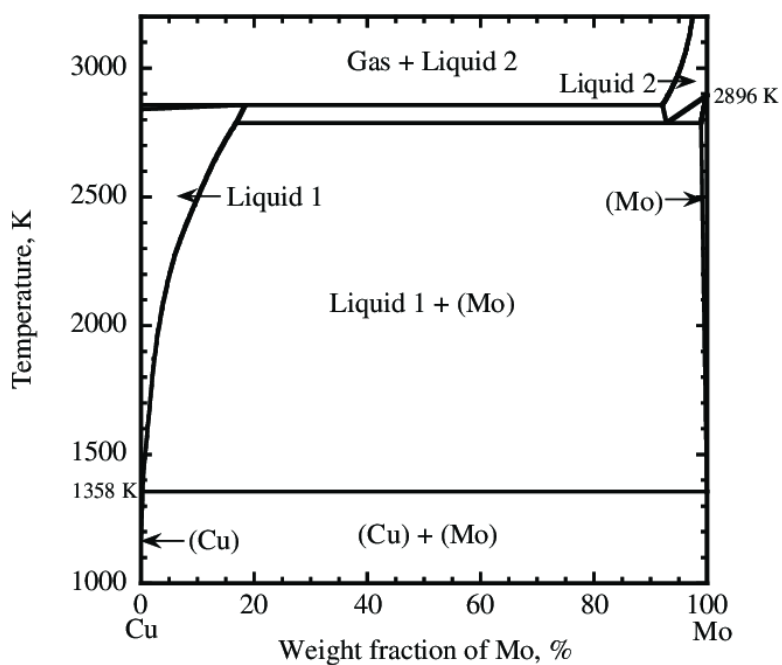


Figure B.1: Phase diagram for Cu-Mo binary system showing immiscibility up through liquid phases. [17]

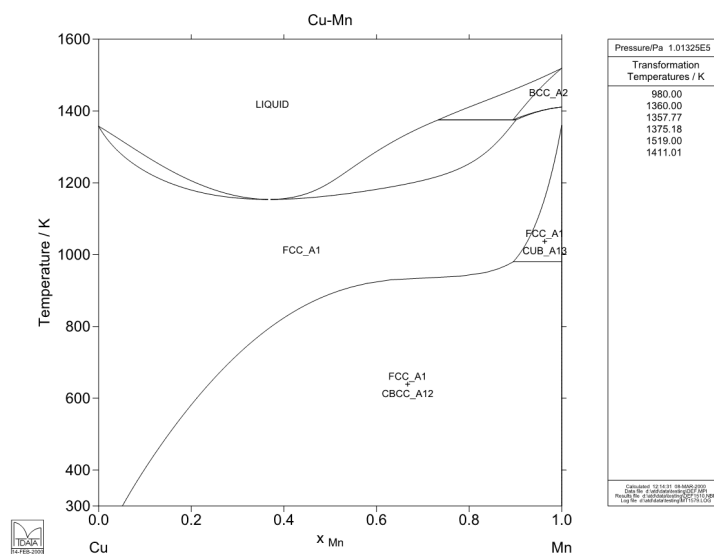


Figure B.2: Phase diagram for Cu-Mn binary system [18]

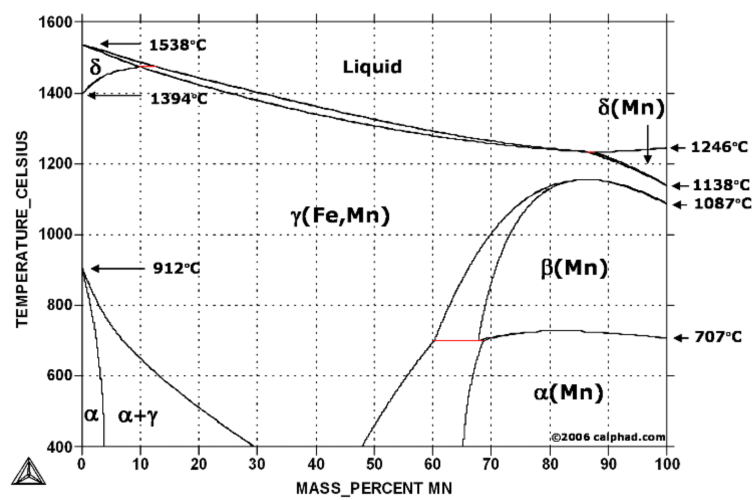


Figure B.5: Phase diagram for Fe-Mn binary system [20]

Appendix C

Mossbauer Raw Data

C.1 Raw Data Files

